Aeroacoustics of Compressible Vortex Reconnection

by

Hamid MohammadMirzaieDaryan

A thesis
presented to the University of Waterloo
in fulfillment of the
thesis requirement for the degree of
Doctor of Philosophy
in
Mechanical and Mechatronics Engineering

Waterloo, Ontario, Canada, 2021

Examining Committee Membership

The following served on the Examining Committee for this thesis. The decision of the Examining Committee is by majority vote.

External Examiner:	Yue Yang Professor, Dept. of Mechanics and Engineering Science, Peking University
Supervisor:	Jean-Pierre Hickey Assistant Professor, Dept. of Mechanical and Mechatronics Engineering, University of Waterloo
Internal Members:	Fue-Sang Lien Professor, Dept. of Mechanical and Mechatronics Engineering, University of Waterloo
	Sean Peterson Professor, Dept. of Mechanical and Mechatronics Engineering, University of Waterloo
Internal-External Member:	Francis Poulin Professor, Dept. of Applied Mathematics, University of Waterloo

Author's Declaration

This thesis consists of material all of which I authored or co-authored; please see the Statement of Contributions included in the thesis. This is a true copy of the thesis, including any required final revisions, as accepted by my examiners.

I understand that my thesis may be made electronically available to the public.

Statement of Contributions

All journal and conference papers published out of this thesis are listed as below:

- "Sound generation mechanism of compressible vortex reconnection" which is under review for publication in *Journal of Fluid Mechanics* [19]. Chapter 3 of the current thesis is based on this paper.
- "Aeroacoustic noise generation due to vortex reconnection" published in *Physical Review Fluids* [18]. Chapter 4 of the current thesis is based on this paper.
- "Aeroacoustic noise generation in compressible vortex reconnection" published in *11th International Symposium on Turbulence and Shear Flow Phenomena, TSFP 2019* [20]. Appendix C of the current thesis is based on this paper.

These papers are co-authored with my supervisor and Professor Fazle Hussain who played a normal advisory role in the research and made some editing works on the manuscript text.

Abstract

Aeroacoustics is a key focus in the design of propulsion, energy, and transportation systems. Noise generation in these systems is caused by the unsteadiness of the flow and simplified acoustic models are used to approximate the noise emission. Although the physical mechanisms of flow-generated noise remain plagued with a lot of uncertainty, we know that coherent structures play a significant role in this process. To understand the noise generation mechanisms, first, a thorough study of the physics of coherent structures and their self- and mutual interactions, as the dominant acoustic sources, is critical. Thus far, despite many experimental and numerical studies, there has not been consensus on the importance of vortex interactions; while, dominant acoustic sources (in jet noise) have been often attributed to vortex pairing. In this thesis, for the first time, the role of vortex reconnection, which leads to a violent topological change and rapid repulsion of vortex lines, in aeroacoustic noise generation is explored. For this, using direct numerical simulation (DNS) of the compressible Navier-Stokes equations, the sound generation mechanism of initially subsonic viscous vortex reconnection at the vortex Reynolds number $Re(\equiv$ circulation/kinematic viscosity$)= 1500$ is studied through decomposition of Lighthill's acoustic source term. The Laplacian of the kinetic energy, flexion product, enstrophy, and the deviation from the isentropic condition provide the dominant contributions to the acoustic source term. The overall (all time) extrema of the total source term and its dominant hydrodynamic components scale linearly with the reference Mach number, M_o; the deviation from the isentropic condition shows a quadratic scaling. The significant sound arising from the flexion product occurs due to the coiling and uncoiling of the twisted vortex filaments wrapping around the bridges when a rapid strain is induced on the filaments by the repulsion of the bridges. The spatial distributions of the various acoustic source terms reveal the importance of mutual cancellations among most of the terms; this also highlights the importance of symmetry breaking in the sound generation during reconnection. Compressibility acts to delay the start of the sequence of reconnection events, as long as shocklets, if formed, are sufficiently weak to not affect the reconnection. The delayed onset has direct ramifications on the sound generation by enhancing the velocity of the entrained jet between the vortices and increasing the spatial gradients of the acoustic source terms. Despite a subsonic reference Mach number of $M_o = 0.9$, reconnection could lead to shocklet formation where acoustic sources containing the Laplacian of the kinetic energy, density gradient, dilatation, and their interactions become dominant. Compressibility also intensifies the spatial distribution and sharp rise of the near-field low pressure which fades away in time. Consistent with the near-field pressure, the overall maximum instantaneous sound pressure level (SPL) in the far field has a quadratic dependence on M_o. At low M_o, the time-averaged sound directivity takes a quadrupole-like pattern. By increase of M_o,

not only the sound level intensifies, but the directivity pattern becomes elongated in the advection direction. Therefore, vortex reconnection, particularly at high reference Mach number, is recognized as a dominant sound-generating event.

Acknowledgements

I would like to thank all the people who made this thesis possible.

First and foremost, I wish to thank my supervisor, Professor Jean-Pierre Hickey, for his constant support over the last four years. Jean-Pierre taught me how to research effectively. I would always be deeply grateful for his encouraging supervision and patience. I would never forget our late, unplanned, long meetings. I would also like to thank the rest of my thesis committee: Prof. Yue Yang, Prof. Fue-Sang Lien, Prof. Sean Peterson, and Prof. Francis Poulin, for their insightful comments.

During my Ph.D. studies, I was fortunate to be advised by Professor Fazle Hussain. Fazle taught me the fundamentals of good research, writing, and presentation. I also had the chance to attend his research group meetings. I would like to thank all the members of Fazle's group, especially Jie Yao, Eric Stout, and Prof. Nadeem Malik, for their thoughtful comments.

I thank my labmates in Multi-Physics Interaction Lab: Mahboubeh Taftian, Joseph Mouallem, Khaled Younes, Chunhui Liu, Duosi Fan, Francis Lacombe, Amit Dutta, Joshua Wawryk, Jeremy Wang, Nicholas Christopher, Matthew Yao, Sai Praneeth, and Mark Epps, for their encouragement in the last four years. I'd also like to thank my friends in the MME department, Mehdi Ashrafizadeh, and SYDE, Amir Atoufi. I'd like to particularly thank my friend Amir for being always open to long discussions about different aspects of aeroacoustics and vortex dynamics.

I'd like to thank my friends: Fahimeh Kazemi, Hossein Soleimani, Amir Safarpoor, Ali Chehrazi, Milad Sikaroudi, Dan Rafii, Danial Maleki, and Mohammad Zandieh, who I spent most of my free time with them during my Ph.D. studies.

Finally, I would like to thank my family for their love, support, and encouragement.

Dedication

This thesis is dedicated to my parents, MohammadAli and Hoorieh, for their love, endless support, and encouragement.

Table of Contents

List of Figures

List of Tables

Abbreviations

1D one-dimensional 23

2D two-dimensional 2, 3

3D three-dimensional 4, 24, 56

CDIC Constant density initial condition 7, 9

CIC Constant initial condition 7, 9

DNS direct numerical simulation v, 1, 2, 11, 25

DTV Density-Temperature-Velocity 24

LES large-eddy simulation 13

LHS left-hand side 21, 35

MPI Message Passing Interface xi, 25, 26

PIC Polytropic initial condition 7, 9, 10, 29

RHS right-hand side 19, 21, 38, 56

SPL sound pressure level v, xiv, xv, 14, 69, 71, 72, 75

Chapter 1

Introduction

1.1 Overview

Aeroacoustics is the study of noise caused by temporal and spatial variations in an unsteady flow. Flow-generated noise is a central consideration to engineering design in a variety of fields such as propulsion, energy, and transportation. In many of these systems, engineers seek to mitigate noise propagated to the surrounding. In order to predicatively model the aeroacoustic noise in a fluidic system, we must first identify the acoustic sources and model the wave propagation to the far-field.

The numerical prediction of aeroacoustic noise helps inform the design for many fluidic systems. For wind turbines, propulsion, and engine test cells, the noise emission is an integral part of the engineering process and will constraint the design space. Many of these systems must meet strict standards on noise emission. Furthermore, aeroacoustics is important in the design of confined flows as the acoustic energy can accumulate into resonant modes leading to whistling and self-sustained oscillations [21]. This procedure can highly decrease the productivity and durability of the system. The origin of noise in these cases could be specific phenomena like cavity noise or intense flow as it appears in engine test cells.

Since acoustic waves convey only a minute fraction of the energy in the flow, the exact determination of sound sources by experiment is very challenging. Also, DNS of the acoustic field of real industrial problems is computationally expensive. Approximate methods which reduce the number of the acoustic sources to facilitate computations, i.e. aeroacoustic analogies, are beneficial but not exact. Therefore, to understand the physics

of sound generation mechanisms, it is better to focus on canonical flows which in turn enables us to mitigate the noise level.

The mechanism of aeroacoustic noise production and its relation to the far-field sound propagation remains poorly understood, in spite of decades of dedicated theoretical, numerical, and experimental studies. Intuitively, we know that coherent vortical structures and their self- and mutual interactions are significant aeroacoustic noise sources as they are the sinews and muscles of turbulence. In fact, coherent structures and their interactions have been often implicated as the main hydrodynamic source of jet noise [36, 30, 13]; however, the extent to which coherent structures are important in sound generation [4] and the types of vortical interactions that generate noise are poorly understood.

The idea that aeroacoustic noise can be modulated through the control of vortical structures has inspired many studies. Extending his earlier work [113] on jet turbulence suppression, Zaman [114] investigated noise suppression and enhancement of a subsonic jet through controlled excitation of the vortical structures (see also [37]). A higher level of organization and mutual interaction among the vortical structures in a laminar jet results in higher noise. However, controlled excitation of a transitional low-speed jet can suppress growth rate of the near-exit shear layer's Kelvin-Helmholtz instability and produce weaker coherent structures downstream, thus less noise. These experiments implied that not only the type, but the intensity of the vortical interaction is influential in sound generation. Eldredge [24] used DNS to investigate the sound generation of two-dimensional (2D) leapfrogging vortices. He showed that the primary acoustic pulse does not originate from the elastic deformation of the inner vortex cores but from the filamentary structures at the outer edges which rotate about the cores–based on Möhring's analogy [74], vorticity stretching and acceleration emerge as an intense noise source. Eldredge deduced that the sound is not necessarily caused by the explicit collision of the vortex cores.

A consensus on the dominant jet noise generation mechanism emerged in early studies [108, 53, 15, 63], where acoustic sources were attributed to vortex pairing. Hussain and Zaman [39] studied the coherent structures in the near field of an axisymmetric free jet and argued however that pairing is completed within four diameters from the jet exit, while most noise originates farther downstream. They proposed that reconnection of the toroidal rings through the evolution of azimuthal lobe structures produces most of the jet noise. Starting with the first suggestion by Melander and Hussain [70], vortical reconnection, which results in a violent topological change of the vortex tubes, has long been hypothesized as a significant contributor to aeroacoustic noise generation in broader classes of turbulent flows.

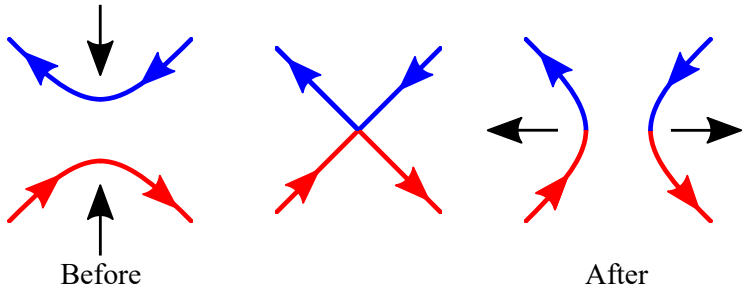

Figure 1.1: Schematic diagram of two anti-parallel vortex filaments before and after reconnection. Red and blue arrows show the vorticity directions. Black arrows show the convective directions.

1.2 Vortex Reconnection

One of the most important vortical interactions is vortex reconnection (cross-linking, cut-and-connect). When two vortex filaments with opposite vorticity directions approach each other, the induced velocity of each vortex affects the motion of the other one (based on the Biot-Savart law which will be discussed later) and two vortices join together and interact with each other through reconnection. Although vortex filaments prefer to keep their topological structures [69], their topology is altered during reconnection. As depicted in Figure 1.1, the topology of the two anti-parallel vortices is changed during reconnection. Each vortex filament is cut from the original filament and connects to the initially neighboring vortex. After exchanging of filament parts, two newly generated vortices recoil from each other in a perpendicular direction to the initial approaching.

Vortex reconnection studies started from the Crow's work on the instability of wingtip vortices [17]. Afterwards, researchers focused on the systematic experimental study of two circular vortex rings which was recognized as the simplest experimental case of the reconnection at that time [26, 89, 79]. Oshima and Asaka [78] captured two successive reconnections in their experiments. They observed that the reconnection of two vortex rings leads to an elongated single ring. After self-induction, this single ring experiences self-collision; the second reconnection takes place and the result is two vortex rings. They concluded that the repetition of such interactions depends on the initial speed and the diffusion. By that time, the experimental data involved averaging and was provided on 2D planes which was not sufficient to analyze the reconnection process [70]. In addition, in most of these experiments the evolution of a passive scalar, like dye or smoke, was captured to determine the behavior of vortex tubes. However, the evolution of vorticity field could be completely different [55] (discussed later).

Considering the experimental limitations in this special phenomenon and the rapid development of supercomputers, several numerical studies have been conducted to provide three-dimensional (3D) evolution of the reconnection process. First numerical simulations conducted at the late of 1980s. Ashurst and Meiron [3] simulated the reconnection of two vortex rings. They showed that at low Reynolds number (Re), which is defined by the ratio of the initial circulation of a single vortex tube over the kinematic viscosity, because of high level of diffusion, vortices disappear before reconnection. They emphasized that reconnection dynamics is highly sensitive to the configuration of vortex tubes; if the tube sections that are far from the reconnection region intensify the induced velocity near this region, the time scale of reconnection will be minimized. They also concluded that high velocity and low pressure between the two anti-parallel vortices cause the squeezing of tubes, which leads to the reduction of the vorticity in the original orientation and rotation to a new direction. Pumir and Kerr [86] provided numerical solution for $500 < Re < 5000$ and reported high level of stretching before reconnection. They stated that by increasing Re, the pairing process remains unchanged; however, the stretching intensifies. In addition, because the reconnection is impossible for inviscid and incompressible fluid flow (based on the Helmholtz's theorem which will be discussed later), some irregularities before reconnection are expected at high Re. Kida and Takaoka [54] simulated the evolution of the knotted vortex tube for $Re = 1200$ and introduced the bridging process. As they claimed, velocity induction produces high velocity gradients which cause that high-vorticity regions to be pulled out of the main vortex tube and join to the other one in a way that the thickness of these bundles (bridges) increases in time. They compared the bridging and vorticity cancellation mechanisms [3, 26, 78] and found that the topological change of two thin vortex filaments through cancellation is much faster than the bridging process for vortex tubes.

1.2.1 Reconnection Process

So far, numerical simulation of vortex reconnection has been conducted on three canonical configurations: vortex rings [3, 57, 56, 12], orthogonal vortices [73, 111, 9, 112, 5], and anti-parallel vortices with a perturbation [70, 5, 86, 52, 95, 106, 40, 102, 51]. Other studied cases contain trefoil knot [54, 58] and the interaction of two elliptical vortex rings [2]. An interesting aspect noted by Siggia [98], and also others [54, 55], is that as two vortex filaments with arbitrary orientations come close together, twist and become locally anti-parallel. Previously, the same procedure was observed in other studies [56, 73, 9, 79, 87]. Therefore, it is reasonable to focus on the configuration of two anti-parallel vortex tubes which allows high-resolution simulation and thus provides detailed data of reconnection [106]. As men-

tioned before, in experimental studies of the reconnection phenomenon, the evolution of a passive scalar is captured. On the other hand, in most of numerical simulations the enstrophy isosurface is visualized. Enstrophy isosurface could be theoretically different from the vorticity surface which contains vortex lines and constructs vortex tubes. Mathematically, evolution equation of the passive scalar follows an advection-diffusion equation. On the other hand, in the enstrophy equation, in addition to the diffusion term, the projected magnitude of vorticity in the direction of stretching term is modified. However, based on the vorticity equation (discussed later) both the magnitude and direction of vorticity are modified by the stretching term. Therefore, different evolution is expected for the passive scalar, enstrophy and vorticity. Accordingly, there should be a distinction between scalar, iso-enstrophy, and vortex tube reconnection [55, 109]. More specifically, in an inviscid and incompressible fluid flow, vortex tube reconnection is impossible, however, it may take place for two other fields.

Reconnection process consists of three characteristic stages:

1. Inviscid induction

   At the first stage, two anti-parallel vortex tubes approach each other by self- and mutual induction; see Figure 1.2(a). This process is almost inviscid [55, 42] and is described by the Biot-Savart law. As the vortex tubes get closer, the initial circular cross section shape of the vortex cores deforms, flattens, stretches, and takes a dipole head-tail structure; see the middle portion of Figure 1.2(a) where outer edges of the vortices are touching each other.

2. Bridging

   In the interaction region, viscous dissipation cancels the vorticity of closest anti-parallel vortex lines (this process is called viscous cross-diffusion in [42]). Simultaneously, these vortex lines with cancelled (reduced) vorticity in the original (axial) direction join to their counterparts in the other tube. Thus far, this process can be considered as the vorticity viscous cancellation mechanism mentioned in [3, 26, 78]. The reconnection process is not limited to viscous cancellation. New vortex lines (which have been cut from their original vortex lines and connected to the counterparts on the opposite tube), accumulate in the lateral direction (orthogonal to the axial direction) and construct the bridges; see Figure 1.2(b). The reason of this orthogonality could be the induced velocities in the interacting region which generate vorticity in the lateral direction [3]. For the first time, in 1987, Kida and Takaoka [54] introduced bridging procedure; however, their explanation of bridges (high-vorticity regions that are pulled out of the main vortex tube and join to the other one) is

not the same as here. For a better analysis, two symmetric, XY, and collision, XZ, planes are introduced in Figure 1.3(a). In the bridging stage, circulation on the symmetric plane begins to transfer to the collision plane. In addition, the head-tail structure which has been initiated in the previous stage intensifies and the tail experiences stretching. The head-tail structure at the bridging stage has been shown on the symmetric plane in Figure 1.3(b).

3. Threading

   Because of the self-induction, the bridges retreat (pull apart). The flow induced by the bridges is similar to a doublet on the collision plane [109] which leads to a downwash flow [42]; see Figure 1.3(c). As more vortex lines reconnect and gather in the bridges, the induced flow of the bridges becomes stronger and the velocity in the opposite direction of the initial dipole's motion increases. Figure 1.3(d) represents the dipole flow on the symmetric plane. The downward velocity induced by the bridges (downwash) opposes the pumping upward motion of the dipole at the contact zone which finally leads to two stagnation points at the front and the rear of the dipole. It has been claimed that bridges' upward motion (in the positive X direction) continues until they reach to the stagnation point in front of the dipole [70, 42]. As time goes forward and bridges become thicker, the downwash flow intensifies and finally reverses the curvature of the non-reconnected vortex lines of the initial two vortices (the initial curvature in the kink area is reversed). As a result of this reversal, the self-inductions of the non-reconnected vortex lines pull them apart. Simultaneously, because of the flow induced by the bridges, these non-reconnected vortex lines are wrapped around the bridges and are stretched as the bridges recoil from each other. Curvature reversal of the initial vortices halts further reconnection. Non-reconnected vortex lines are called threads [42] and survive from the reconnection; see Figure 1.2(d). Because of the stretching nature of the threads, so far, threading stage has not been captured in the experimental studies.

Previously Hussain and Melander [42, 72] claimed that the threads are the heads of the head-tail structure of the initial dipole. It has been assumed that as flow evolves and heads are separated from the tails, tails like heads experience viscous cross-diffusion. However, because of their low circulation, they diffuse and decay, and finally heads remain as the threads. The high-resolution simulation of the current study in a small domain reveals that even at low Re tails are not annihilated completely; see Appendix C. As the downwash forces heads to reverse their curvature and slows their motion, separated tails approach the heads and construct new dipole structures. It has been predicted that after a long time as two bridges recede from each other and the downwash effects reduce, threads as a new

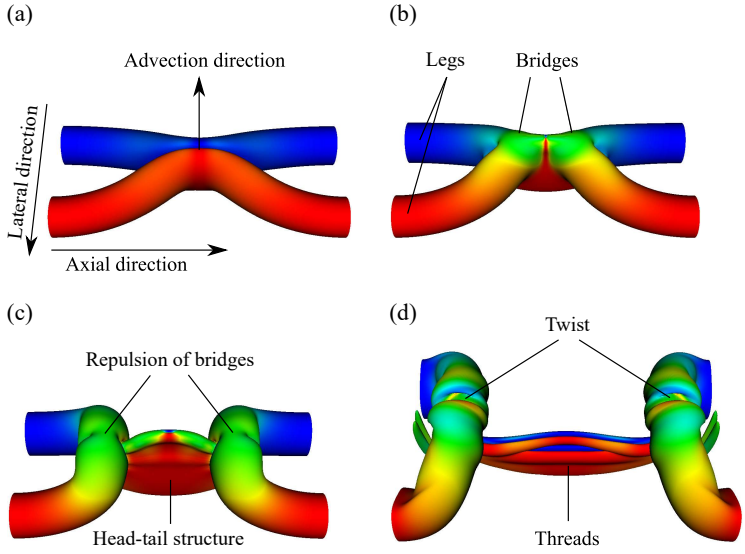

Figure 1.2: Reconnection process of two anti-parallel vortices including (a) inviscid induction, (b) bridging, (c) repulsion of bridges, and (d) threading. Blue, green, and red colors show negative, zero, and positive axial vorticity, respectively.

dipole can again reverse their curvature by mutual induction, approach each other, flatten, stretch, and cause the second reconnection [42, 72]. This long time can be justified by the stretching, which intensifies vorticity and postpones the cross-diffusion [70], and the initial gap between the threads.

1.2.2 Compressible Reconnection

In spite of the recent advances in characterizing incompressible reconnection [40, 110], relatively little is known about the compressible case, which involves a more complicated evolution owing to the strong dependence on the initial thermodynamic conditions [107] and additional vorticity generation mechanisms through dilatation and baroclinicity [106]. The strong dependence of the compressible vortex reconnection on initial thermodynamic conditions has been examined by Virk and Hussain [107]. They compared three initial conditions for pressure and density: 1) Constant density initial condition (CDIC), where density is considered constant and pressure is calculated from the Poisson equation. 2) Constant initial condition (CIC), where both density and pressure are constant. 3) Polytropic initial condition (PIC), where pressure is substituted by density using a polytropic relation and the Poisson equation is solved for the density. It has been showed that for

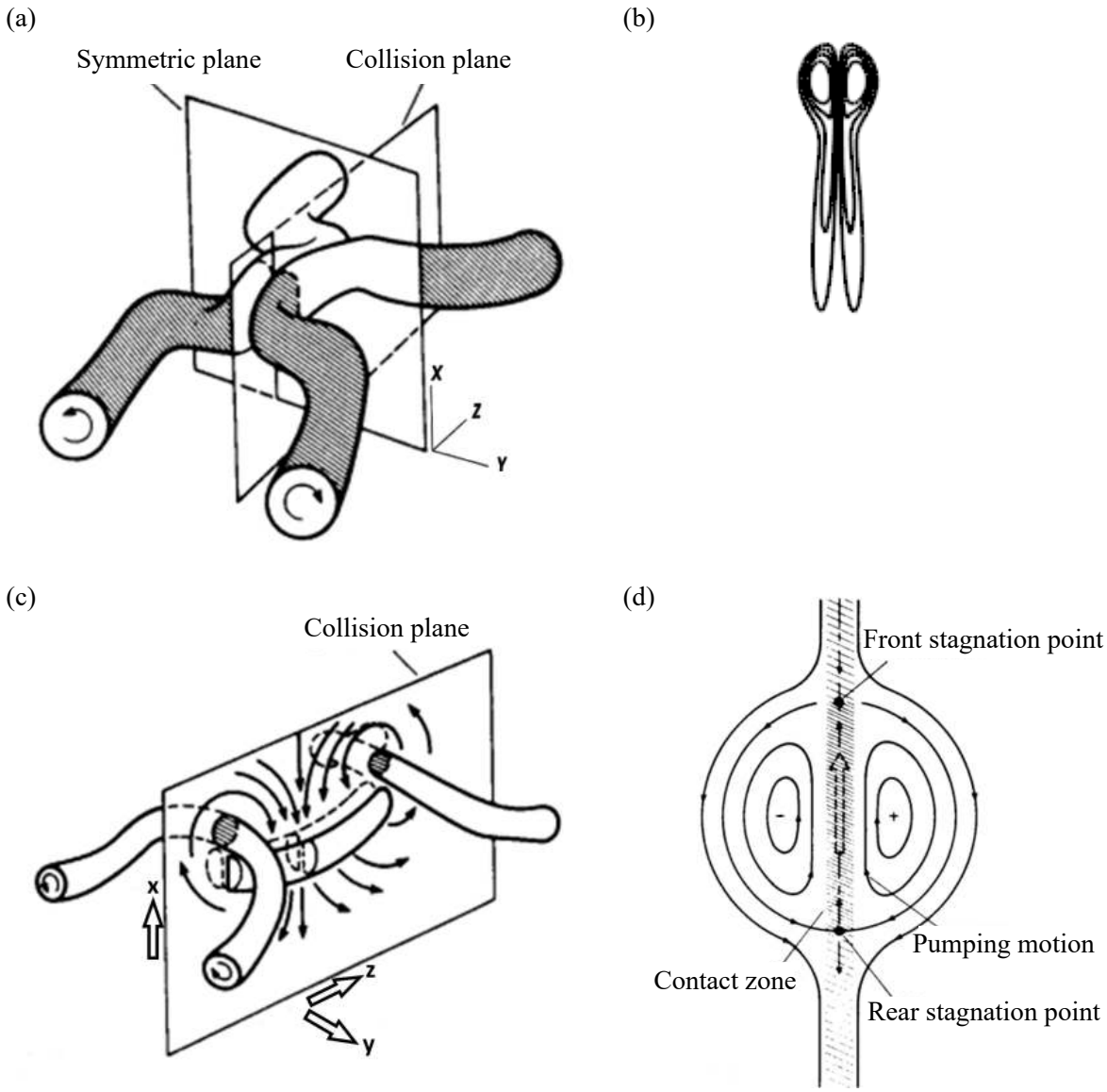

Figure 1.3: Schematic diagrams of (a) symmetric and collision planes, (b) head-tail structure, (c) downwash flow, and (d) stagnation points. Diagrams (a), (c), and (d) are modified figures from [70].

CDIC, two dominant effects of compressibility, namely baroclinic vorticity generation and shocklet formation (dilatation effect), cancel out during early evolution of compressible reconnection and artificial incompressible behavior occurs. Although CIC with uniform thermodynamics captures the salient features of compressible reconnection, the initially unbalanced centrifugal force generates a strong acoustic wave which negatively affects the subsequent reconnection dynamics. On the other hand, by balancing centrifugal force with the radial pressure gradient, PIC cancels acoustic transients and the results are consistent with the experimental observations [33, 22, 68] and theoretical analysis [25, 115] of compressible vortices. Therefore, PIC is selected as the most appropriate choice for the initial distribution of density and pressure in the compressible reconnection. Polytropic relation between pressure and density itself is not enough and the Poisson equation should be satisfied; otherwise, although general evolution trend remains the same, there will be perturbation and acoustic waves which could influence the reconnection dynamics especially at high Mach number (M). One may assume completely incompressible flow with unit density at the initial step, and after calculation of pressure by the Poisson equation, apply polytropic relation to find density. In the original PIC proposed in [107], polytropic relation is applied first and then, by assuming an inviscid flow, Poisson equation is solved for density directly.

Only a few works have considered compressible reconnection [50, 106, 91, 96, 82]– all of which are limited to low Re. In the transonic and supersonic regimes, incipient shocklet-induced reconnection alters the vorticity field causing earlier bridging but subsequent slowdown of the circulation transfer. More precisely, shocklet formation leads to an earlier circulation transfer from the symmetric to the collision plane. This early circulation transfer creates early bridges which oppose the mutual induction, initial vortices' curvature growth, vorticity gradient, and viscous cross diffusion. After shocklet diffusion, viscous cross diffusion becomes the main mechanism of circulation transfer and any factor that decreases viscous cross diffusion will weaken the rate of the circulation transfer. Therefore, at later times there is a reduction in the the rate of the circulation transfer and the peak vorticity on both of the symmetric and collision planes. Thus, at the same Re, the timescale of the compressible reconnection increases compared to the incompressible case [106]. It is known that compressibility also affects the domain of influence of vortical structures impacting the level of turbulence anisotropy in canonical flows [80, 32]. In addition to the hydrodynamic effects, shocklet formation during reconnection could represent an additional aeroacoustic sound source.

Virk *et al* [106] found that at high M, because of the undeveloped perturbation in the kink section and the reduction in the strain rate, the head-tail structure is not observed. They also captured early peaks in the circulation transfer rate and vorticity which are

associated to the early appearance of shocks. In addition, it has been seen that at higher Re the contribution of the baroclinic term in the circulation transfer is more than the viscous term. They claimed that at higher Re baroclinic vorticity generation could lead to a new topology, a closed vortex line, at the interaction region. Such topology requires at least two reconnections along a vortex line. Another feature of the baroclinic term mentioned in [106] is that it makes reconnection possible for the inviscid flows. However, considering PIC and knowing that $\frac{D(p\rho^{-\gamma})}{Dt} = 0$ for inviscid (and zero heat conduction–isentropic) flows, reconnection is impossible without viscous terms, which clearly highlights the role of the initial conditions and the fact that reconnection is a viscous phenomenon with PIC.

Two factors, namely axial flow inside the vortex tube [88] and the downwash flow induced by the bridges [106], are considered to analyze the vortex stretching on the symmetric plane. For enough high Re, pressure drop inside of the vortex tube is directly related to the square of the circulation. During reconnection, circulation on the symmetric plane reduces and is transferred to the collision plane, while circulations on the cross sections near the legs do not experience a large reduction. In other words, pressure drop on the symmetric plane will be lower than the cross sections near the legs which leads to the axial velocity gradient and vortex stretching along the vortex line. By increasing M, circulation transfer and strength of the bridges diminish which all cause less vortex stretching. The effect of the compressibility on the bridges has not been thoroughly explored yet. Preliminary observations suggest that by increasing the compressibility the threads become stronger and the vortex stretching in the bridges intensifies. On the other hand, the dilatation vorticity generation also becomes significant and reduces the peak vorticity on the collision plane. The ultimate effect of these two factors is weaker bridges. In comparison to the incompressible case with the same simulation time, bridges are father from the symmetric plane. In addition, compared to the vortex legs, bridges have less elevation in the direction of the initial vortices' movement which is expected as the strength and self-induction of the bridges decrease.

Virk *et al* [106] also stated that if the viscous diffusion is considered as a destruction mechanism of the shocklets, then shocklets can exist for a longer time at higher Re–note that the author of the current thesis does not believe that viscous effects play a significant role in the shocklet disappearance. Virk *et al* claimed that if shocklets exist for a longer time, the early circulation transfer could be large enough to complete the compressible reconnection at much shorter timescale; this behavior is only predicted and has not been investigated yet.

1.2.3 High-Re Reconnection

Previously, it has been claimed that coherent structures' repeated interactions, especially repeated reconnections which cause topological changes, are crucial in fine-scale mixing and energy cascade in turbulent flows, aerodynamic drag, destruction of aircraft wakes, and jet noise generation [70, 34, 36, 17, 92]. Thanks to recent progress in experimental facilities and computational resources, it has become possible to have a detailed investigation of such claims. In this regard, reconnection regains a renewed attention and becomes an active research field. Experiments of Lee and Fu [65] showed that reconnection of near-wall vortices plays an essential role in the creation of a chain of ring-like vortices in transitional and turbulent boundary layers. In 2011, Hussain and Duraisamy [40] conducted high resolution incompressible Navier-Stokes DNS of two anti-parallel vortex tubes reconnection for the range of $Re = (250, 9000)$ and provided some important scaling relations. Result of the highest Re is limited to the first collision; however, intense stretching of the threads is captured. It has been proposed that at high Re fine-scale reconnection cascade (repeating reconnection of threads) could take place. Unlike the superfluid and magnetic reconnections, vortex cores experience extreme deformation before viscous reconnection and bridges are formed gradually by gathering the reconnected vortex filaments. Because of the irregular vorticity distribution, they used vorticity centroid (only vorticity with more than 75% of the maximum vorticity is considered) to define vortex separation. Scaling analysis clearly showed that the repulsion of the bridges takes less time than the collision of the initial vortex tubes which could be justified by more intense curvature and self-induction of the bridges. More interestingly, scaling analysis showed that different initial conditions affect scale factor of the vortex separation before reconnection; however, scale factor after reconnection remains the same. In other words, repulsion of the bridges is independent of the initial conditions and is dominated by the local curvature and self-induction. As expected, increase of Re reduces the viscous cross-diffusion and postpones the formation of the bridges. In addition, results showed that as Re increases, the curvature and the abrupt repulsion of the bridges intensifies. These two factors lead to a smaller reconnection time (defined based on the circulation transfer) which has been verified by the scaling analysis. It has been mentioned that such acceleration during repulsion could be considered as a source of the noise generation.

Rees *et al* [102] studied anti-parallel vortex reconnection of higher Re, at $Re = 10000$. To explore the behavior of the vortices after the first reconnection, they continued the simulation for a longer time and captured the second collision of the elliptical ring which was generated as a result of the first reconnection. Their simulations demonstrated that reconnection of vortices without axial flow generates vortical structures containing axial

flow. This axial flow originates from the reconnection region towards the vortex legs. To investigate the effect of such axial flow in the secondary vortical structures, they simulated the reconnection of anti-parallel vortices which initially contain axial flow. Results showed that the general features and the main stages of the process remain unchanged; however, axial flow leads to an increase in the maximum circulation transfer rate and therefore a reduction in the reconnection time. It is worth mentioning that although high initial Re was used, reconnection cascade (reconnection of threads) was not captured. This observation challenges the idea of reconnection cascade even at higher initial Re. Due to the low circulation and Re (in comparison to the circulation and Re of the initial vortices), threads' interaction is dominated by the viscous diffusion. In addition, threads are highly sensitive to the instabilities which generate multiple dipoles and facilitate viscous diffusion of small-scale vortices (threads). Such instabilities are acknowledged in [40] as asymmetries on the symmetric plane with regard to the collision plane at high Re.

By using the vortex sub-tube method, Beardsell *et al* [5] decomposed the vorticity field into the reconnected and non-reconnected sections. In the anti-parallel configuration, they detected the regions which are not located in these two sections. It was shown that such regions cover the ring structures. They associated these ring structures to the instability arising at high Re at jet-like flow. Generated dipoles have a leap-frog interaction with each other at parallel planes to the symmetric plane. Such interactions lead to off-centered viscous diffusion extrema and accordingly reconnection at both sides of the symmetric plane. At high Re such structures cause discrepancies between the integral and instantaneous reconnection level estimators. Note that the integral estimator is based on an integral quantity, i.e. circulation on the half of the symmetric plane. On the other hand, instantaneous estimator tracks the vortex lines and finds the points where they touch the boundaries of the domain; this way, it can determine the percentage of the reconnected vortex lines. Generally, integral estimators cannot capture such looping structures and underestimates reconnection level. Such looping structures at high Reynolds number have not been captured in the orthogonal configuration. However, both configurations followed the same stages, which supports the idea that physics of the reconnection is independent of the initial configurations [70, 9, 72]. Beardsell *et al* [5] also investigated the effect of the domain size on the flow evolution of the orthogonal configuration. They found that the global physics (trend of the instantaneous estimator of the reconnection level) remains unchanged. However, the influence of the neighboring vortices on the evolution of the maximum vorticity magnitude in the whole domain can be visualized by slight differences.

Because of high computational cost and asymmetries on the symmetric plane at high Re, so far, the second reconnection (reconnection of threads) has not been captured by the periodic boundary conditions. By imposing symmetric boundary conditions on the

symmetric and collision planes, Yao and Hussain [110] reported the incompressible second vortex reconnection at $Re = 9000$ which causes the generation of other small-scale structures, e.g. vortex rings, smaller-scale vortex wrap around threads, and hairpin-like vortices packets. At $Re = 40000$, they also captured the third reconnection.

1.2.4 Sound Generation Through Reconnection

Sound generation has been noted in the oblique collisions of vortex rings; the primary acoustic source originates from reconnection regions of vortex lines [49, 1, 46]. Furthermore, Nakashima [77] showed that as the collision angle decreases, reconnection and its contribution to the far-field sound intensify. On the other hand, using Lighthill's analogy [66], Scheidegger [91] failed to find a distinct far-field sound signal during the reconnection of orthogonal vortices. He noted that many source points in the reconnection region contribute to sound generation and the sound radiation is sporadic. In another attempt, Paredes *et al* [81] used Möhring's analogy [74] and large-eddy simulation (LES) to study the reconnection sound of anti-parallel vortices at high Re; however, no clear conclusion backed up by data was presented. Recently, it has been shown that the reconnection of two anti-parallel vortices produces significant far-field sound which is deterministic in the sound directivity pattern [18]. The analysis demonstrates that the main acoustic sources are located at the contact region of the vortices at the start of the reconnection and then migrate towards the bridges. In addition to viscous flow cases, sound generation during quantum vortex reconnection becomes an appealing topic, recently identified as an energy exchange and irreversibility mechanism [85, 103].

1.3 Motivation and Objectives

Many features of turbulent flows such as turbulence production, dissipation, fine-scale mixing, and noise generation are rooted in the behavior of the coherent structures and, more specifically, in their self- and mutual-interactions. In this regard, being the only known mechanism of topological change in fluid flows, vortex reconnection has emerged as an important process to understand the myriad complexities of turbulent flows and their control [110]. There are still many outstanding questions on the dynamics of reconnection. Although vorticity evolution is qualitatively the same for all subsonic reconnections [20], many aspects of compressible reconnection including the detailed roles of the supplementary vorticity generation terms, sound production mechanism, recognition and evolution of the dominant components of the acoustic source term, the near-field pressure evolution,

and far-field noise level and its directivity during the reconnection process still remain unexplored. Also, very little is known about the formation and features of shocklets near the sonic threshold and their dependence on Re.

The main objectives of this thesis are as follow:

- Characterize the sound generation mechanism of initially subsonic viscous vortex reconnection through decomposition of Lighthill's acoustic source term [66].
- Recognize the dominant components of the acoustic source term, their physical representation, and the role of compressibility on their evolution.
- Explore the features of shocklets and their importance in the sound generation.
- Study the near field pressure evolution (which is closely tied to the sound production and propagation mechanisms [13, 67]), far-field SPL and directivity pattern, and its dependence on compressibility.

Theoretical framework and numerical setup are described in Chapter 2. Chapters 3 and 4 are dedicated to the investigation of above objectives. Conclusions are drawn in Chapter 5.

Chapter 2

Theoretical Framework and Numerical Setup

This chapter consists of two sections: theoretical framework and numerical setup. In the first section, governing equations of fluid dynamics, the most useful relations of vortex dynamics, and Lighthill's inhomogeneous wave equation [66] and the decomposition of the source term are presented. In the second section, nondimensionalization, the numerical method, the problem setup, and mesh independency are discussed.

2.1 Theoretical Framework

2.1.1 Governing Equations

The conservative form of the governing equations for compressible, Newtonian fluid flow in an inertial frame of reference with zero external forces can be written as (detailed derivations including the non-conservative forms can be found in [60]):

- Conservation of mass

$$\frac{\partial \rho}{\partial t} + \frac{\partial}{\partial x_j}(\rho v_j) = 0. \tag{2.1}$$

- Conservation of momentum

$$\frac{\partial \rho v_i}{\partial t} + \frac{\partial}{\partial x_j}(\rho v_i v_j) = \frac{\partial \sigma_{ij}}{\partial x_j}. \tag{2.2}$$

- Conservation of energy

$$\frac{\partial \rho e_T}{\partial t} + \frac{\partial}{\partial x_j}(\rho e_T v_j) = \frac{\partial v_i \sigma_{ij}}{\partial x_j} - \frac{\partial q_j}{\partial x_j}. \tag{2.3}$$

ρ is density, t is time, and v_j is the velocity component in x_j direction. σ_{ij} is the stress tensor and is given as below:

$$\sigma_{ij} = -P\delta_{ij} + \tau_{ij} = -P\delta_{ij} + 2\mu S_{ij} + \lambda S_{mm}\delta_{ij}, \tag{2.4}$$

where P is the static pressure and δ_{ij} is the Kronecker delta tensor. $\tau_{ij} = 2\mu S_{ij} + \lambda S_{mm}\delta_{ij}$ is the fluid-dynamic contribution to the stress tensor and is called the deviatoric stress tensor. μ is the shear viscosity coefficient, $S_{ij} = \frac{1}{2}(\frac{\partial v_i}{\partial x_j} + \frac{\partial v_j}{\partial x_i})$ is the strain rate tensor, $\lambda = \mu_\nu - 2\mu/3$ is the second viscosity coefficient, and μ_ν is the bulk viscosity coefficient which is often assumed to be zero, $\mu_\nu = 0$, based on the Stokes assumption.
In the conservation of energy, equation 2.3, $e_T = e + \frac{1}{2}v_i v_i$ is the total energy per unit mass, e is the internal energy per unit mass, and q_j is the heat flux component in the x_j direction. It is often assumed that the heat transfer is caused by thermal conduction alone (without radiation) and it follows Fourier's law of heat conduction, $\boldsymbol{q} = -k\boldsymbol{\nabla}T$, where $\boldsymbol{q}$ is the heat flux, k is the fluid's thermal conductivity, and T is temperature. Considering a calorically perfect gas relation, $e = C_v T$ and $P = \rho R T$, where C_v is the specific heat capacity at constant volume and R is the gas constant, above conservation equations become a solvable equation set.

By using Gibbs relation, $Tds = de + Pd(\frac{1}{\rho})$, one may derive the governing equation for the evolution of entropy, s (details can be found in [100] and [28]). Isentropic relation for a calorically perfect gas can be derived directly from the Gibbs relation as $P = a\rho^\gamma$, where a is a constant and γ is the ratio of the specific heats.

2.1.2 Vortex Dynamics

The velocity gradient tensor, $\frac{\partial v_i}{\partial x_j}$, like any other tensor can be decomposed into symmetric, S_{ij}, and antisymmetric, R_{ij}, tensors:

$$\frac{\partial v_i}{\partial x_j} = S_{ij} + \frac{1}{2}R_{ij},\ S_{ij} = \frac{1}{2}(\frac{\partial v_i}{\partial x_j} + \frac{\partial v_j}{\partial x_i}),\ R_{ij} = \frac{\partial v_i}{\partial x_j} - \frac{\partial v_j}{\partial x_i}, \tag{2.5}$$

where S_{ij}, as introduced before, is the strain rate tensor and embodies the fluid element deformation. R_{ij} is the rotation tensor and embodies fluid element rotation. The rotation

tensor is an antisymmetric tensor and has only three independent elements which can be expressed by a vector. This vector is the vorticity vector, $\boldsymbol{\omega} = \boldsymbol{\nabla} \times \boldsymbol{v}$, and is related to the rotation tensor as follows:

$$R_{ij} = -\epsilon_{ijk}(\boldsymbol{\nabla} \times \boldsymbol{v})_k = -\epsilon_{ijk}\omega_k = \begin{bmatrix} 0 & -\omega_3 & \omega_2 \\ \omega_3 & 0 & -\omega_1 \\ -\omega_2 & \omega_1 & 0 \end{bmatrix}, \tag{2.6}$$

where ϵ_{ijk} is the alternating tensor or permutation symbol, and ω_i are the components of vorticity vector:

$$\omega_1 = \frac{\partial v_3}{\partial x_2} - \frac{\partial v_2}{\partial x_3},\ \omega_2 = \frac{\partial v_1}{\partial x_3} - \frac{\partial v_3}{\partial x_1},\ \omega_3 = \frac{\partial v_2}{\partial x_1} - \frac{\partial v_1}{\partial x_2}. \tag{2.7}$$

Fluid motion is called irrotational if $\boldsymbol{\omega} = 0$ or equivalently $R_{ij} = 0$. In this case, the fluid velocity can be written as the gradient of a scalar function which satisfies the condition of irrotationality. Generally, based on Helmholtz decomposition, any continuous vector field $\boldsymbol{f}$ can be globally decomposed as:

$$\boldsymbol{f} = \boldsymbol{\nabla}\phi + \boldsymbol{\nabla} \times \boldsymbol{\psi}, \tag{2.8}$$

where scalar field ϕ and solenoidal vector field $\boldsymbol{\psi}$ are known as the scalar and vector Helmholtz potentials of $\boldsymbol{f}$, respectively. Utilizing the vector identity of $\nabla^2\boldsymbol{f} = \boldsymbol{\nabla}(\boldsymbol{\nabla}.\boldsymbol{f}) - \boldsymbol{\nabla}\times(\boldsymbol{\nabla} \times \boldsymbol{f})$, one may determine ϕ and $\boldsymbol{\psi}$ by solving the Poisson equation for a given vector field $\boldsymbol{f}$:

$$\nabla^2\phi = \boldsymbol{\nabla}.\boldsymbol{f},\ \nabla^2\boldsymbol{\psi} = -\boldsymbol{\nabla} \times \boldsymbol{f}. \tag{2.9}$$

By applying Helmholtz decomposition to the velocity vector field, we can obtain the irrotational and non-solenoidal velocity, $\boldsymbol{v_C}$, and rotational and solenoidal velocity, $\boldsymbol{v_I}$:

$$\begin{aligned} \boldsymbol{\nabla}.\boldsymbol{v_C} = \boldsymbol{\nabla}.\boldsymbol{v} = \upsilon,\ \boldsymbol{\nabla} \times \boldsymbol{v_C} = 0, \\ \boldsymbol{\nabla}.\boldsymbol{v_I} = 0,\ \boldsymbol{\nabla} \times \boldsymbol{v_I} = \boldsymbol{\nabla} \times \boldsymbol{v} = \boldsymbol{\omega}, \end{aligned} \tag{2.10}$$

where $\boldsymbol{v} = \boldsymbol{v_C} + \boldsymbol{v_I}$, and υ is the dilatation. Clearly, $\boldsymbol{v_C}$ is associated with the dilatation and compression in the compressible flows; thus, it is important near strong acoustic waves and shocklets. On the other hand, $\boldsymbol{v_I}$ represents the solenoidal and rotational part of the velocity field. More specifically, the solenoidal rotational velocity, $\boldsymbol{v_I}$, which is induced by a known concentrated distribution of vorticity (a vortex) with arbitrary orientation, can be calculated by solving the following Poisson equation:

$$\nabla^2\boldsymbol{v_I} = -\boldsymbol{\nabla} \times \boldsymbol{\omega}. \tag{2.11}$$

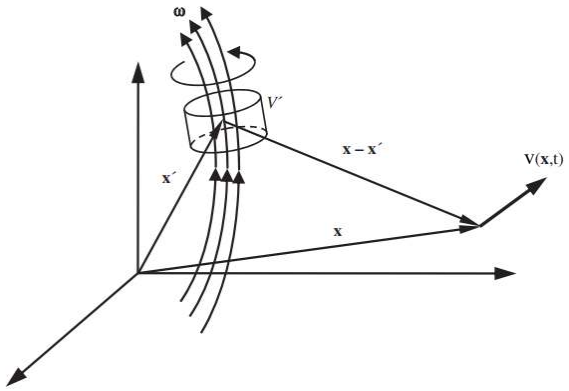

Figure 2.1: Geometry used in the description of Biot-Savart law [60].

The Biot-Savart vortex induction law expresses the vorticity-induced velocity as follows:

$$\boldsymbol{v_I}(\boldsymbol{x},t) = \frac{1}{4\pi}\int_{V'} \frac{\boldsymbol{\omega}(\boldsymbol{x'},t)\times(\boldsymbol{x}-\boldsymbol{x'})}{|\boldsymbol{x}-\boldsymbol{x'}|^3} d^3x', \tag{2.12}$$

where $\boldsymbol{x}$ is the observation location (location of the vortex-induced velocity vector), $\boldsymbol{x'}$ is the vortex (vorticity concentration) location, and V' encloses the vorticity of interest with perpendicular ends to the vorticity and lateral sides outside the vortex as depicted in Figure 2.1. The derivation details of the Biot-Savart law can be found in [60].

An equation for the vorticity, can be obtained from the curl of the momentum conservation equation. By assuming that the body forces are conservative, $\boldsymbol{g} = \boldsymbol{\nabla}\phi$, and the Stokes assumption, $\mu_\nu = 0$, is valid, the equation governing vorticity in a compressible fluid flow is obtained as below [11]:

$$\begin{aligned}\frac{D\boldsymbol{\omega}}{Dt} = &\underbrace{(\boldsymbol{\omega}.\boldsymbol{\nabla})\boldsymbol{v}}_{\text{I}} \underbrace{-\boldsymbol{\omega}(\boldsymbol{\nabla}.\boldsymbol{v})}_{\text{II}} + \underbrace{\frac{\boldsymbol{\nabla}\rho\times\boldsymbol{\nabla}P}{\rho^2}}_{\text{III}} \\ &\underbrace{\frac{\mu}{\rho}\nabla^2\boldsymbol{\omega}}_{\text{IV}} + \underbrace{\frac{\mu}{\rho^2}\boldsymbol{\nabla}\rho\times(\boldsymbol{\nabla}\times\boldsymbol{\omega})}_{\text{V}} + \underbrace{\frac{4}{3}\frac{\mu}{\rho^2}\boldsymbol{\nabla}(\boldsymbol{\nabla}.\boldsymbol{v})\times\boldsymbol{\nabla}\rho}_{\text{VI}} \\ &\underbrace{\boldsymbol{\nabla}\mu\times[\frac{4}{3}\frac{(\boldsymbol{\nabla}.\boldsymbol{v})}{\rho^2}\boldsymbol{\nabla}\rho - \frac{1}{\rho}(\boldsymbol{\nabla}\times\boldsymbol{\omega})] + \boldsymbol{\nabla}\times(\frac{1}{\rho}\boldsymbol{\xi})}_{\text{VII}},\end{aligned} \tag{2.13}$$

where $\boldsymbol{\xi} = 2\boldsymbol{S} \odot \boldsymbol{\nabla}\mu - 2/3(\boldsymbol{\nabla}.\boldsymbol{v})\boldsymbol{\nabla}\mu$ and $\boldsymbol{S}$ is the strain rate tensor. Term I on the right-hand side (RHS) represents the rate of change of vorticity caused by the stretching and tilting of vortex lines; it can be written as $(\boldsymbol{\omega}.\boldsymbol{\nabla})\boldsymbol{v} = \boldsymbol{\omega}.\boldsymbol{S}$. Term II shows the rate of change of vorticity caused by dilatation and is expected to be large near the shocks. Term III represents baroclinic vorticity generation rate. Finally, four remaining terms show the viscous effects; specifically, term IV denotes the rate of change of vorticity through diffusion of vorticity. Also, term VII shows the effect of the viscosity variation and is expected to play an important role in the dynamics of any flow with significant heat transfer –some relations of $\boldsymbol{\xi}$ are expanded in appendix A. Enstrophy (vorticity magnitude) equation can be determined by the dot product of $\boldsymbol{\omega}$ and equation 2.13.

Circulation, the amount of fluid rotation within a closed contour (or circuit) C, is defined by:

$$\Gamma = \oint_C \boldsymbol{v}.\boldsymbol{ds} = \int_A \boldsymbol{\omega}.\boldsymbol{n}dA, \tag{2.14}$$

where $\boldsymbol{ds}$ is an element of C. Using the momentum equation 2.2 and the same assumptions mentioned above, total time derivative of the circulation becomes:

$$\begin{aligned}
\frac{D\Gamma}{Dt} &= \frac{D}{Dt}\oint_C \boldsymbol{v}.\boldsymbol{ds} = \oint_C \frac{D\boldsymbol{v}}{Dt}.\boldsymbol{ds} \\
&= -\oint_C \frac{1}{\rho}\boldsymbol{\nabla}P.\boldsymbol{ds} + \oint_C \frac{1}{\rho}(\boldsymbol{\nabla}.\boldsymbol{\tau}).\boldsymbol{ds} \\
&= \underbrace{-\oint_C \frac{1}{\rho}\boldsymbol{\nabla}P.\boldsymbol{ds}}_{\text{Term 1}} \underbrace{-\oint_C \frac{\mu}{\rho}(\boldsymbol{\nabla}\times\boldsymbol{\omega}).\boldsymbol{ds}}_{\text{Term 2}} + \underbrace{\oint_C \frac{4}{3}\frac{\mu}{\rho}\boldsymbol{\nabla}(\boldsymbol{\nabla}.\boldsymbol{v}).\boldsymbol{ds}}_{\text{Term 3}} + \underbrace{\oint_C \frac{1}{\rho}\boldsymbol{\xi}.\boldsymbol{ds}}_{\text{Term 4}}.
\end{aligned} \tag{2.15}$$

Term 1 represents the baroclinic effect; Term 2 is the usual viscous term appeared in the incompressible flow; the last two terms are the viscous effect due to the dilatation and viscosity variation, respectively. Based on equation 2.15 and as Kelvin's theorem states, in a barotropic flow with conservative body forces, when the fluid is inviscid ($\mu = \mu_\nu = 0$) or the integrated viscous force ($\boldsymbol{\nabla}.\boldsymbol{\tau}$) is zero around a closed curve, the circulation around that curve moving with the fluid remains constant with time if the motion is observed from an inertial frame of reference. Therefore, there are three ways to generate or destroy vorticity in a flow: nonconservative body forces, a nonbarotropic pressure-density relationship, and nonzero net viscous torques. In this regard, Helmholtz proved that vortex lines become material lines under the same conditions of the Kelvin's theorem. More details of this theorem are provided in [60].

To model the behavior of a real vortex flow, first two ideal steady vortex flows are introduced:

1. Solid-body rotation. This flow is generated by a uniform distribution of plane-normal vorticity with magnitude ω. The velocity components in the (r, θ)-polar coordinates are given by:

$$v_r = 0,\ v_\theta = \omega r/2. \tag{2.16}$$

The circulation around an arbitrary circuit of radius r in the (r, θ)-plane can be determined as:

$$\Gamma = \oint_C \boldsymbol{v}.\boldsymbol{ds} = \int_0^{2\pi} v_\theta r d\theta = 2\pi r v_\theta = \pi r^2 \omega. \tag{2.17}$$

The strain rate tensor for this flow is zero, $\boldsymbol{S} = 0$, and fluid elements do not deform.

2. Irrotational vortex. This flow is generated by an ideal plane-normal vortex line located at the origin and produces circulation Γ around any circuit including the origin. The velocity components in the (r, θ)-polar coordinates are given by:

$$v_r = 0,\ v_\theta = \Gamma/2\pi r. \tag{2.18}$$

The strain rate tensor for this flow is nonzero, however, the vorticity at any point away from the origin is zero. It means that fluid elements only deform and do not spin.

The behavior of real vortices is a combination of the flows generated by these two ideal vortices. The flow near the core of a real vortex is approximately a solid-body rotation, but flow away from the core is almost irrotational. Two common models which are used to describe the behavior of real vortex flows are the Rankine and the Gaussian vortex flows. In the Rankine model, the transition from the solid-body rotation to irrotational vortex flow is abrupt; however, in the Gaussian model, this transition happens gradually. The details of these two models are available in [60]. In the current study, a compact Gaussian vorticity distribution (presented later in equation 2.33) with the Gaussian distribution of vorticity inside and zero outside the initial vortex tubes has been used–note that vorticity variation at the edge of the vortex tubes remains smooth.

2.1.3 Acoustic Source

Combining the time derivative of the continuity equation and divergence of the momentum equation, Lighthill's inhomogeneous wave equation is derived [66]. The homogeneous part of this partial differential equation describes acoustic wave propagation within an inviscid,

stationary fluid whereas the inhomogeneous contribution represents the summation of all source terms driving the wave. The equation can be written as follows:

$$\frac{\partial^2 \rho}{\partial t^2} - c_0^2 \nabla^2 \rho = \underbrace{\boldsymbol{\nabla .} \left[\rho(\boldsymbol{v}.\boldsymbol{\nabla})\boldsymbol{v} - \boldsymbol{v}\frac{\partial \rho}{\partial t} + (\boldsymbol{\nabla} P - c_0^2 \boldsymbol{\nabla}\rho) - \boldsymbol{\nabla .} \boldsymbol{\tau} \right]}_{\text{S}}, \tag{2.19}$$

where the left-hand side (LHS) is the wave operator with t as time, c_0 as the constant speed of sound of the stationary medium, and ρ, density, as the dependent variable. The RHS is the source term, S, where $\boldsymbol{v}$ is the velocity vector, P is the pressure, and $\boldsymbol{\tau}$ is the viscous stress tensor. Using vector identity and the continuity equation, the non-linear term and the time derivative in S can be respectively substituted as follow:

$$\rho(\boldsymbol{v}.\boldsymbol{\nabla})\boldsymbol{v} = \rho(\boldsymbol{\omega} \times \boldsymbol{v}) + \rho\frac{\boldsymbol{\nabla}|\boldsymbol{v}|^2}{2}, \tag{2.20}$$

$$-\boldsymbol{v}\frac{\partial \rho}{\partial t} = (\boldsymbol{\nabla .}(\rho \boldsymbol{v}))\boldsymbol{v}, \tag{2.21}$$

where $\boldsymbol{\omega} \times \boldsymbol{v}$ is the Lamb vector,$\boldsymbol{L}$. Using above equations, the acoustic source term can be reformulated to delineate the physical interpretation of the mechanisms causing the sound generation as:

$$\begin{aligned} \frac{\partial^2 \rho}{\partial t^2} - c_0^2 \nabla^2 \rho = &\underbrace{\boldsymbol{\nabla .} \left[\rho(\boldsymbol{\omega} \times \boldsymbol{v})\right]}_{\text{A}} + \underbrace{\boldsymbol{\nabla .} \left[\rho\frac{\boldsymbol{\nabla}|\boldsymbol{v}|^2}{2}\right]}_{\text{B}} + \underbrace{\boldsymbol{\nabla .} \left[(\boldsymbol{\nabla .}(\rho\boldsymbol{v}))\boldsymbol{v}\right]}_{\text{C}} \\ &+ \underbrace{(\nabla^2 P - c_0^2 \nabla^2 \rho)}_{\text{D}} \underbrace{-\boldsymbol{\nabla .}[\boldsymbol{\nabla .}\boldsymbol{\tau}]}_{\text{E}}. \end{aligned} \tag{2.22}$$

This reformulation of the Navier-Stokes equations, equation 2.22, is exact and, unlike standard aeroacoustic analogies, all acoustic source terms are preserved. The wave operator can also be written in terms of pressure as the dependent variable; however, since it is computationally inefficient, we proceed with the above form of Lighthill's equation. The decomposed terms in equation 2.22 are tractable and amenable to a physical interpretation. Term A denotes the role of the divergence of the Lamb vector, term B is related to the spatial variation of the kinetic energy, term C contains interactions involving the gradient of density and the dilatation field, term D is the deviation from the isentropic condition, and term E contains the viscous effects. Through a further expansion of each of these

terms, the individual contribution of the velocity, vorticity, dilatation, and density, and their mutual interactions can be delineated even more:

$$\underbrace{\boldsymbol{\nabla}.[\rho(\boldsymbol{\omega}\times\boldsymbol{v})]}_{\text{A}} = \underbrace{(\rho\boldsymbol{v}).(\boldsymbol{\nabla}\times\boldsymbol{\omega})}_{\text{A1}} + \underbrace{\boldsymbol{v}.(\boldsymbol{\nabla}\rho\times\boldsymbol{\omega})}_{\text{A2}}\ \underbrace{-\rho(\boldsymbol{\omega}.\boldsymbol{\omega})}_{\text{A3}}, \tag{2.23}$$

$$\underbrace{\boldsymbol{\nabla}.\left[\rho\frac{\boldsymbol{\nabla}|\boldsymbol{v}|^2}{2}\right]}_{\text{B}} = \underbrace{\rho\nabla^2\left(\frac{|\boldsymbol{v}|^2}{2}\right)}_{\text{B1}} + \underbrace{\boldsymbol{\nabla}\rho.\boldsymbol{\nabla}\frac{|\boldsymbol{v}|^2}{2}}_{\text{B2}}, \tag{2.24}$$

$$\begin{aligned}\underbrace{\boldsymbol{\nabla}.[(\boldsymbol{\nabla}.(\rho\boldsymbol{v}))\boldsymbol{v}]}_{\text{C}} = &\underbrace{\rho\boldsymbol{v}.\boldsymbol{\nabla}(\boldsymbol{\nabla}.\boldsymbol{v})}_{\text{C1}} + \underbrace{\rho(\boldsymbol{\nabla}.\boldsymbol{v})^2}_{\text{C2}} + \underbrace{2(\boldsymbol{\nabla}.\boldsymbol{v})\boldsymbol{v}.\boldsymbol{\nabla}\rho}_{\text{C3}} \\ &+ \underbrace{\boldsymbol{v}.(\boldsymbol{v}.\boldsymbol{\nabla}\boldsymbol{\nabla}\rho)}_{\text{C4}} + \underbrace{\boldsymbol{v}.(\boldsymbol{\nabla}\rho.\boldsymbol{\nabla}\boldsymbol{v})}_{\text{C5}},\end{aligned} \tag{2.25}$$

$$\underbrace{(\nabla^2 P - c_0^2\nabla^2\rho)}_{\text{D}} = \underbrace{\nabla^2 P}_{\text{D1}}\ \underbrace{-c_0^2\nabla^2\rho}_{\text{D2}}, \tag{2.26}$$

$$\underbrace{-\boldsymbol{\nabla}.[\boldsymbol{\nabla}.\boldsymbol{\tau}]}_{\text{E}} = \underbrace{-\frac{4}{3}\mu\nabla^2(\boldsymbol{\nabla}.\boldsymbol{v})}_{\text{E1}}\ \underbrace{-\boldsymbol{\nabla}\mu.\left[\frac{4}{3}\boldsymbol{\nabla}(\boldsymbol{\nabla}.\boldsymbol{v}) - \boldsymbol{\nabla}\times\boldsymbol{\omega}\right] - \boldsymbol{\nabla}.\boldsymbol{\xi}}_{\text{E2}}. \tag{2.27}$$

Let us consider the terms in the above reformulation. If the flow is assumed to be inviscid, incompressible, and isentropic, only terms A1, A3, and B1 remain–some part of term E2 due to viscosity variation, if any, also remains. Term A1 is the flexion product and is primarily positive since it represents a dissipative mechanism with a minus sign in the kinetic energy transport equation of incompressible flow [31]:

$$\frac{1}{2}\frac{\partial|\boldsymbol{v}|^2}{\partial t} = -\boldsymbol{v}.\boldsymbol{\nabla}\phi - \nu\boldsymbol{v}.(\boldsymbol{\nabla}\times\boldsymbol{\omega}), \tag{2.28}$$

where $\phi = P/\rho + |\boldsymbol{v}|^2/2$ and ν are the Bernoulli function and kinematic viscosity, respectively. The flexion product has been also considered as an unwinding term, converting the angular momentum in a vortex into linear momentum, thus attenuating the low pressure in the vortex core [31]. Further, it can be related to the Laplacian of the solenoidal velocity vector by $\boldsymbol{v}.(\boldsymbol{\nabla}\times\boldsymbol{\omega}) = -\boldsymbol{v}.\nabla^2\boldsymbol{v}$; see Figure 2.2 for a qualitative orientation of the velocity and flexion (curl of vorticity) vectors at the edge of a vortex tube with Gaussian vorticity

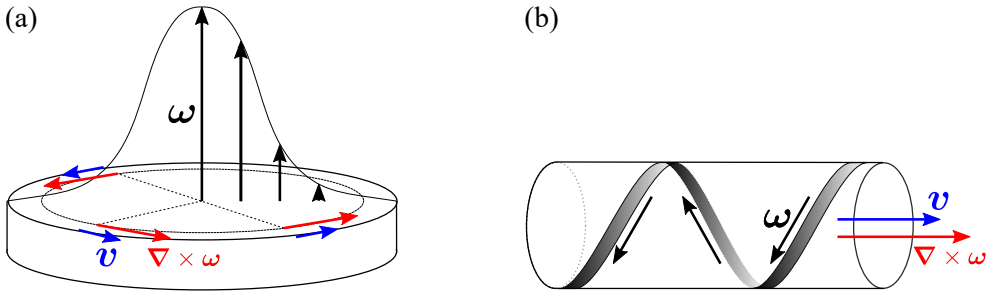

Figure 2.2: Qualitative orientation of the velocity and flexion vectors (a) at the edge of a vortex tube with Gaussian vorticity distribution and (b) in the core of a twisted vortex tube, resulting in an unwinding of the vortex line.

distribution and in the core of a twisted vortex tube.
Term A3 is enstrophy and its contribution to the source term is always negative. Term B1 is the Laplacian of the kinetic energy highlighting the role of the kinetic energy deviation from its local average in the sound production. Given the satisfactory results of the low-M approximation in sound predictions [29], it is natural to conjecture that terms A1, A3, and B1 are the dominant hydrodynamic sources of sound. In this regard, Cabana *et al* [10] solved a one-dimensional (1D) wave equation for each of the decomposed source terms (except the viscous terms) and showed that terms A2 and B2 are also important in sound production in a mixing-layer. They categorized terms A and B as production terms, and term C–involving interactions of density, velocity, and dilatation fields–as the acoustic term responsible for the sound propagation. Furthermore, vortex sound analogies consider only terms A and B providing suitable sound predictions [83]–in high-Re, low-M flows, while term B is often neglected.

Although the aeroacoustic analogies (e.g. Lighthill's [66], Powell's [83], or Möhring's [74]) hinge on an *ad hoc* simplification of the acoustic source term and the decoupling of the sound production and propagation mechanisms, elimination of any physical subtleties in the acoustic-hydrodynamic interactions could affect accurate assessment of the propagated sound [13]. For instance, in Powell's low-M analogy (without external force field and neglecting viscous-thermal effects) [83], only term A ($\boldsymbol{\nabla}.[\rho(\boldsymbol{\omega}\times\boldsymbol{v})]$) is kept and all other source terms in equation 2.22 are eliminated (note that in Powell's analogy pressure is considered as the dependent variable). Then, using the Green's function, an integral solution for the far-field pressure perturbation is found:

$$P'(\boldsymbol{x},t) = -\frac{\rho_\infty}{4\pi c_\infty^2|\boldsymbol{x}|^3}\frac{\partial^2}{\partial t^2}\int\int\int_V (\boldsymbol{x}.\boldsymbol{y})\boldsymbol{x}.(\boldsymbol{\omega}\times\boldsymbol{v})_{t^*}d^3\boldsymbol{y}, \tag{2.29}$$

where $\boldsymbol{x}$ is the probing position vector, t is time, ρ_∞ and c_∞ are respectively the density and speed of sound at far field, $\boldsymbol{y}$ is the source position vector, and V is the 3D domain. Note that the Lamb vector $(\boldsymbol{\omega} \times \boldsymbol{v})$ is calculated at the retarded time, $t^* = t - \boldsymbol{x}/c_\infty$. Computation of this integral is still very expensive. To facilitate the computations, the second time derivative of the Lamb vector is recognized as the dominant term in the above equation and its magnitude isosurface (isosurface of $|\partial^2(\boldsymbol{\omega} \times \boldsymbol{v})/\partial t^2|$) is visualized to locate the approximate sound sources [104, 105, 18].

In this thesis, first, the evolution of the entire source term and its dominant components are analyzed, and then, approximate sound sources during reconnection are visualized.

2.2 Numerical Setup

2.2.1 Nondimensionalization

Density-Temperature-Velocity (DTV) scheme [75] is used to nondimensionalize the governing equations. First, a reference point is selected and is shown by subscript o. Then, reference parameters are set as follow:

$$\rho_{ref} = \rho_o,\ T_{ref} = T_o,\ V_{ref} = v_o, \tag{2.30}$$

where ρ_o, T_o, and v_o are the density, temperature, and velocity magnitude at the reference point. Other reference parameters can be set as:

$$P_{ref} = \rho_{ref} V_{ref}^2,\ R_{ref} = V_{ref}^2/T_{ref},\ e_{ref} = V_{ref}^2, \tag{2.31}$$

where P_{ref}, R_{ref}, and e_{ref} are the reference pressure, gas constant, and internal energy, respectively. Considering above parameters, dimensionless variables (depicted by star sign, *) at the reference point are given by:

$$\begin{aligned} &\rho_o^* = 1,\ T_o^* = 1,\ v_o^* = 1,\ P_o^* = \frac{1}{\gamma M_o^2}, \\ &R_o^* = \frac{1}{\gamma M_o^2},\ \mu_o^* = \frac{1}{Re},\ k_o^* = \frac{C_P^* \mu_o^*}{Pr} \end{aligned} \tag{2.32}$$

where $M_o = \frac{v_o^*}{c_o^*}$ is the reference Mach number, $c_o^* = \sqrt{\gamma R_o^* T_o^*} = \sqrt{\gamma P_o^*/\rho_o^*}$ is the reference speed of sound, $C_P^* = \frac{\gamma R_o^*}{\gamma - 1}$ is the specific heat capacity at constant pressure, and Pr is the Prandtl number–note that, hereafter, all variables are dimensionless and will be used without sign *. More details of the nondimensionalization of the compressible Navier-Stokes equations can be found in [75].

2.2.2 Numerical Method

In the current research, high-fidelity DNS of the compressible Navier-Stokes equations is conducted using a highly scalable C++ MPI solver named Hybrid [62, 47, 6]. Considering zero external forces and zero bulk viscosity, the Hybrid code solves the conservative form of the compressible Navier-Stokes equations presented in Section 2.1.1. Note that a power-law relation is used for the dynamic viscosity, i.e. $\mu = \mu_o(T/T_o)^{3/4}$, where μ_o and T_o are the reference dynamic viscosity and temperature, respectively. Also, thermodynamic variables follow the ideal gas equation, $P = \rho RT$.

In addition to the domain size, grid data, and time step, the Hybrid code requires the ratio of the specific heats, gas constant, Prandtl number, reference dynamic viscosity, and reference temperature as inputs. The solver uses a fourth-order Runge-Kutta scheme for time integration and a sixth-order finite difference scheme for spatial derivatives combined with a high-order filtering [23]. This high-order numerical scheme with filtering has been validated for problems with acoustic wave propagation. The Hybrid code uses structured grids and is only applicable for problems with simple boundaries, which could be considered as its main drawback.

The accuracy and validation of the Hybrid code is thoroughly addressed in [47]. The code is efficiently parallelized and hyperthreading is also available through MPI. By using almost two million cores on the Blue Gene/Q systems, weak and strong scaling and the efficiency of the hyperthreading of the code were investigated in [6]; it was showed that the code scales extremely well. The strong scalability is defined as the variation of the simulation speed (completed steps per time) while increasing the number of processors for a constant size of a problem. An ideal strong scalability refers to the situation which as the number of the processors is doubled, the simulation speed increases by a factor of two. The strong scaling efficiency is determined as $E = \frac{N_0}{N}\frac{t_0}{t}$, where N is the number of the processors and t is the required time for completion of one step. Subscript 0 refers to the case with the smallest number of the processors. For the current research, the strong scalability of the Hybrid code was examined on the Compute Canada clusters at Niagara SciNet. For this purpose, isotropic turbulence case with periodic boundary conditions is simulated. Strong scalability of the code in the absence of multithreading is implemented for four grids and the results are shown in Figure 2.3. As expected, the minimum efficiency 66% is for the coarsest grid (256^3); by using finer grids efficiency highly improves, namely 95%, 95%, and 98% for 512^3, 1024^3, 2048^3 grids, respectively.

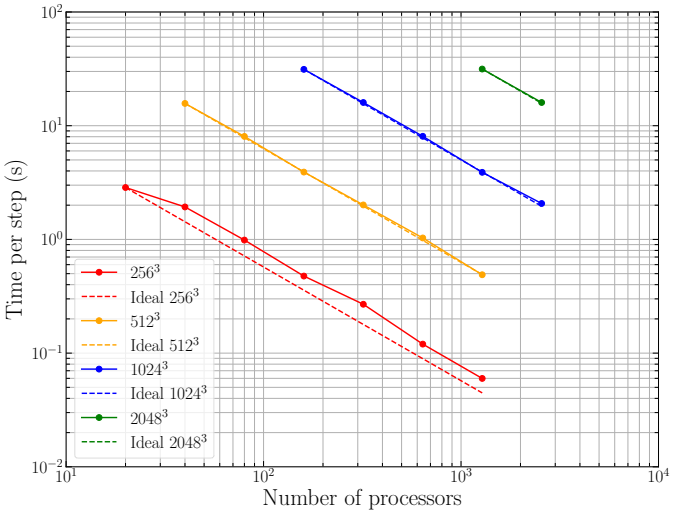

Figure 2.3: Parallel scalability analysis of the Hybrid code on Niagara SciNet cluster with Intel Skylake cores at 2.4GHz (CPU), EDR Infiniband network in a so-called 'Dragonfly+' topology (interconnection), Intel v2018.2 (compiler), and openmpi v3.1.0 (MPI library).

2.2.3 Problem Setup

As stated in Section 1.2, thus far, reconnection has been studied on different configurations, e.g. vortex rings [56] and orthogonal vortices [9], and anti-parallel vortices with a localized perturbation [70]. It has been shown that mutual induction between two approaching vortex filaments leads to the local anti-parallel orientation [98, 54, 55], and as a result, the anti-parallel configuration could be considered as the representative canonical flow of reconnection revealing the underlying physics of this phenomenon. Also, this simple setup, which can be thought of as an abstraction of a Crow instability [17], isolates the reconnection enabling high-resolution simulations and emergence of the fundamental features.

Using the same numerical setup as [18], initial anti-parallel vortex tubes with a sinusoidal perturbation are simulated in a large computational domain. Initial vorticity field

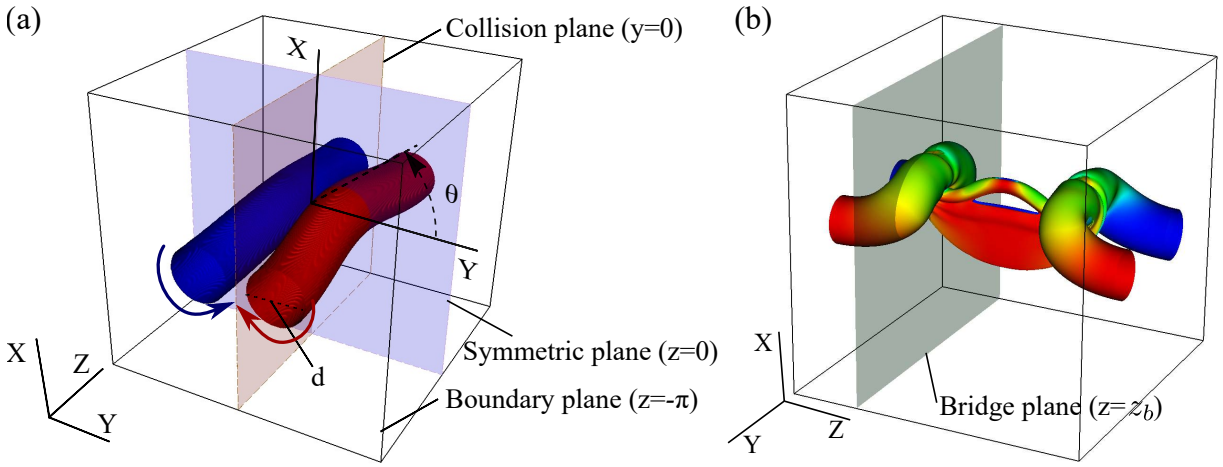

Figure 2.4: (a) Initial configuration. (b) Bridge plane.

follows the compact Gaussian vorticity distribution [106, 70] given by:

$$
\begin{aligned}
&\boldsymbol{\omega}(\boldsymbol{x}) = \omega(r)(-A\sin(\alpha)\sin(z)\boldsymbol{i} + A\cos(\alpha)\sin(z)\boldsymbol{j} + \boldsymbol{k}) \\
&\omega(r) = \begin{cases} 10[1 - f(r/r_c)], & r < r_c \\ 0, & r \geqslant r_c \end{cases} \\
&r^2 = (x - x_c - A\sin(\alpha)\cos(z))^2 + (y - y_c + A\cos(\alpha)\cos(z))^2 \\
&f(\eta) = \exp[-K\eta^{-1}\exp(1/(\eta - 1))], \qquad K = \frac{1}{2}\exp(2)\log(2),
\end{aligned}
\tag{2.33}
$$

where A is the sinusoidal perturbation amplitude, α is the inclination angle, r_c is the radius, and $(x_c + A\sin(\alpha)\cos(z), y_c - A\cos(\alpha)\cos(z), z)$ is the center of the vortex tube. In the current study these parameters are set as: $A = 0.2$, $\alpha_1 = \pi/3$, $\alpha_2 = 2\pi/3$, $r_c = 0.65$, $x_{c1} = x_{c2} = 0$, $y_{c1} = 0.75$, and $y_{c2} = -0.75$, leading to two anti-parallel perturbed vortices at the middle of a large computational domain; see Figure 2.4(a). The perturbation without a gap between the compact vortex cores in the kink section localizes the reconnection event. Figure 2.4(a) also shows characteristic planes, i.e. symmetric plane ($z = 0$), boundary plane ($z = -\pi$), and collision plane ($y = 0$). The bridge plane is defined as $z = z_b$, where z_b locates the maximum ω_y on the collision plane and $-\pi < z_b < 0$; see Figure 2.4(b). Top and side views of the initial axial vorticity are shown in Figure 2.5(a) and (b), respectively. The initial vorticity distribution for each vortex tube versus the radial distance from the core axis is depicted in Figure 2.5(c); note the Gaussian distribution of vorticity inside and zero outside the vortex tube.

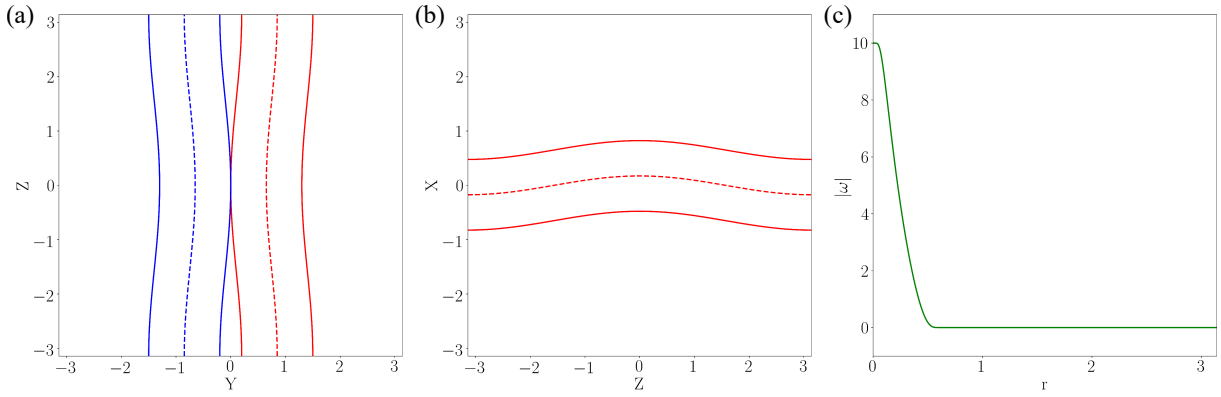

Figure 2.5: (a) Top and (b) side view of initial axial vorticity distribution. Red and blue colors respectively show positive and negative axial vorticity. Core axis is depicted with dash line. (c) Initial vorticity distribution versus the radial distance from the core axis.

To analyze the far-field sound, two sets of 192 equidistant probing points with circular layout are considered on symmetric and boundary planes; the centers of the circles are respectively at $(x_s, 0, 0)$ and $(x_s, 0, -\pi)$, where $x_s = 1.38$ is the x with the maximum absolute value of the source term at the beginning of the circulation transfer at $M_o = 0.5$– the location is the same for all M_o under consideration. Note that post-processing of case $M_o = 0.5$ consists of two steps; first, x_s is found and then, probing points are set and far-field sound is analyzed. There is not a clear interface between the near field and far field. To be far enough from the vortices and prevent effects of the reflected acoustic waves on the data collected at the probing points (discussed in the next paragraph) at the lowest M_o, the probing points are located on a circle of radius $R = 4.8d$, where $d = 2r_c$ is the diameter of the initial vortex tubes; see Figure 2.6.

Periodic boundary conditions are implemented in all three directions. To avoid polluting the data collected at the probing points by information across the periodic boundaries, the computational domain is well extended in the advection (x) and lateral (y) directions. Considering the higher relative speed of sound at lower M_o, the domain size is set to $66\pi \times 66\pi \times 2\pi$ for $M_o = 0.1$ and $28\pi \times 28\pi \times 2\pi$ for all other M_o. The mesh size of the inner $(2\pi)^3$ domain is 384^3, which is consistent with the mesh independence at $Re = 1500$ [18]. By applying expansion *growth ratio* $= 1.01$ for the surrounding domain (note that this is a small growth ratio in order to minimize dispersion/dissipation of the acoustic waves in the far field), the final resolution becomes $1212 \times 1212 \times 384$ for $M_o = 0.1$ and $1036 \times 1036 \times 384$ for all other M_o.

To minimize the initial acoustic transients and capture the salient features at early

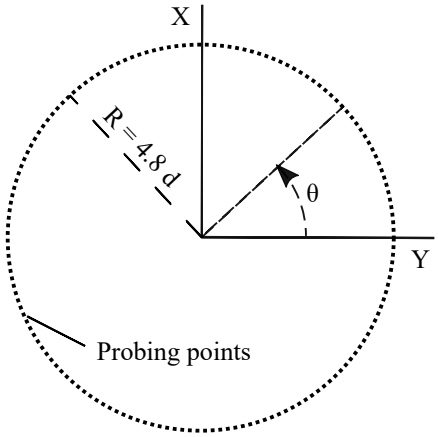

Figure 2.6: Probing points on the symmetric and boundary planes. This figure is a modified version of figure 1 of [18].

stages of compressible reconnection, we use PIC proposed by [107]. Using the initial vorticity distribution (equation 2.33), the velocity field is determined by solving the Poisson equation:

$$\nabla^2 \boldsymbol{v} = -\boldsymbol{\nabla} \times \boldsymbol{\omega}. \tag{2.34}$$

The velocity field is then normalized by the maximum velocity (the point with the maximum velocity is considered as the reference point and is denoted by the subscript o). Imposing incompressible and inviscid flow assumptions, the Poisson equation for the pressure term can be derived by taking the divergence of the momentum equation, i.e.:

$$\boldsymbol{\nabla}.(\boldsymbol{\nabla} P/\rho) = -\boldsymbol{\nabla}.[(\boldsymbol{v}.\boldsymbol{\nabla})\boldsymbol{v}]. \tag{2.35}$$

Then, density is substituted by a polytropic relation:

$$\rho = (P/P_o)^{1/\gamma}. \tag{2.36}$$

Recall that $P_o = 1/\gamma M_o^2$ is the pressure at the reference point, $\gamma = 1.4$ is the ratio of the specific heats, and M_o is the Mach number at the reference point. The Poisson equation 2.35 provides the pressure difference; the pressure field is updated such that pressure at the reference point becomes P_o. Finally, density is calculated by the polytropic relation (equation 2.36) satisfying $\rho_o = 1$. Thermodynamic variables follow the ideal gas equation, $P = \rho RT$, where $R = P_o$ is the gas constant, implying $T_o = 1$. The initial velocity field is the same for all cases studied in this thesis; to get different M_o we change P_o leading to the modification of the speed of sound at the reference point

(recall that $c_o = v_o/M_o = \sqrt{\gamma P_o/\rho_o}$, where $v_o = 1$ is the velocity at the reference point). In the current study, we consider five different subsonic reference Mach numbers: $M_o = 0.1, 0.3, 0.5, 0.7$, and 0.9. Time step used in the Hybrid code for each case respectively equals $dt = 0.00125, 0.0025, 0.005, 0.005$, and 0.005.

The vortex Reynolds number is defined as $Re = \Gamma_0/\nu_o$, with Γ_0 the initial circulation of either vortex and ν_o the kinematic viscosity at the reference point. The dynamic viscosity obeys the power-law relation, $\mu = \mu_o(T/T_o)^{3/4}$, where $\mu_o = \rho_o\nu_o$. In the current research, the sound generation of the vortex reconnection is studied at $Re = 1500$.

The reference length and time are taken to be unity. Time t_0 represents the time just before the beginning of the circulation transfer. Start time, t_S, and end time, t_E, are defined as the times when the circulation on half of the symmetric plane ($z = 0, y > 0$) becomes $\Gamma = 0.95\Gamma_0$ and $\Gamma = 0.05\Gamma_0$, respectively. The reconnection time, t_R, is the time required for the reduction of the circulation on half of the symmetric plane from $\Gamma = 0.95\Gamma_0$ to $\Gamma = 0.50\Gamma_0$. Furthermore, the maximum time, t_M, is defined as the moment when the absolute value of the acoustic source term becomes maximal (after the start of reconnection $t_M > t_S$) within the computational domain.

2.2.4 Mesh Independency

Before any discussion about the results, mesh independency of the problem is investigated. For this purpose, reconnection of two anti-parallel vortices is simulated in a small, $2\pi^3$, domain for $M_o = 0.5$ and $Re = 1500$ and 6000, on four different grids.

For $Re = 1500$, four grids, 128^3, 256^3, 384^3, and 512^3 are used. Figure 2.7(a) shows the evolution of the maximum pressure versus time for the mentioned grids. Considering the finest grid as the exact solution, $L2$ error ($1/n\sqrt{\Sigma_{i=1}^{n} e_i^2}$, where n is the total number of discrete data and e_i is the difference between the simulated and exact values at point i) takes the value of 3.7×10^{-4}, 2.6×10^{-4}, and 8.6×10^{-5}, on grids 128^3, 256^3, and 384^3, respectively. The same analysis is applied for the maximum local Mach number (M_{max}). Figure 2.7(b) shows the evolution of the M_{max} versus time. $L2$ error takes the value of 6.1×10^{-4}, 1.4×10^{-4}, and 4.4×10^{-5}, on grids 128^3, 256^3, and 384^3, respectively. $L2$ error data for this case is summarized in Table 2.1. Both of these analyses clearly confirm the mesh independency at $Re = 1500$.

For $Re = 6000$, four grids, 512^3, 640^3, 768^3, and 1024^3 are used and the same analysis is implemented. Figure 2.8(a) shows the evolution of the maximum pressure versus time for the mentioned grids. $L2$ error takes the value of 8.9×10^{-6}, 4.5×10^{-6}, and 2.1×10^{-6}, on grids 512^3, 640^3, and 768^3, respectively. Figure 2.8(b) shows the evolution of the M_{max}

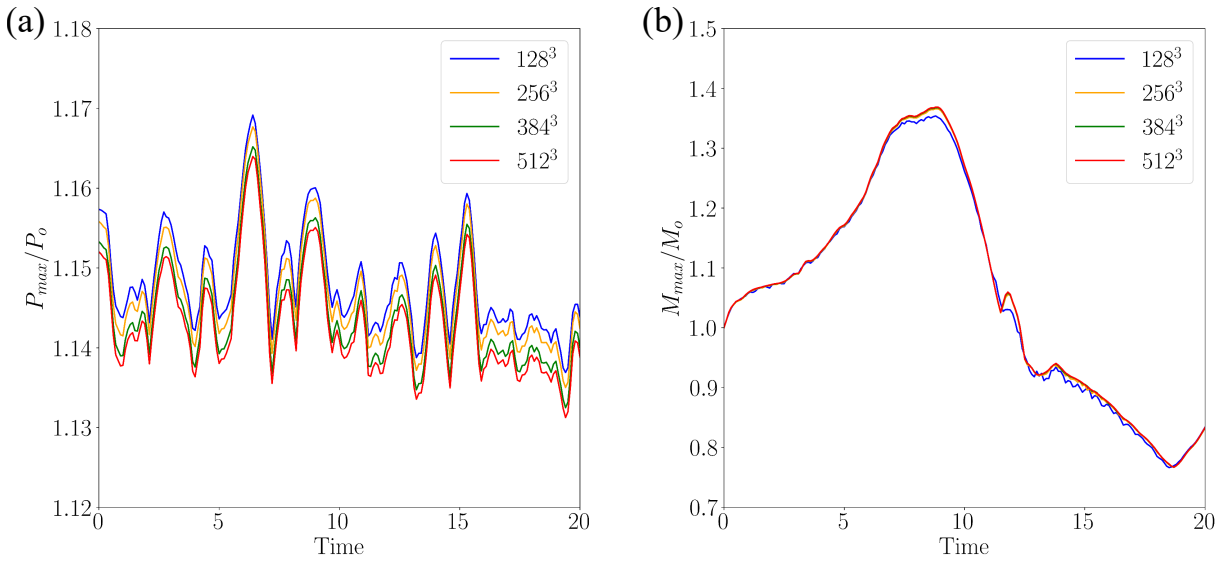

Figure 2.7: Mesh independency for the case with $Re = 1500$ and $M_o = 0.5$ through evolution of the (a) maximum pressure and (b) M_{max}.

	128^3	256^3	384^3
$L2$ error of P_{max}	3.7×10^{-4}	2.6×10^{-4}	8.6×10^{-5}
$L2$ error of M_{max}	6.1×10^{-4}	1.4×10^{-4}	4.4×10^{-5}

Table 2.1: $L2$ error data on different grids for the case with $Re = 1500$ and $M_o = 0.5$.

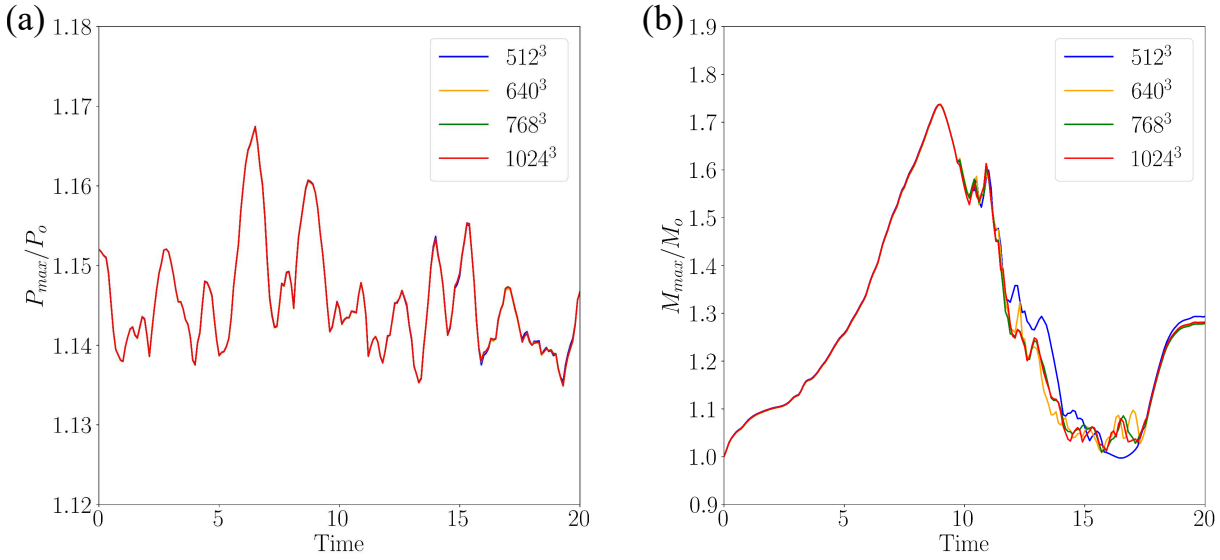

Figure 2.8: Mesh independency for the case with $Re = 6000$ and $M_o = 0.5$ through evolution of the (a) maximum pressure and (b) M_{max}.

	512^3	640^3	768^3
$L2$ error of P_{max}	8.9×10^{-6}	4.5×10^{-6}	2.1×10^{-6}
$L2$ error of M_{max}	2.2×10^{-3}	1.1×10^{-3}	5.6×10^{-4}

Table 2.2: $L2$ error data on different grids for the case with $Re = 6000$ and $M_o = 0.5$.

versus time for the same grids. $L2$ error takes the value of 2.2×10^{-3}, 1.1×10^{-3}, and 5.6×10^{-4}, on grids 512^3, 640^3, and 768^3, respectively. $L2$ error data for this case is summarized in Table 2.2. These analyses also confirm the mesh independency at a higher Re.

It is worth mentioning that M_{max} is a very sensitive criterion for the mesh independency analysis as it is dependent on both local velocity and thermodynamic variables. By comparing with $Re = 1500$, Figure 2.7(b), it is obvious that this sensitivity intensifies as Reynolds number increases. After the bridging stage and once the small-scale structures (threads) emerge, the role of the grid size becomes important. It is clear that the grid resolution at 512^3 is not a good option for the simulation of reconnection at $Re = 6000$ since it cannot capture the behavior of the small-scale structures.

Chapter 3

Sound Generation Mechanism

In this chapter, the sound generation mechanism of initially subsonic viscous reconnection through decomposition of Lighthill's acoustic source term [66] is studied. First, characteristic times and M_{max} evolution of different reference Mach numbers, M_o, are compared. Then, the dominant components of the source term are recognized; the role of compressibility on their evolutions, physical representation, mutual cancellation, and spatial distribution are investigated. Using Powell's aeroacoustic analogy [83] approximate sound sources are explored. Finally, the shocklets near the sonic threshold and their importance in sound generation are characterized.

3.1 Characteristic Times and Local Mach Number

Table 3.1 shows the characteristic times for the different M_o. An increase of M_o postpones reconnection in these initially subsonic cases. More precisely, t_S and t_E rise as M_o increases. Yet, with the exception of the $M_o = 0.9$ case, the time required for the circulation transfer during subsonic reconnection (t_R and $t_E - t_S$) is independent of M_o; however, $t_M - t_E$ increases with M_o. Recall that t_S and t_E are respectively the start and end of reconnection; t_R is the reconnection time defined as the time required for the reduction of the circulation on half of the symmetric plane from $\Gamma = 0.95\Gamma_0$ to $\Gamma = 0.50\Gamma_0$ and t_M is the maximum time showing the moment when the absolute value of the acoustic source term becomes maximal ($t_M > t_S$); see Section 2.2.3 for more details.

The reduction of t_0 at $M_o = 0.9$ is due to the formation of shocklets which lead to an earlier circulation transfer–Virk *et al* [106] observed the initial circulation transfer due to

	Characteristic moments							Characteristic intervals		
M_o	t_0	t_S	$t_S + 1.5t_R$	t_E	t_M	$t_E + 2t_R$	$t_E + 4t_R$	t_R	$t_E - t_S$	$t_M - t_E$
0.1	6.34	7.16	9.14	9.62	9.91	12.62	15.62	1.50	2.46	0.29
0.3	6.41	7.26	9.24	9.71	10.01	12.69	15.67	1.49	2.45	0.30
0.5	6.56	7.44	9.42	9.88	10.25	12.88	15.88	1.50	2.44	0.37
0.7	6.75	7.70	9.69	10.13	10.90	13.15	16.17	1.51	2.43	0.77
0.9	4.29	7.83	10.16	10.58	11.57	14.26	17.94	1.84	2.75	0.99

Table 3.1: Characteristic times for different M_o.

shock formation in the supersonic regime. However, these shocklets (at the current Re) are not strong enough to modify the reconnection process. The shocklet formation (discussed in Section 3.6) stems from the jet flow on the collision plane which is intensified as the two vortices approach each other by self-induction. Intensification of the M_{max} during reconnection can be seen in Figure 3.1(a). For $M_o = 0.9$, prior to the start of reconnection, M_{max} crosses the sonic threshold and rises up to $M_{max} \approx 1.6$; the extremum of other cases takes place just after t_S. Once reconnection begins, the reversed flow induced by the reconnected vortex lines, which are accumulated at the bridges, slows down the jet flow and impedes further growth of the local Mach number (while also slowing down the tenting phenomenon of the vortex pair, hence slowing their collision and also the circulation transfer rate). By considering only the states after the start of reconnection, Figure 3.1(b) shows a linear scaling of the overall maximum local Mach number, $M_{overall\,max} \approx 1.5M_o$, at $Re = 1500$; *overall max* refers to the maximum over the time period of $[t_S, t_E + 4t_R]$–note that $t_E + 4t_R$ represents a long time after reconnection. M_{max} does not necessarily always occur at the same location. Figure 3.2 shows the evolution of the regions with a high local Mach number for the $M_o = 0.5$ case. Initially located at the contact point between the vortices, they gradually migrate towards the bridges; owing to the initial jet flow followed by the sharp cusp-induced rapid repulsion of the bridges, high velocity is expected at theses areas. Note that due to the qualitative similarities in all the initially subsonic reconnection cases at $Re = 1500$, we observe the same general local Mach number distribution at other cases after t_S (discussed in Section 3.2).

It is expected that shocklets become stronger at higher Re as the jet flow between the two vortices intensifies before the start of reconnection–this complex issue is outside the scope of this thesis. It is also speculated that these shocklets may be a defining feature of the reconnection mechanism at high Re, which not only alter the reconnection dynamics, but can also play a significant role in sound generation. Except Section 3.6, where the

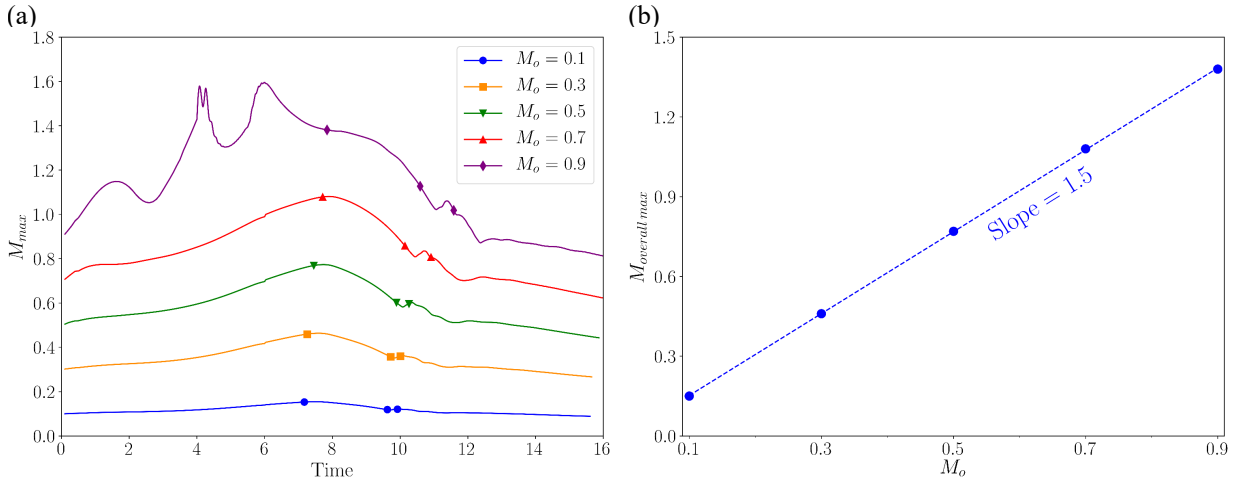

Figure 3.1: (a) Evolution of M_{max}. Markers represent t_S, t_E, and t_M. (b) Scaling of $M_{overall\,max}$.

characteristics of of the shocklets are explored, in the remaining sections, the discussion is limited to the period after the start of the reconnection, i.e. after t_S.

3.2 Acoustic Source Term

The order of magnitude of the convective term in the wave operator of the Lighthill's equation (LHS of the equation 2.19) depends on the square of the reference speed of sound. As a result, in all scale analyses, we consider the relative source term, divided by c_o^2. The evolution of the extrema (minimum and maximum at each time) of the source term in equation 2.19 at different M_o is presented in Figure 3.3. Apart from the initial oscillations at $M_o = 0.9$ which is tied to the formation of shocklets, the most obvious commonality among all cases is the amplification of the source strength during reconnection; see the magnified section of Figure 3.3.

Just after t_E, once circulation transfer is complete, the accumulation of the cusped reconnected vortex lines reinforces the self-induced rapid repulsion of the fully-developed bridges, culminating in the maximum absolute value of the source term at t_M. Linear growth of the overall extrema and maximum amplitude (largest difference between the local minimum and maximum) of the source term with respect to M_o is evident in Figure 3.4;

To identify the dominant components of the source term, we examine the respective

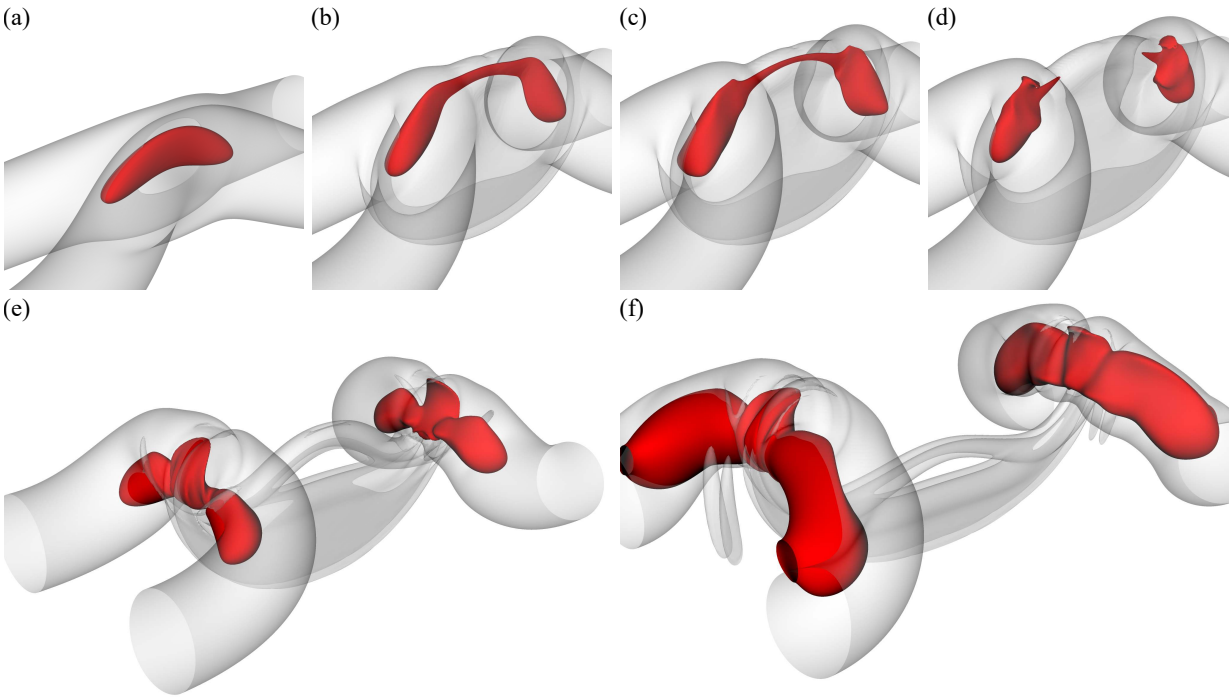

Figure 3.2: Local Mach number isosurface (red color) of $M_o = 0.5$ set at 80% of its maximum value at (a) t_S, (b) $t_S + 1.5t_R$, (c) t_E, (d) t_M, (e) $t_E + 2t_R$, and (f) $t_E + 4t_R$. Gray transparent color shows the enstrophy isosurface set at 2% of the overall maximum enstrophy. A magnified view is presented in the last two panels.

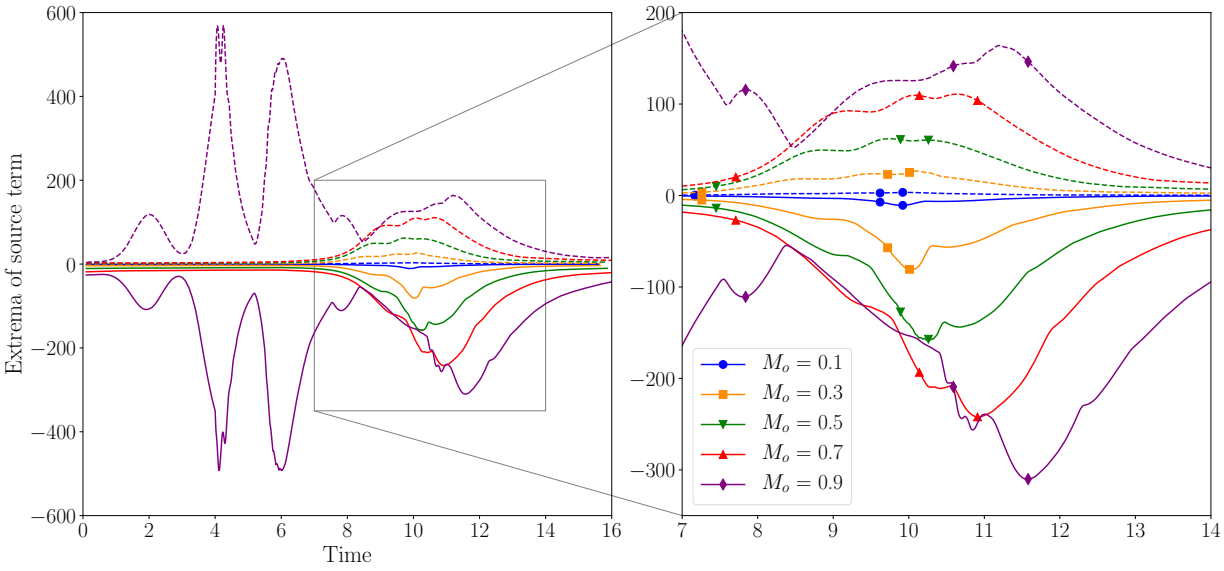

Figure 3.3: Evolution of the minimum (solid line) and maximum (dashed line) of the source term. Markers represent t_S, t_E, and t_M.

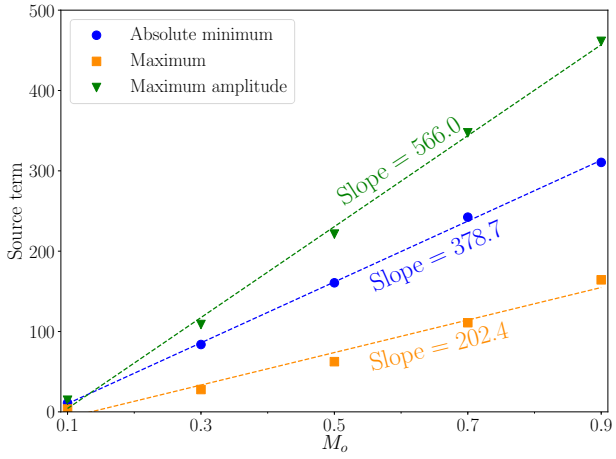

Figure 3.4: Scaling of the overall extrema and maximum amplitude of the source term.

contribution of each term on the RHS of equation 2.22 through an order-of-magnitude analysis. The extrema evolution of these terms at different M_o is provided in Figure 3.5; similar to the source term (S), the amplifications of the individual components during reconnection are quite different. Term A, the divergence of the Lamb vector, and term B, chiefly related to the Laplacian of the kinetic energy, are the dominant hydrodynamic components–these terms are also considered as the main sound production mechanisms in the vortex sound analogy [83]. Term D, the deviation from the isentropic condition, also has a notable contribution; this term is generally neglected in aeroacoustic analogies [83]. Terms C and E, respectively containing dilatation and viscous effects, become negligible after the start of reconnection (t_S). Nonetheless, by virtue of the sharp velocity changes through the shocklets, it is expected that term C to play an inevitable role prior to the start of reconnection for the $M_o = 0.9$ case.

Figure 3.5 shows that compressibility leads to smoother changes of the extrema of the source term and its components during the time interval $[t_E, t_M]$. In Figure 3.5(a), at $M_o = 0.1$, sharp repulsion and large temporal variations of the extrema of the source terms are clear near t_E. On the other hand, smoother variations can be seen in Figure 3.5(e) at $M_o = 0.9$. Also, the overall extrema of terms A and B at $M_o = 0.1$ take place in the time interval of $t_E < t < t_M$, which is not always true for $M_o = 0.9$.

Using equations 2.23 and 2.24, we can further decompose terms A and B. Figure 3.6 shows the evolution of the extrema of the decomposed components of the source term, while terms C and E are excluded for clarity. Terms A2 and B2 do not play a considerable role. The flexion product, term A1 ($\rho \boldsymbol{v}.(\boldsymbol{\nabla} \times \boldsymbol{\omega})$), enstrophy, term A3, and the Laplacian of the kinetic energy, term B1, are dominant. The maximum of flexion product is always more than its absolute minimum value. Also, whereas the overall extrema of the dominant terms generally occur close to the end of reconnection, flexion product takes its overall minimum with a delay after t_M, when the bridges are recoiling from each other. As also revealed in Figure 3.5, sharp and smooth variations near t_E can be observed in Figures 3.6(a) and 3.6(e), at low and high M_o, respectively.

Let us examine each of these dominant decomposed components individually. The evolution of the bounds of terms A1, A3, B1, and D with respect to M_o is presented in Figure 3.7. Compressibility intensifies all of these terms. Except for the overall minimum of term A1 which occurs after t_M, the overall extrema take place close to t_E, generally for $t_E < t < t_M$–note that at $M_o = 0.7, 0.9$, the overall minimum of term B1 occurs just before t_E. The effect of M_o is more obvious on the evolution of term D extrema–the overall extrema occur before and after t_M at high and low M_o, respectively. As depicted in Figure 3.7, the contribution of the flexion product to the source term is mainly positive. Of course, the enstrophy term is always negative. The Laplacian of the kinetic energy and the

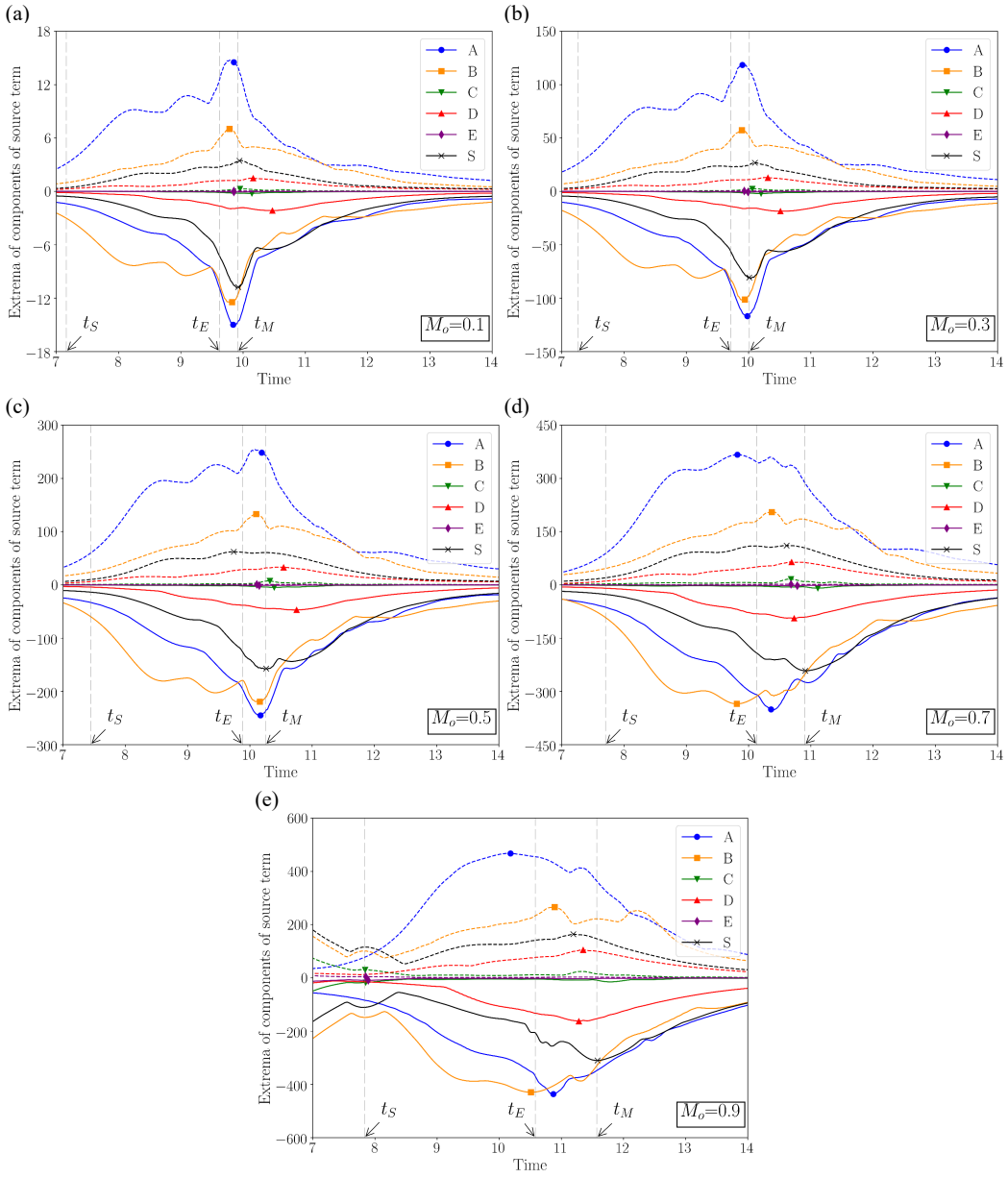

Figure 3.5: Evolution of the minimum (solid line) and maximum (dashed line) of the components of the source term at (a) $M_o = 0.1$, (b) $M_o = 0.3$, (c) $M_o = 0.5$, (d) $M_o = 0.7$, and (e) $M_o = 0.9$. Markers represent the overall extrema.

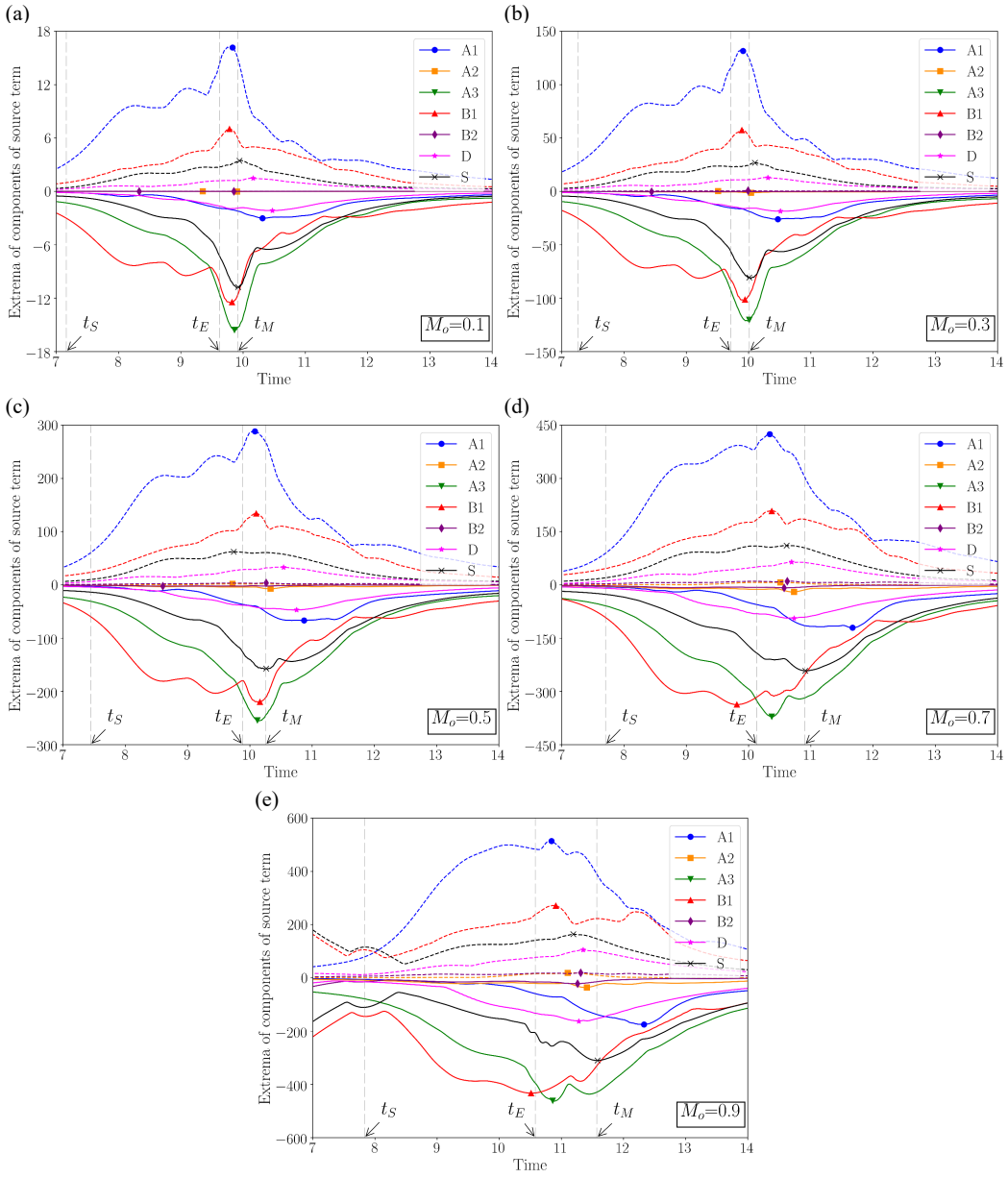

Figure 3.6: Evolution of the minimum (solid line) and maximum (dashed line) of the decomposed components of the source term at (a) $M_o = 0.1$, (b) $M_o = 0.3$, (c) $M_o = 0.5$, (d) $M_o = 0.7$, and (e) $M_o = 0.9$. Markers represent the overall extrema.

deviation from the isentropic condition have both positive and negative effects (discussed later).

Similar to the source term (Figure 3.4), the overall extrema and maximum amplitude of the dominant terms are linearly scaled by M_o as depicted in Figure 3.8(a)-(c). On the other hand, term D containing the Laplacian of pressure and density follows a quadratic scaling relation; see Figure 3.8(d). Such second-order dependency of term D on compressibility implies significant deviation from the isentropic condition at higher M_o. As vortex reconnection gives rise to important thermodynamic changes, it is expected that we observe a departure from the isentropic condition, especially at higher M_o.

Correspondingly, the aeroacoustic analogies, which generally neglect this term at low Mach number, appear to incorrectly estimate the acoustic source term (discussed later). Relatively little is known about the role of the deviation from the isentropic condition in sound production. At the end of our order-of-magnitude analysis, by comparing the magnitude of the overall extrema and maximum amplitude shown in Figures 3.7 and 3.8, we can conclude that the Laplacian of the kinetic energy, flexion product, enstrophy, and the deviation from the isentropic condition are respectively, in decreasing magnitude, the dominant components of the source term during reconnection. Note that such an analysis only highlights the pointwise significance of these terms; of course, a high value of a term at a single point in the domain does not necessarily imply the integrated importance of that term.

3.3 Flexion Product

As mentioned above, the flexion product, represented by term A1, is one of the dominant sources of aeroacoustic noise associated with the hydrodynamics of reconnection. Figure 2.2(a) shows that in a prototypical vortex tube, the flexion, $\boldsymbol{\nabla} \times \boldsymbol{\omega}$, and local velocity are co-aligned in the azimuthal direction. As a result, at a given radial distance from the axis of a vortex tube, the flexion product, $\boldsymbol{v}.(\boldsymbol{\nabla} \times \boldsymbol{\omega})$, is constant and always has a positive value. Alternatively, if the vortex tube is twisted (as in a polarized vortex, i.e. a vortex with axial flow), as shown in Figure 2.2(b), and has an self-induced core or advective velocity along the tube, the flexion and local velocity vectors will be aligned with the twisted vortex tube, thus yielding a large flexion product. These two scenarios, shown in Figure 2.2((a) and (b)), are means of flexion product generation in prototypical vortices. Following Hamman *et al* [31], we also speculate that the largest flexion product will result in coiling (negative flexion product) or uncoiling (positive flexion product) of the twisted vortex tube. Results in Figure 3.7(a) show that the overall maximum and minimum of

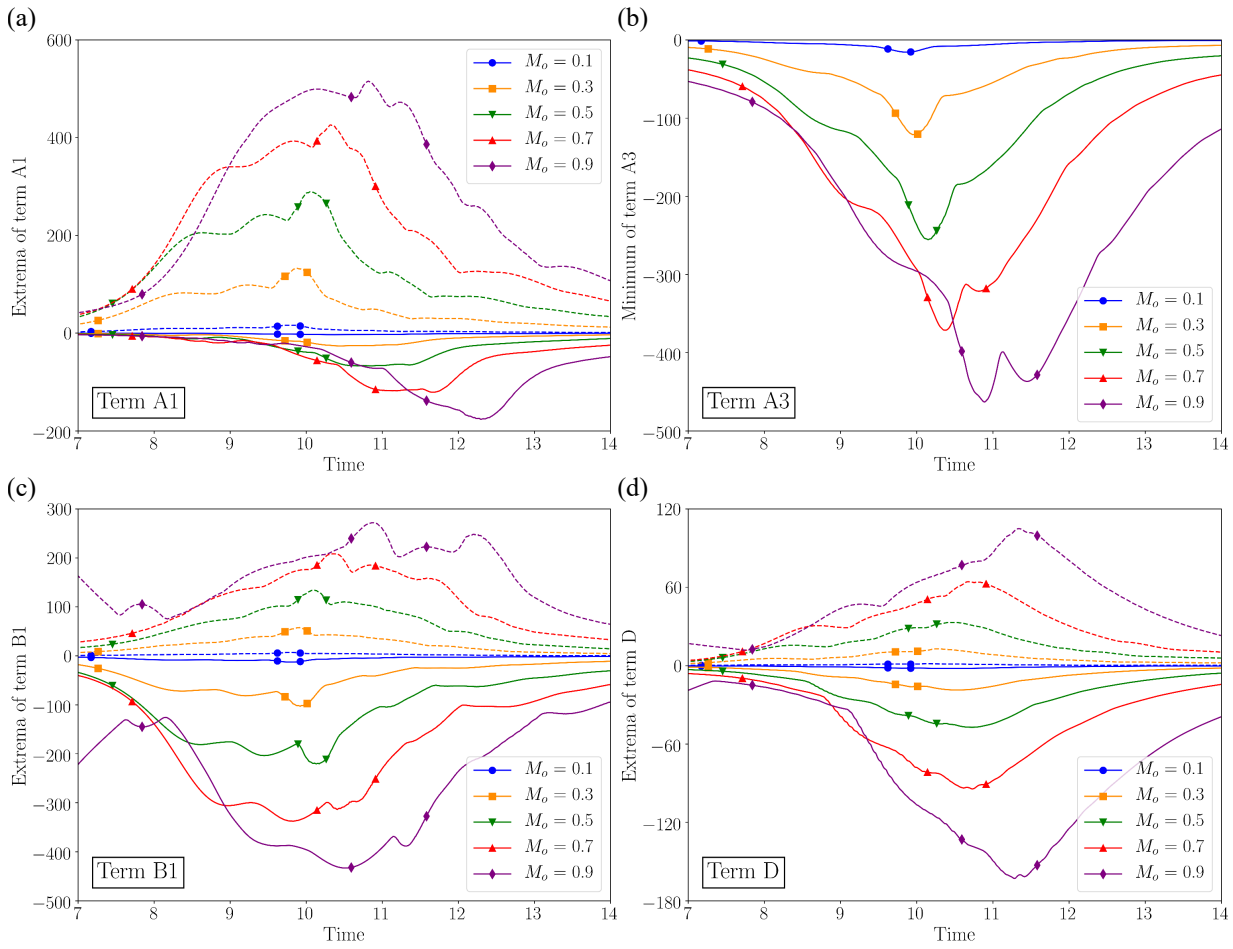

Figure 3.7: Evolution of the minimum (solid line) and maximum (dashed line) of (a) term A1, (b) term A3, (c) term B1, and (d) term D. Markers represent t_S, t_E, and t_M.

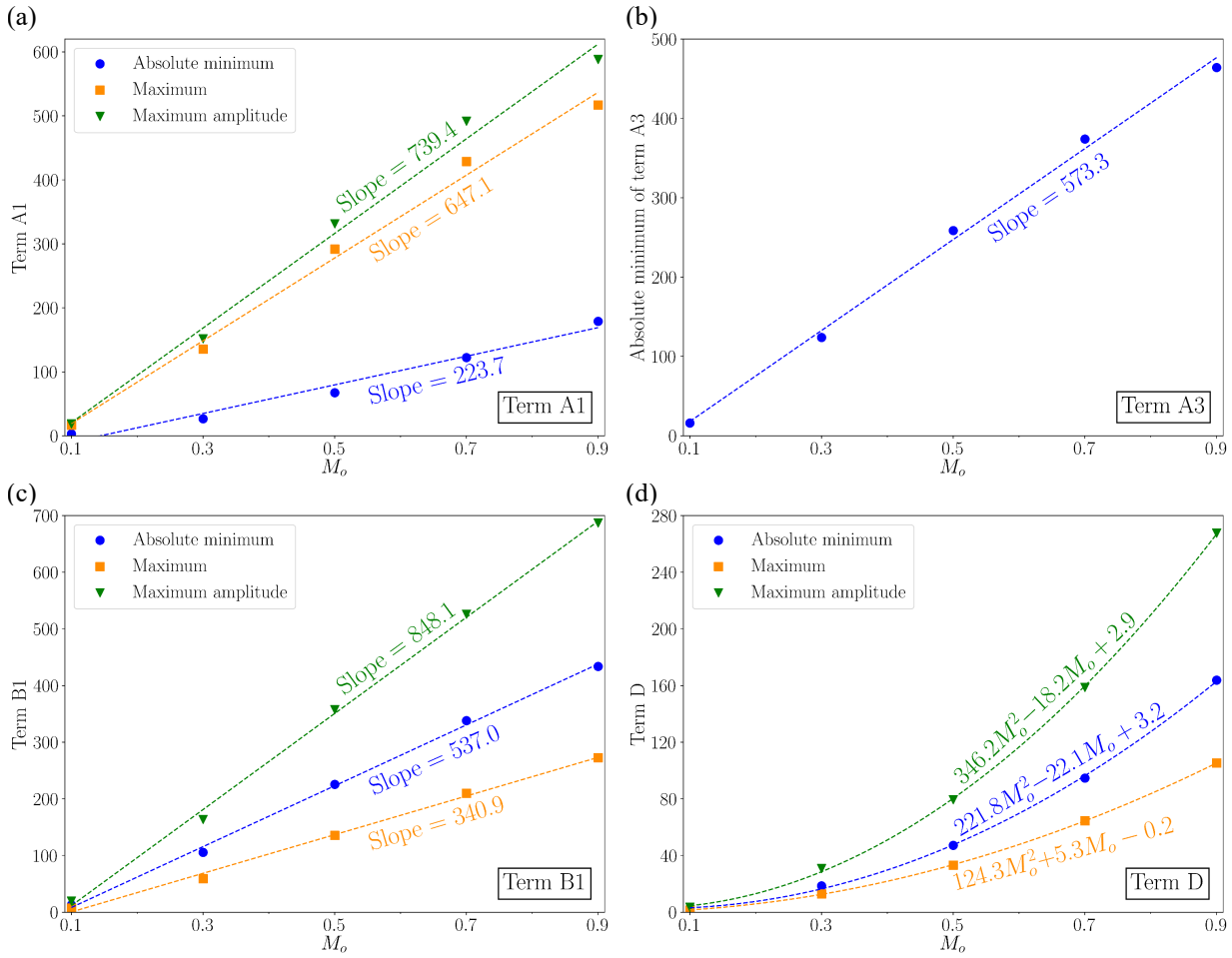

Figure 3.8: Scaling of the overall extrema and maximum amplitude of (a) term A1, (b) term A3, (c) term B1, and (d) term D.

the flexion product occur after t_E and physically correspond to an axial advection of a twisted vortex tube. The uncoiling motion is intensified near t_E by the repulsion of the highly-curved vortex lines at the top of the bridges. The maximum coiling (or the flexion product overall minimum) occurs at the region where twisted filaments wrap around the bridges. The coiling mechanism is visualized at $M_o = 0.5$ in Figure 3.9; the location of the overall minimum flexion product is shown in panel (a) and the orientations of the velocity, vorticity and flexion vectors about this point are shown in panels (b) and (c). In Figure 3.9(b), the velocity and flexion vectors form a very large obtuse angle thus yielding the maximum negative value of the flexion product. The orientation of the flexion vector at this location is the result of the twisting of the vortex lines bundle about the vortex tube axis, whereas the velocity vector (which is dominated by the repulsion of the bridges) is nearly aligned with the flexion vector, albeit in the opposite direction. Interestingly, as illustrated in Figure 2.2(a) (also shown in the right most portion of Figure 3.9(c)), when the bundle of vortex lines is not twisted, the flexion line wraps around the vortex tube. With the twisting of the vortex tube (hence increasing the flexion product), the flexion lines are aligned in the direction of the vortex tube axis, as seen in Figure 2.2(b) (also shown at the middle of Figure 3.9(c)). Furthermore, core dynamics is inherent to coherent structures and vortex dynamics where nonuniform tube diameter along a vortex coils vortex lines which then propagate as waves along vortices. Such core dynamics, elucidated first and extensively studied by Melander and Hussain [71], presumably can be useful in explaining the phenomenon of vortex bursting (private communication E. Stout).

Therefore, coiling and uncoiling of vortex lines in a twisted vortex tube represent one of the most dominant sources of aeroacoustic noise in vortex reconnection, i.e. flexion product term. As discussed above, being a purely hydrodynamic source term, the flexion product presumably plays a decisive role in the incompressible vortex reconnection. Furthermore, this term scales linearly with M_o (Figure 3.8(a)); a detailed explanation of the role of compressibility on this term is outside the scope of the present work. To better understand the spatial distribution, we show the positive and negative isosurfaces of the flexion product along with the helicity density ($h = \boldsymbol{v}.\boldsymbol{\omega}$) in Figure 3.10; contours on the half of the bridge plane are also given. As in Figure 3.9, these isosurfaces are for $M_o = 0.5$ at the time when the flexion product reaches its overall minimum. The large region of positive flexion product is predominantly caused by the typical alignment of the induced velocity and flexion vectors in a prototypical (or twisted) vortex tube. The negative flexion product can only arise due to the coiling of twisted vortex tube; thus the negative isosurfaces of the flexion product are localized at specific points in and around the bridges (blue color in Figure 3.10(a)). The isosurface of helicity density (Figure 3.10(b)) provides insight on the local alignment of the velocity and vorticity vectors at this specific time instant. The

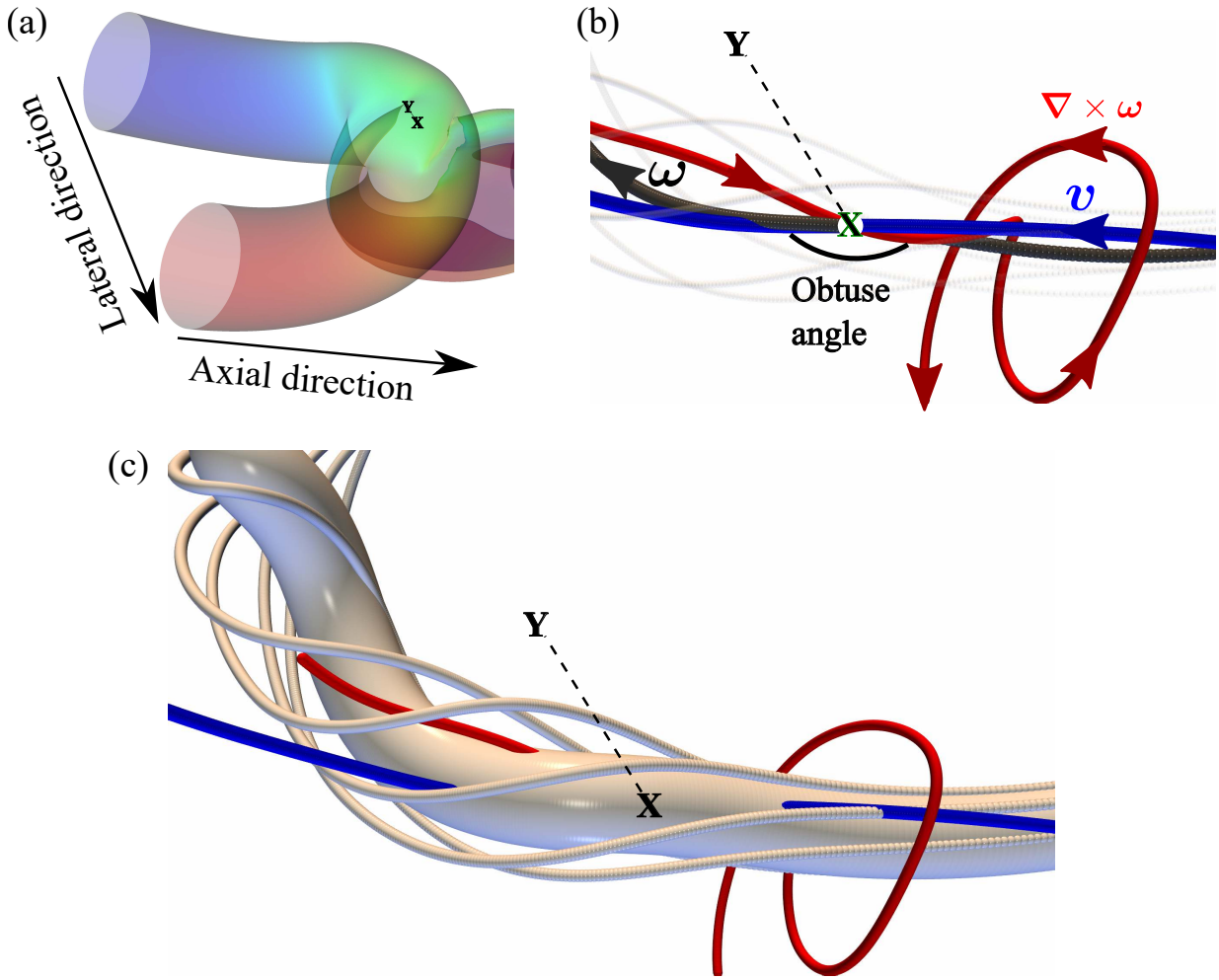

Figure 3.9: (a) Position of the overall minimum flexion product at $M_o = 0.5$. (b) Orientation of the velocity, vorticity, and flexion vectors. (c) Twist of vortex lines (small light colored lines) around the central vortex tube.

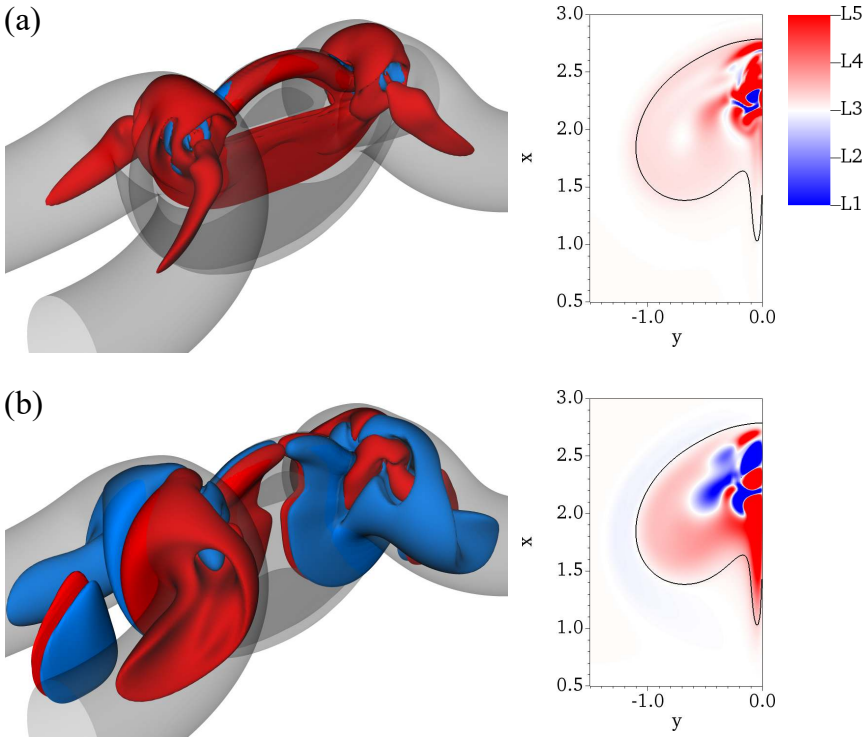

Figure 3.10: Positive and negative isosurface and contour (on the half of the bridge plane) of (a) flexion product and (b) helicity density for $M_o = 0.5$ at the time of the overall minimum of the flexion product. Limits of the global linear legend equal the negative and positive 5% of the overall maximum absolute value of each variable. The solid line depicts the enstrophy contour set at 2% of the overall maximum enstrophy.

evolution of the isosurface of the flexion product and the helicity density for $M_o = 0.5$ can be found in Figures B.1 and B.2, respectively.

3.4 Mutual Cancellation and Spatial Distribution

As depicted in Figures 3.5 and 3.6, the amplification of the source term during reconnection is not as intense as those of its dominant components–which implies spatial cancellations between the source term's constituents. For instance, positive and negative contributions of the Laplacian of the kinetic energy neutralize the negative and positive contributions of the enstrophy and flexion product, respectively. Such mutual cancellation mechanisms have

been observed in the sound generation in a mixing layer through vortex pairing [14, 10]. Extrema evolution of the term A+B (the sum of terms A and B), term D, and the source term is compared in Figure 3.11. The amplification of A+B is less than its components, highlighting the cancellation between A and B. Another interesting point in Figure 3.11 is the higher relative contribution of term D as M_o increases; compare Figure 3.11(a) and (e). This conclusion could also be drawn by observing the linear and quadratic scalings of the source term and term D, respectively in Figures 3.4 and 3.8(d).

Let us explore the spatial distribution of the source term. Considering the moderate Re of the cases, the spatial evolution of the source term is nearly symmetric. As a result, we only present the contours on the half of the characteristic planes in the following figures. Figure 3.12 shows the source term contour on the collision plane at six times and for different M_o. The spatial distribution of the source term and the vorticity field evolution, visualized by the enstrophy line contour, remain essentially the same during the reconnection with subsonic initial conditions, although we note an intensification of the localized source term at higher M_o. Our results on the symmetric and bridge planes (see Figures B.3 and B.4) also agree with this observation. Hereafter, we focus on the spatial distribution of the source term at $M_o = 0.5$, representing the general behavior of the subsonic reconnection process at a moderate subsonic M_o.

The spatial distributions of the dominant components and the source term are compared on the collision, symmetric, and bridge planes respectively in Figures 3.13, 3.14, and 3.15. Positive regions of term A, which are primarily due to the flexion product (term A2 is negligible) nearly overlap the negative regions of term B. The same situation exists for negative regions of term A, mainly originating from the enstrophy, and the positive regions of term B. The importance of A over B is manifested by the qualitative resemblance between A and A+B. These contours also exhibit the inevitable role of term D which could be considered as a reinforcement of term A+B especially in the cores of the bridges and threads.

The flexion product, $\rho\boldsymbol{v}.(\boldsymbol{\nabla}\times\boldsymbol{\omega})$, is remarkably positive on the collision plane which implies high magnitudes of the velocity and flexion, $\boldsymbol{\nabla}\times\boldsymbol{\omega}$, vectors and the acute angle between them. High velocity plane jet on the collision plane is rooted in the induced velocity between the anti-parallel vortices. The high flexion magnitude on the collision plane originates from the rotation of the vorticity vector from the axial towards the lateral direction during reconnection. Indeed, the positive contribution of the flexion product is due to the acute angle between the velocity and flexion vectors; see Section 2.1.3 for more discussion. Further studies are required to characterize the evolution of these vectors in canonical vortical flows. Except at the vortex cores where the enstrophy is dominant, term A shows a positive contribution at other regions; see Figures 3.13, 3.14, and 3.15.

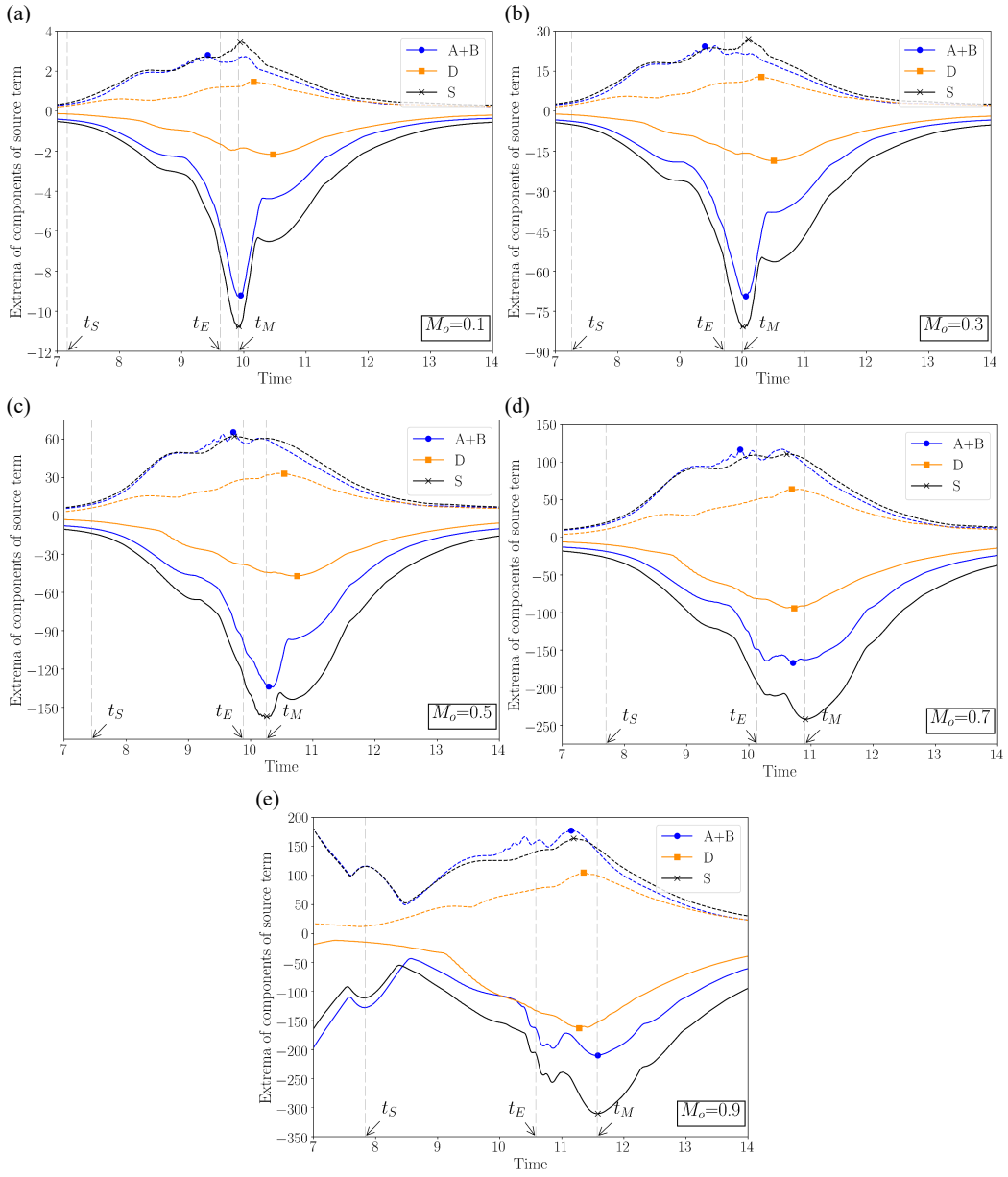

Figure 3.11: Evolution of the minimum (solid line) and maximum (dashed line) of term A+B, term D, and the source term at (a) $M_o = 0.1$, (b) $M_o = 0.3$, (c) $M_o = 0.5$, (d) $M_o = 0.7$, and (e) $M_o = 0.9$. Markers represent the overall extrema.

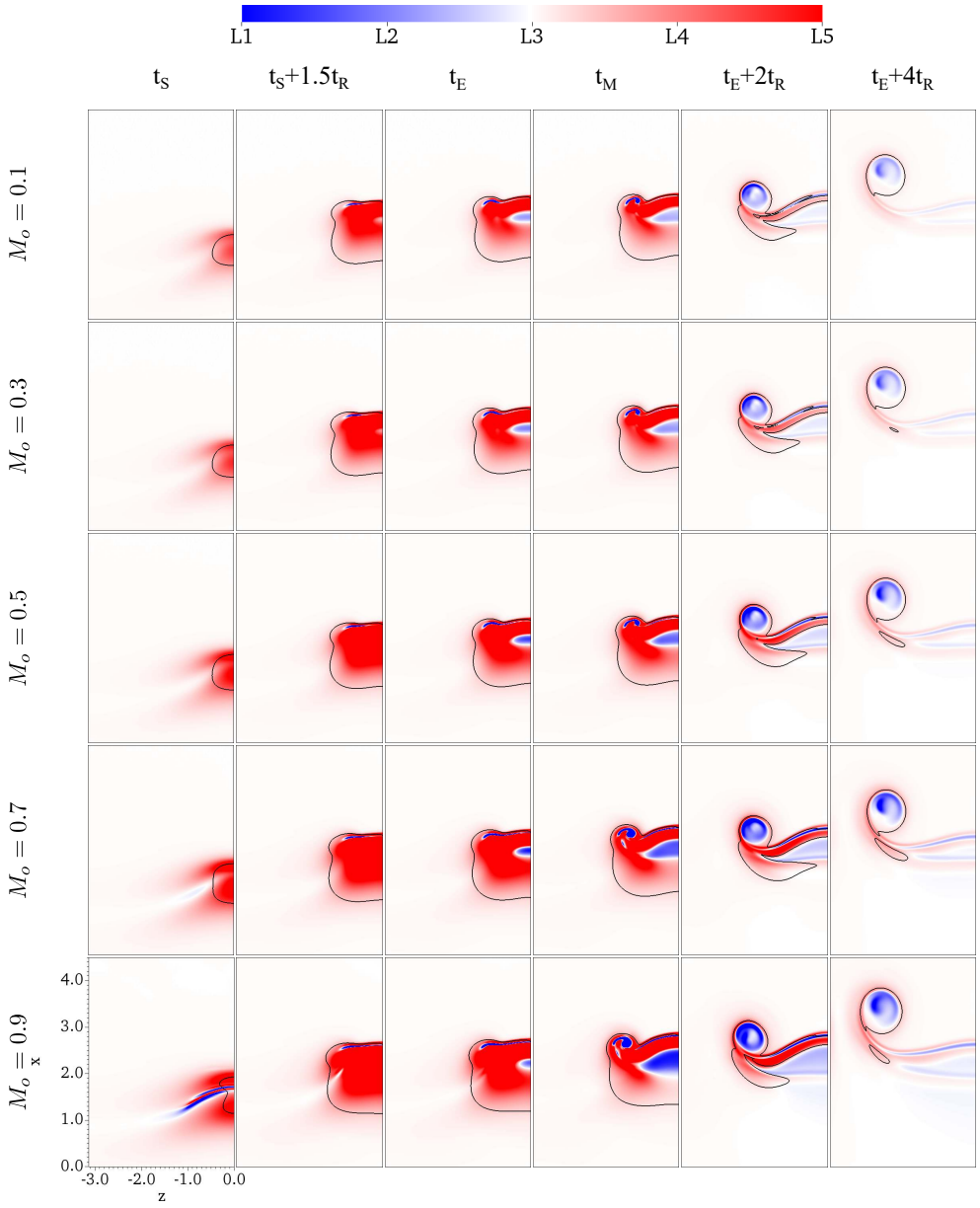

Figure 3.12: Source term contour on the collision plane. Limits of the global linear legend equal the negative and positive 5% of the overall maximum absolute value of the source term. The solid line depicts the enstrophy contour set at 2% of the overall maximum enstrophy.

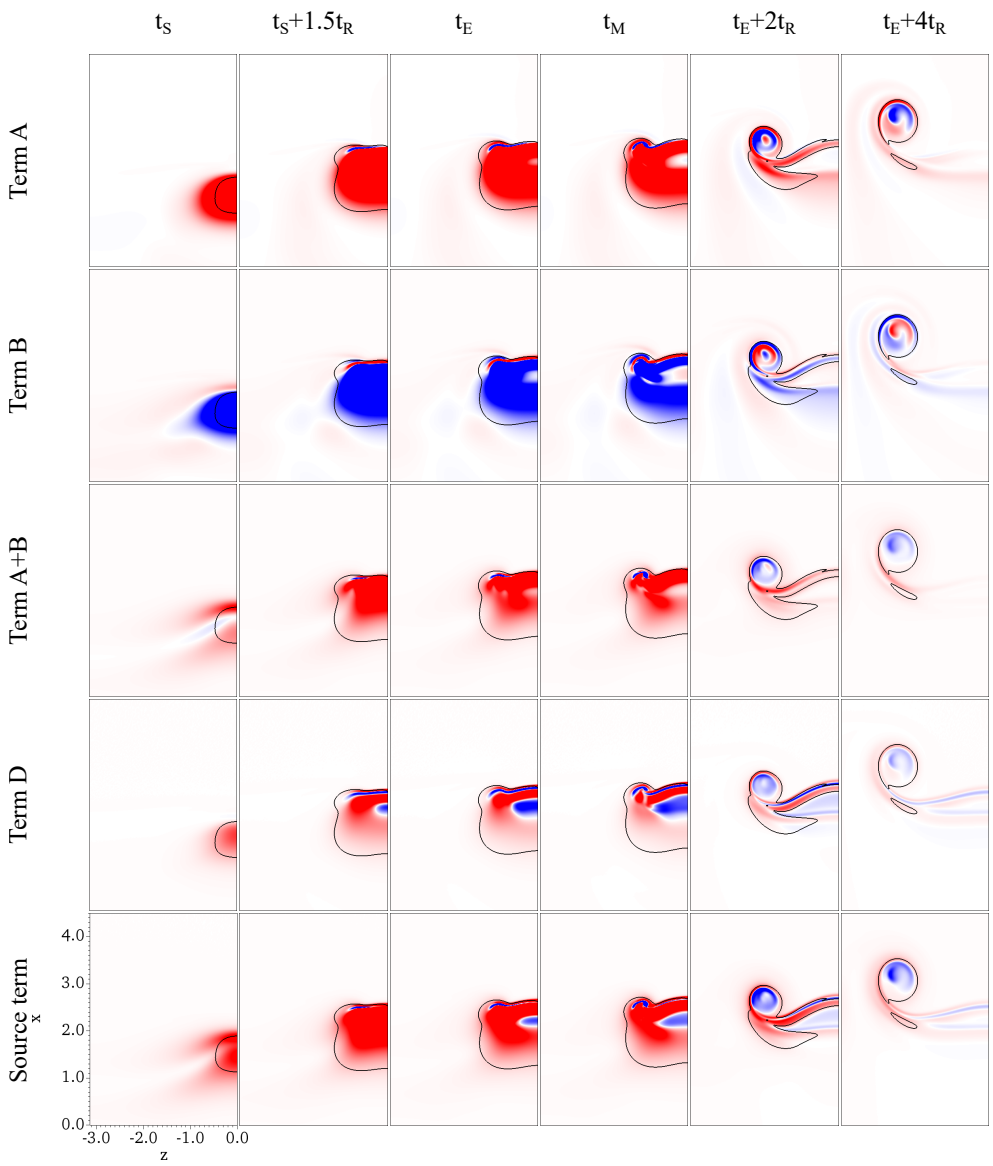

Figure 3.13: Source term and its dominant components contour on the collision plane at $M_o = 0.5$. The legend is the same as in Figure 3.12.

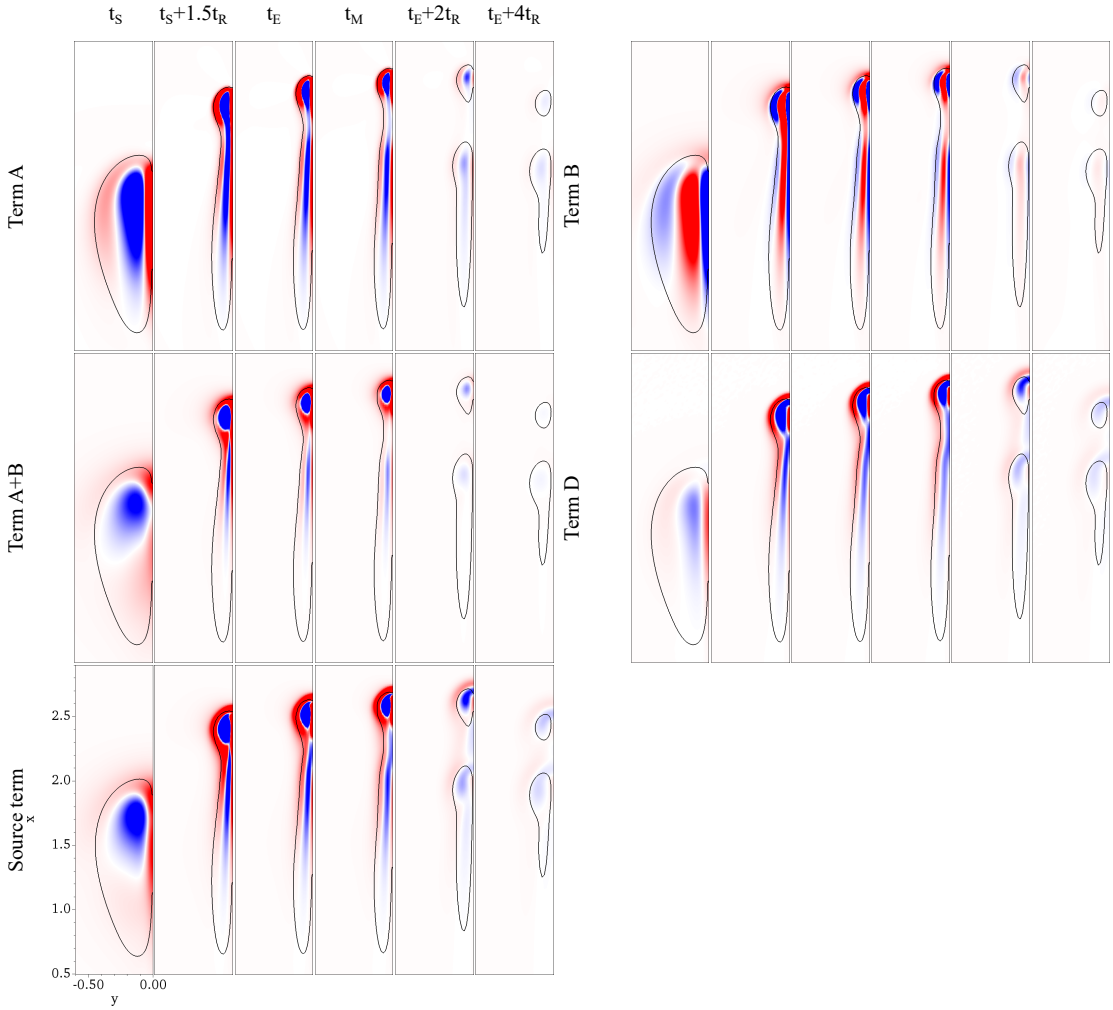

Figure 3.14: Source term and its dominant components contour on the symmetric plane at $M_o = 0.5$. The legend is the same as in Figure 3.12.

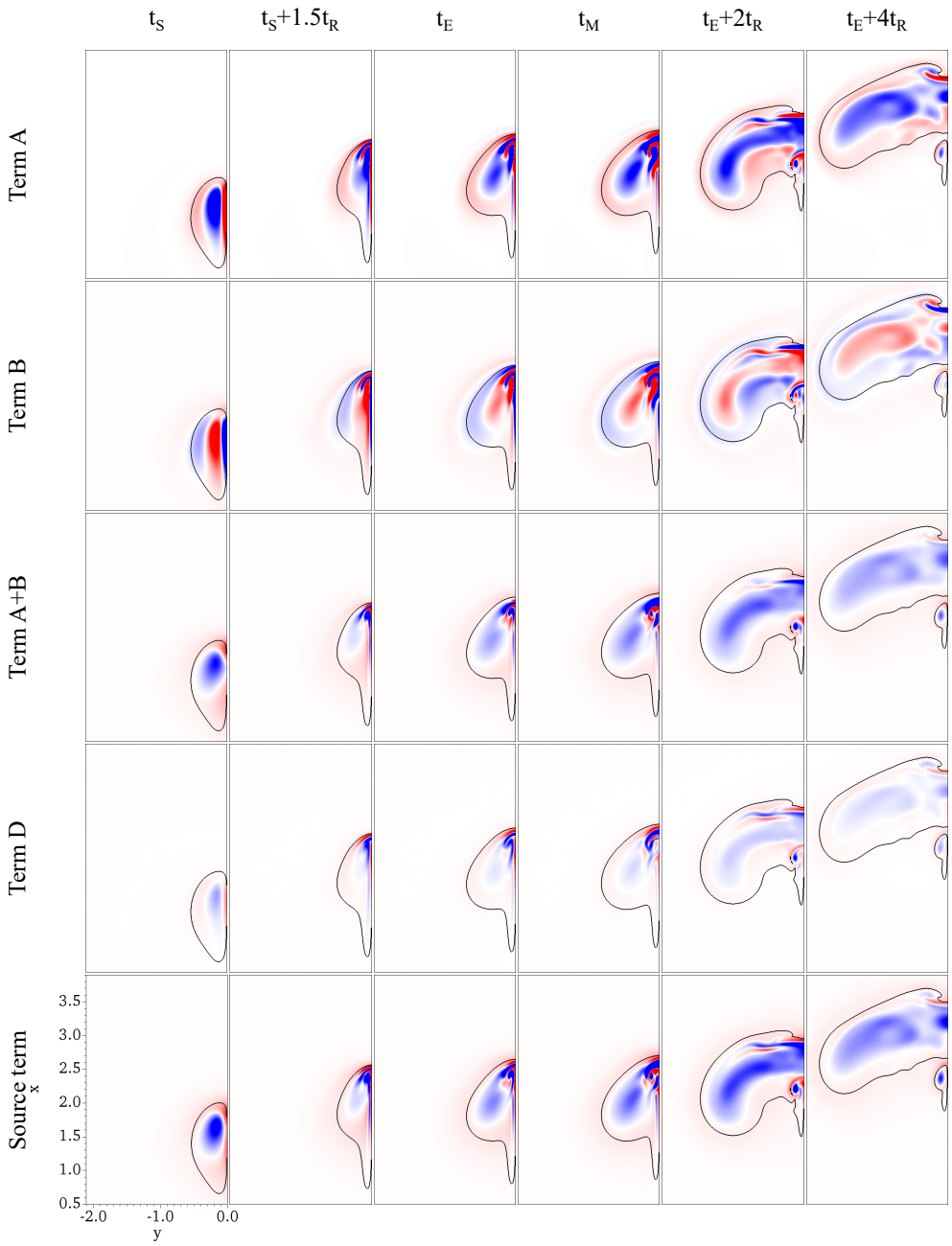

Figure 3.15: Source term and its dominant components contour on the bridge plane at $M_o = 0.5$. The legend is the same as in Figure 3.12.

Considering the high velocity of the jet flow, the Laplacian of the kinetic energy, which is the dominant contributor to term B, becomes highly negative on the collision plane; see Figure 3.13. The same explanation can be used around the vortex cores–because there is high velocity around the core of vortex. On the other hand, the low velocity gradient at the vortex axis leads to positive values of term B; see Figures 3.13, 3.14, and 3.15. Thus, terms A and B are intense but mutually cancelling.

The deviation from the isentropic condition denotes a difference between the Laplacian of pressure and density while the latter one has been multiplied by c_0^2; see equation 2.26. Where the pressure and density evolve isentropically, this term is exactly zero. Considering the equation of state and small temperature variations, the evolutions of pressure and density are similar. Low pressure and density in the vortex cores yield positive Laplacian in terms D1, $\nabla^2 P$, and D2, $-c_0^2 \nabla^2 \rho$. The results show that term D2 is dominant. Term D, identical to term A+B, becomes negative in the vortex cores, i.e. cores of bridges and threads; see Figures 3.13, 3.14, and 3.15. Note that the contribution of term D is more evident at the attachment of symmetric head-tail structures on the center line, clearly shown by blue areas at the middle of the contours on the collision plane in Figure 3.13. Despite similarities in the evolution as depicted in Figure 3.16, the absolute minimum value of D2 is more than the maximum of D1, justifying the negative contribution of D in the vortex cores. Also, the relative effect of D2 including the Laplacian of density increases with M_o; compare range of different terms in Figures 3.16(a) and (e).

The evolution of the isosurface of the positive and negative source terms is presented in Figure 3.17. At the start of reconnection, the negative source term is mainly located in the vortex cores, while the positive part, due to the flexion product, extends on the collision plane and bends over the vortices. Halfway through the reconnection event, due to the deviation from the isentropic condition and the enstrophy term at the stretched tail (stretched tail of the well-known head-tail structure is appeared as vortex sheet), the negative source term extends on both sides of the collision plane; compare Figures 3.14 and 3.17(b) at $t_S + 1.5t_R$.

Because of the sign changing characteristic of the Laplacian of pressure and density, a succession of negative and positive regions of term D is expected. Constructed by the flexion product and the deviation from the isentropic condition, the positive isosurface of the source term emerges as parallel layers around the vortex sheets. Note that despite identical sheet-like structures, the red isosurfaces parallel to the collision plane do not represent regions of concentrated vorticity. Resorting to the same analysis, the development of the positive isosurface around the bridges and heads of the threads can be explained.

As time advances, vortex sheets extend in the axial and advection directions, so do

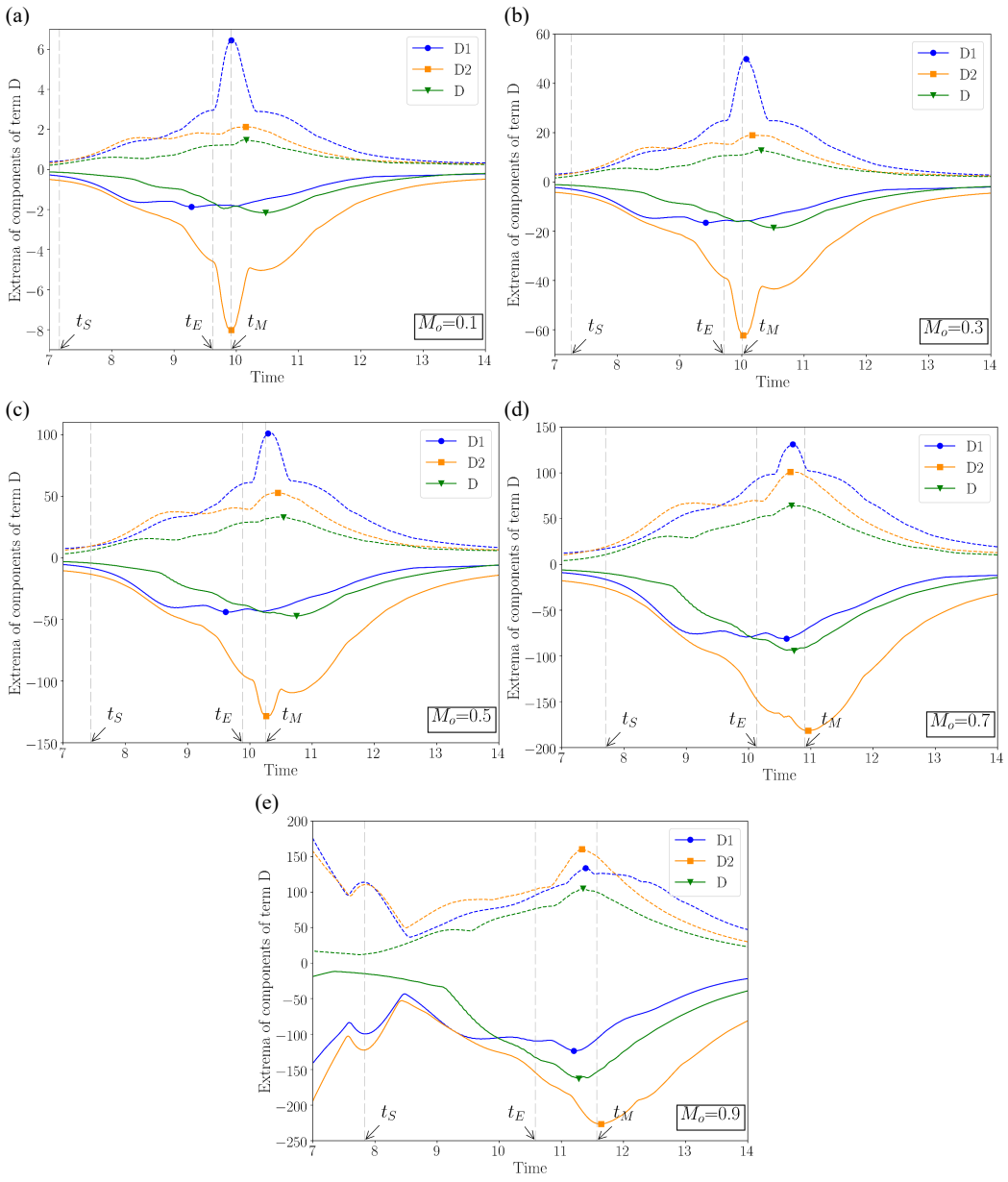

Figure 3.16: Evolution of the minimum (solid line) and maximum (dashed line) of terms D1, D2, and D at (a) $M_o = 0.1$, (b) $M_o = 0.3$, (c) $M_o = 0.5$, (d) $M_o = 0.7$, and (e) $M_o = 0.9$. Markers represent the overall extrema.

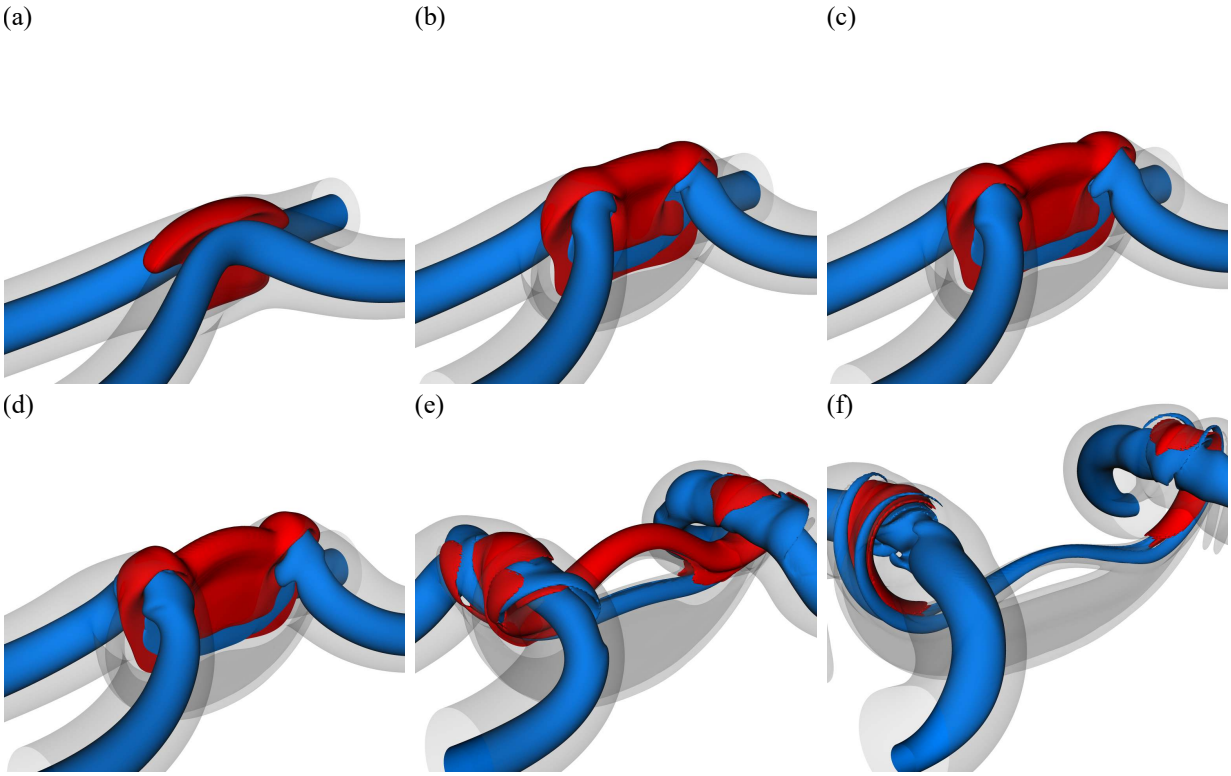

Figure 3.17: Source term isosurface of $M_o = 0.5$ at (a) t_S, (b) $t_S + 1.5t_R$, (c) t_E, (d) t_M, (e) $t_E + 2t_R$, and (f) $t_E + 4t_R$. Blue and red isosurface levels equal the negative and positive 1% of the overall maximum absolute value of the source term. Gray transparent color shows the enstrophy isosurface set at 2% of the overall maximum enstrophy.

positive layers of the source term; see Figures 3.17(c) and (d). Once reconnection is complete and the bridges recoil from each other, entangled positive and negative source term isosurfaces are accumulated at bridges and threads while the cores of the vortices have negative contributions; see Figures 3.17(d) and (e). Due to the global isosurface level used in Figure 3.17, red positive layers may not be visualized enveloping the blue isosurfaces in vortex cores of the separated tails; however, a weak positive source term is still around the cores as demonstrated in the last two panels of the Figure 3.14. As stated earlier, the main positive source term is rooted in the flexion product and the angle between the velocity and the flexion vectors is critical in the sign of the contribution. The flexion vector evolution and its relation to the velocity vector in canonical vortical flows have not been studied yet.

3.5 Approximate Sound Source

Since it is not clear yet what percentage of the near-field pressure perturbation propagates to far field, the dominance of the decomposed source terms on the RHS of the wave equation 2.22 in far-field sound generation could be completely different from their hydrodynamic importance in the near field. Also, considering the above cancellation mechanism, estimation of the structure of the true sound source at near field becomes even more complicated. For this purpose, one may solve the wave equation for each of the decomposed source terms in equation 2.22, which requires 3D time-resolved data and is computationally expensive. Another approach is using aeroacoustic analogies to study the approximate sound sources at near field.

In this section, the Powell's aeroacoustic analogy [83] is used to visualize the spatial distribution of the approximate sound sources. As stated in Section 2.1.3, in Powell's low-M analogy (without external force field and neglecting viscous-thermal effects), only term A ($\boldsymbol{\nabla}.[\rho(\boldsymbol{\omega} \times \boldsymbol{v})]$) is kept and all other source terms in equation 2.22 are eliminated. Note that term A contains the flexion product (see equation 2.23) and it is expected that the Powell's analogy provides a good approximation of the reconnection sound sources.

Approximate sound sources at $M_o = 0.5$ are visualized in Figure 3.18 using isosurface of the magnitude of the second time derivative of the Lamb vector, $|\partial^2(\boldsymbol{\omega} \times \boldsymbol{v})/\partial t^2|$ [104, 105, 18]. At t_S (Figure 3.18(a)), sound sources are located at the contact region of the two vortices and include cusps of the recently reconnected vortex lines. At $t_S + t_R$ (Figure 3.18(b)), when 50% of the initial circulation is transferred to the collision plane, sound sources are mainly located at the reconnection zone including two not-fully-developed bridges, where the reconnected vortex lines with cusps rapidly recoil by self-induction and accumulate. Reconnection is still in progress at this time as anti-parallel vortex lines

continue to approach each other and reconnect. Thus, the reconnection zone between the bridges has a considerable share in sound sources at this time. At t_E (Figure 3.18(c)), once 95% of the circulation is transferred, reconnection is virtually completed and sudden repulsion and accumulation of reconnected vortex lines cause the bridges to act as moving sound sources. Threads, which represent small-scale remnants of the initial vortices, survive the reconnection and experience a high level of stretching as they advect and accelerate by mutual induction. As Re increases, the curvature and concomitant self-induction of the reconnected cusps increase and the two vortices recoil from each other more intensely [40]. This process leads to higher stretching of the threads and hence a rapid increase in vorticity of the threads; as a result, the threads' contribution to the sound sources should increase at higher Reynolds numbers [74, 20]. Other than an increased contribution from the threads, we expect the same qualitative time evolution of sound sources at higher Reynolds numbers.

Figure 3.19 shows the contour of enstrophy and sound sources of $M_o = 0.5$ on the collision plane at different times. Because of the symmetric evolution, only half of the collision plane is shown. As discussed earlier and shown in Figures 3.19(a) and 3.19(b), considerable sound is radiated from the reconnection region between the not-fully-developed bridges at the middle stages of the reconnection, i.e. between $t_S + t_R$ and $t_S + 1.5t_R$. The other interesting point is that at t_E (Figure 3.19(c)), the most sound originates from the contact region (also location of intense vortex stretching) between the bridges and threads, where the reconnected vortex lines accumulate and create concentrated vorticity regions–the cores of the bridges.

3.6 Shocklets Features

As seen earlier, despite a subsonic reference Mach number, $M_o = 0.9$, reconnection would affect shocklet formation. Note that shock generation in initially supersonic reconnection could highly modify the circulation transfer process [106]; therefore, shocklet formation, with initially subsonic $M_o = 0.9$ at high Re, could play a key role in both hydrodynamics and aeroacoustics of reconnection. Near shocklets, magnification of the gradient of density, the dilatation, and their interactions, which appeared in source term C in equation 2.25, are expected. The evolution of the maximum magnitude of the density gradient and the extrema of the dilatation at different M_o are compared in Figure 3.20, where intensification after t_S at all M_o is clear; however, three larger oscillations before t_S at $M_o = 0.9$ take place due to the shocklet formation. Note that, by comparing the variations of density, velocity, and pressure through shocklets with normal shock relations, shocklet formation

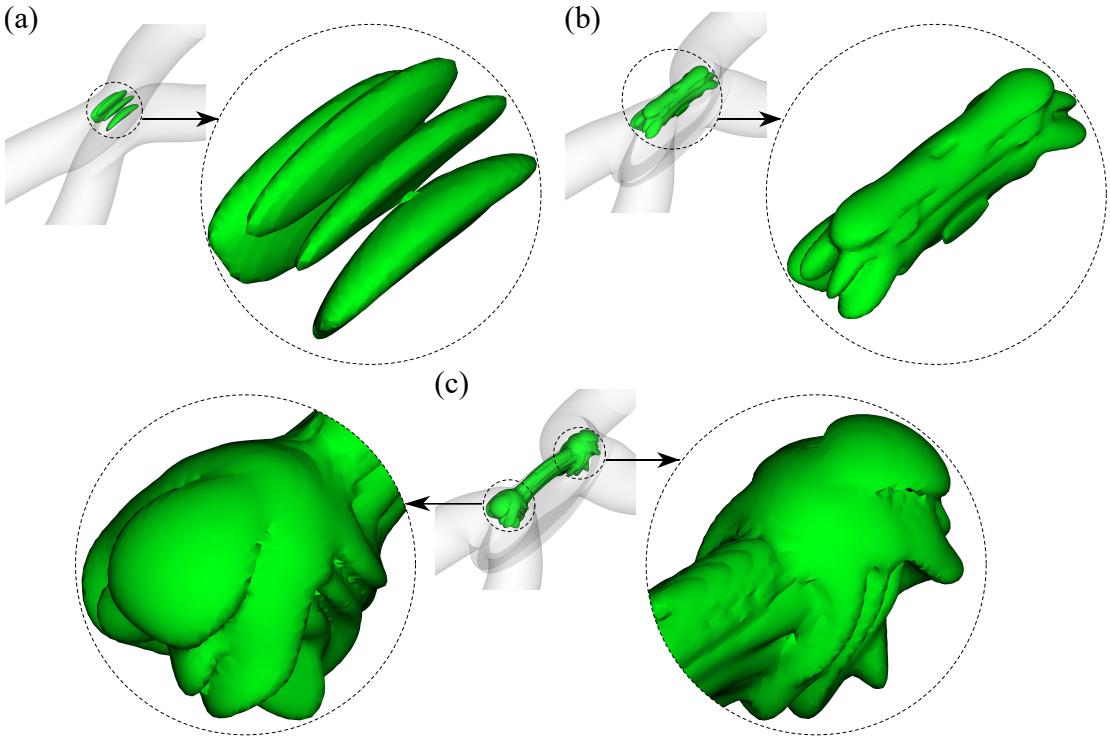

Figure 3.18: Sound source isosurfaces (and their magnified views, indicated by arrows) of $M_o = 0.5$ at: (a) t_S, (b) $t_S + t_R$, and (c) t_E. Transparent grey color is the enstrophy isosurface at 10% of the maximum initial axial vorticity and green is the isosurface of the magnitude of the second time derivative of the Lamb vector at 3% of its maximum value at t_E.

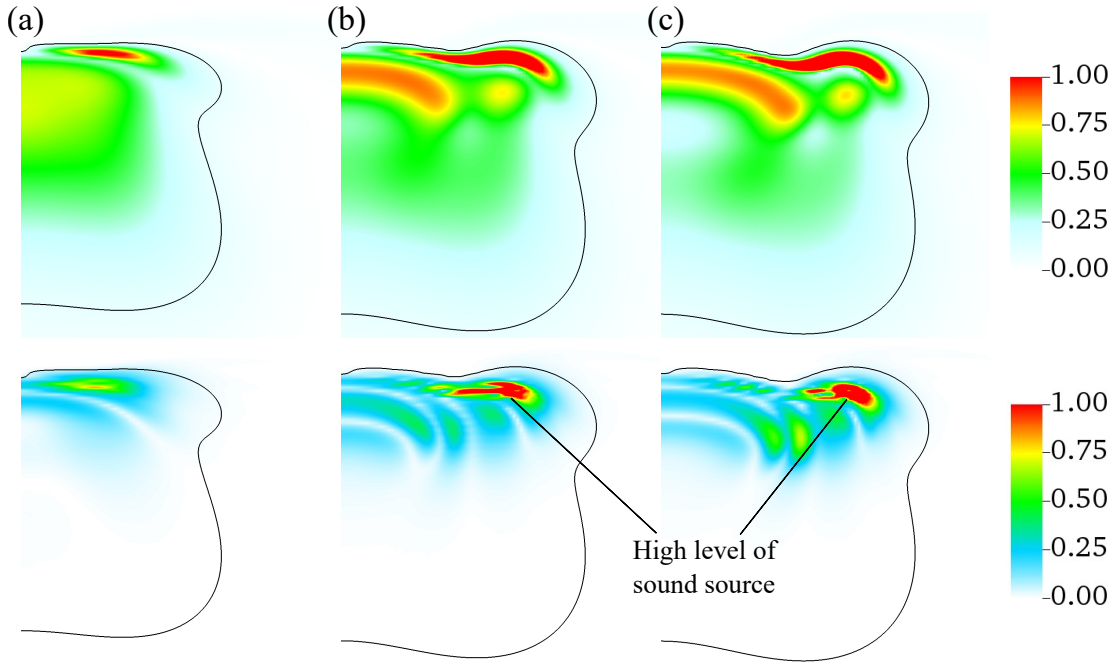

Figure 3.19: Contours of enstrophy (top row) and sound sources (second row) of $M_o = 0.5$ on the collision plane at (a) $t_S + t_R$, (b) $t_S + 1.5t_R$, and (c) t_E. Both enstrophy and sound sources are divided by the maximum initial axial vorticity. Black line shows enstrophy contour at 10% of the maximum initial axial vorticity.

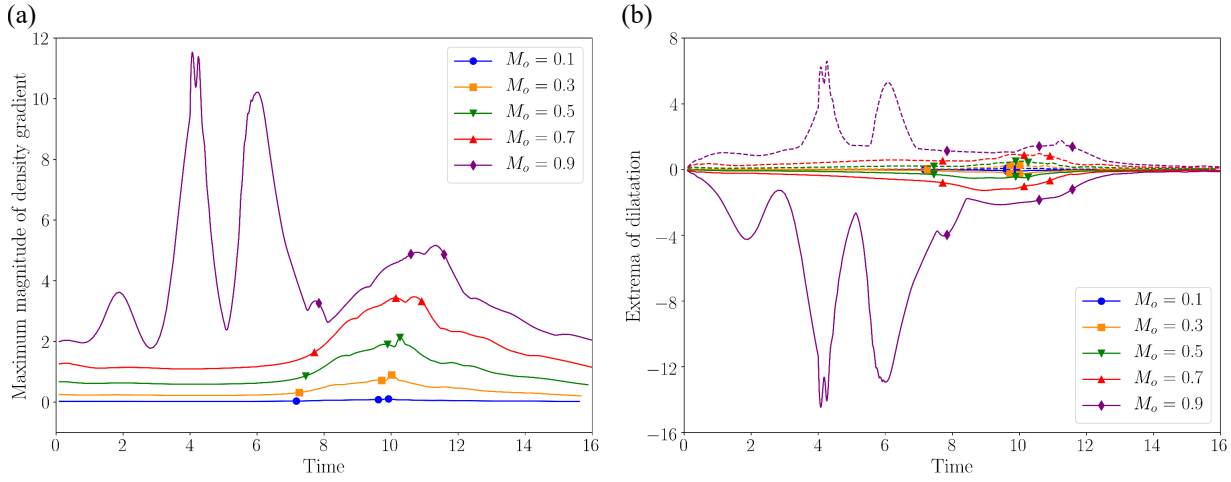

Figure 3.20: Evolution of the (a) maximum magnitude of the density gradient and (b) extrema of the dilatation. Markers represent t_S, t_E, and t_M.

can be validated (calculations are not shown in this thesis).

In this section, the main focus is on $M_o = 0.9$ before t_S when appearance of shocklets lead to oscillations of the source term; see Figure 3.3. As seen in Figure 3.20, density gradient and dilatation are highly sensitive to shocklet formation. Thus, contribution of term C to the source term (see equation 2.25) is inevitable through shocklets. Also, due to the high velocity variations, contribution of the Laplacian of the kinetic energy should be significant near shocklets–note that the Laplacian can be interpreted as a measure estimating deviation from the neighbors average. Evolution of the extrema of the components of the source term before t_S at $M_o = 0.9$ is shown in Figure 3.21; terms B and C are the main contributors to the source term through shocklets.

Evolution of the constituents of terms B and C before t_S at $M_o = 0.9$ are compared in Figure 3.22. Terms B1, $\rho\nabla^2\left(\frac{|\boldsymbol{v}|^2}{2}\right)$, C1, $\rho\boldsymbol{v}.\boldsymbol{\nabla}(\boldsymbol{\nabla}.\boldsymbol{v})$, and C4, $\boldsymbol{v}.(\boldsymbol{v}.\boldsymbol{\nabla}\boldsymbol{\nabla}\rho)$, are the dominant ones; however, other remaining terms also experience intensification through shocklets. Term C2, $\rho(\boldsymbol{\nabla}.\boldsymbol{v})^2$, is always positive; terms B2, $\boldsymbol{\nabla}\rho.\boldsymbol{\nabla}\frac{|\boldsymbol{v}|^2}{2}$, C3, $2(\boldsymbol{\nabla}.\boldsymbol{v})\boldsymbol{v}.\boldsymbol{\nabla}\rho$, and C5, $\boldsymbol{v}.(\boldsymbol{\nabla}\rho.\boldsymbol{\nabla}\boldsymbol{v})$, are mainly negative near shocklets.

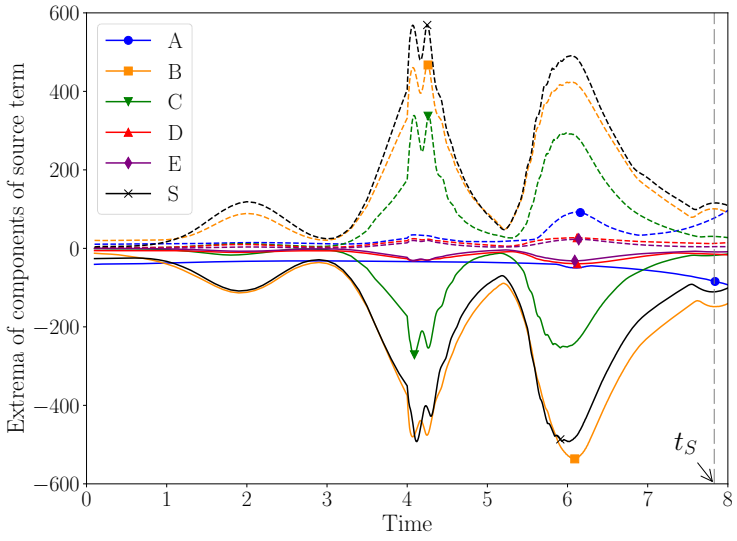

Figure 3.21: Evolution of the minimum (solid line) and maximum (dashed line) of the components of the source term before t_S at $M_o = 0.9$. Markers represent the extrema over the time period of $[0, t_S]$.

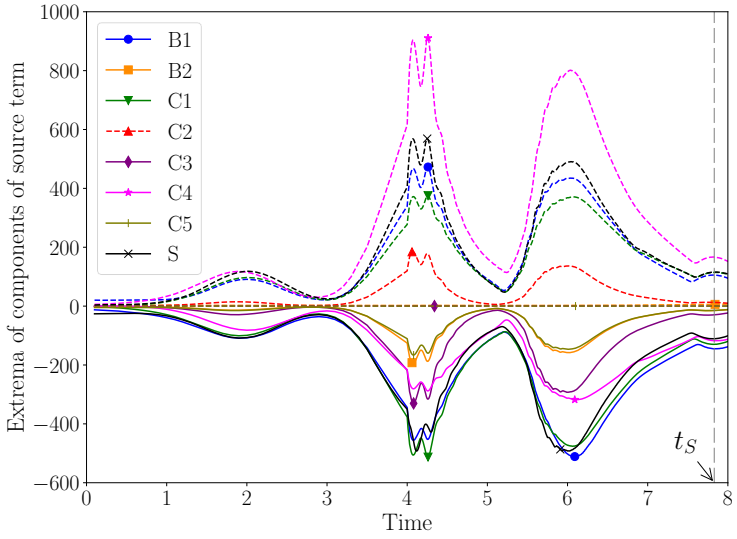

Figure 3.22: Evolution of the minimum (solid line) and maximum (dashed line) of the decomposed components of the source term before t_S at $M_o = 0.9$. Markers represent the extrema over the time period of $[0, t_S]$.

Chapter 4

Near-Field Pressure and Far-Field Sound

In this chapter near-field pressure evolution and far-field sound during reconnection are explored. First, near-field pressure contour at different characteristic times for different M_o are compared. Then, the sharp rise of the near-field pressure during reconnection is investigated. Finally, instantaneous and time-averaged sound directivity patterns for different M_o within scaling relations are provided.

4.1 Near-Field Pressure Evolution

Consistent with the statements of Cabana *et al* [10], a non-zero source term–which is the essence of the sound production–is the result of subtle imbalances perturbing inherent spatiotemporal symmetry among components of the source term. However, the conversion mechanism of near-field energy into acoustic energy is not clear yet. It has been often acknowledged that the near-field pressure evolution could be critical in discerning the causality between the hydrodynamic effects and acoustic far-field pressure [13, 67]. The pressure contour on the collision plane for different M_o is presented in Figure 4.1. High pressure below the vortices can be observed at t_S. As time advances, vortex lines reconnect alongside the axial direction leading to the vorticity generation in the lateral direction; see the extended low pressure region at $t_S + 1.5t_R$ and t_E showing the concentrated vorticity region in the lateral direction. Accumulation of the reconnected vortex lines in the bridges constructs the cores of reconnected vortex tubes manifested by dark blue color at t_M. Note

that, in addition to the twisted vortex line bundles [106], high pressure at the reconnection region could also affect the axial flow along the vortex core. Once the bridges are complete, the intensity of low core pressure decreases; see fading blue color at $t_E + 2t_R$ and $t_E + 4t_R$.

Although the qualitative evolution is the same, spatial distribution of near-field low pressure is clearer at higher M_o; compare distribution of orange color at low and high M_o in Figure 4.1. More specifically, the rise of the near-field low pressure at t_E [18], delimited by a dashed line, becomes more intense as M_o increases; follow the dashed line evolution at $M_o = 0.9$. Figure 4.2 shows the pressure contour on the symmetric plane. Although the low pressure spatial distribution and sharp rise are obvious at higher M_o, the intensity of low pressure at the cores of threads always decreases as the lowest pressure is associated with the initial vortex tubes before reconnection. Low pressure spatial distribution and sharp rise at higher M_o can be also seen in the near-field pressure evolution on the bridge plane; see Figure 4.3. Owing to the repulsion of the bridges which reduces the high curvature of the reconnected, cusped vortex lines, the bridges extend in the lateral direction; see low pressure extension at $t_E + 2t_R$.

The rise of the near-field low pressure at t_E becomes more obvious by visualizing the volume-averaged pressure isosurface [18]. Evolution of the enstrophy and volume-averaged pressure isosurface at $M_o = 0.5$ is shown in Figure 4.4. The volume-averaged pressure isosurface at each time represents an interface between low pressure near the vortices and high pressure in the far field; so we can monitor the qualitative behavior of the near-field pressure. At the moment of the reconnection, as the lately reconnected vortex lines rapidly recoil from each other by self-induction, low pressure region near the vortices suddenly expands and the pressure isosurface experiences an intense convex twist–compare Figures 4.4(a) and 4.4(b). This twist is mainly oriented in the colliding dipole advection direction, where the pressure isosurface evolves at 53.13% of the reference speed of sound, c_o. As two bridges recoil from each other, low pressure near the vortices is distributed in both axial and lateral directions. Moreover, local pressure increases near the reconnection zone [70]. Therefore, that sudden low pressure expansion retreats and the convex twist of the near-field pressure isosurface flattens in the lateral direction; see Figure 4.4(c). Evolution of the volume-averaged pressure contour at $M_o = 0.5$ on the collision and symmetric planes is shown in Figure 4.5. Local high pressure region near the reconnection zone [70] is observed as an elongated ring just below the kink section in Figure 4.5(b). We expect that the retreat of the low pressure would occur more rapidly at higher Re as the curvature near the cusp of the reconnected vortex lines increases and the repulsion is faster.

The scaling of the overall extrema and maximum amplitude of pressure, which is divided by γP_o, versus M_o is shown in Figure 4.6. The overall extrema and the maximum amplitude

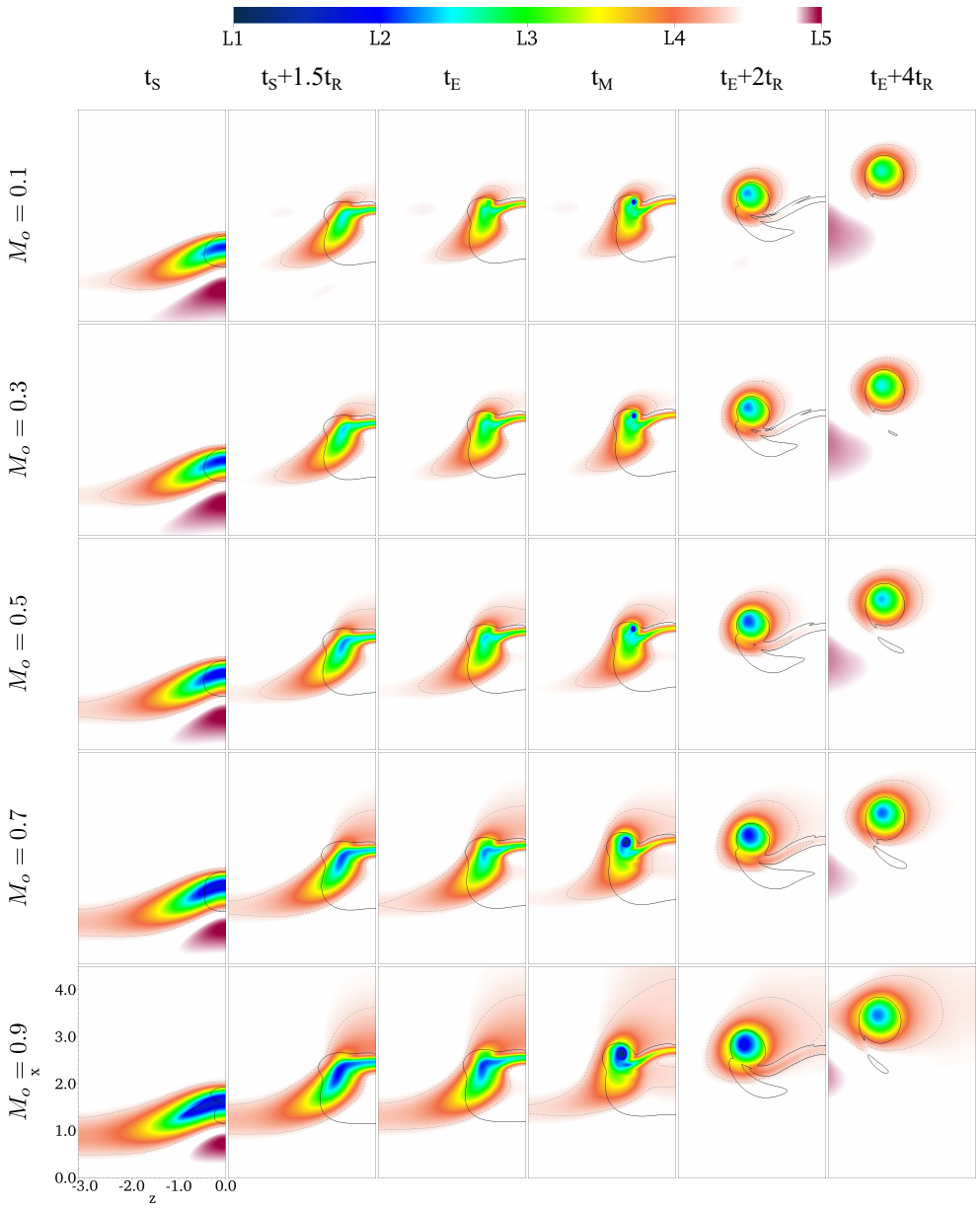

Figure 4.1: Pressure contours on the collision plane. Limits of the global linear legend equal the pressure overall extrema. The black solid line shows the enstrophy contour set at 2% of the overall maximum enstrophy. The gray dashed line shows the pressure contour set at 84.5% of the pressure range.

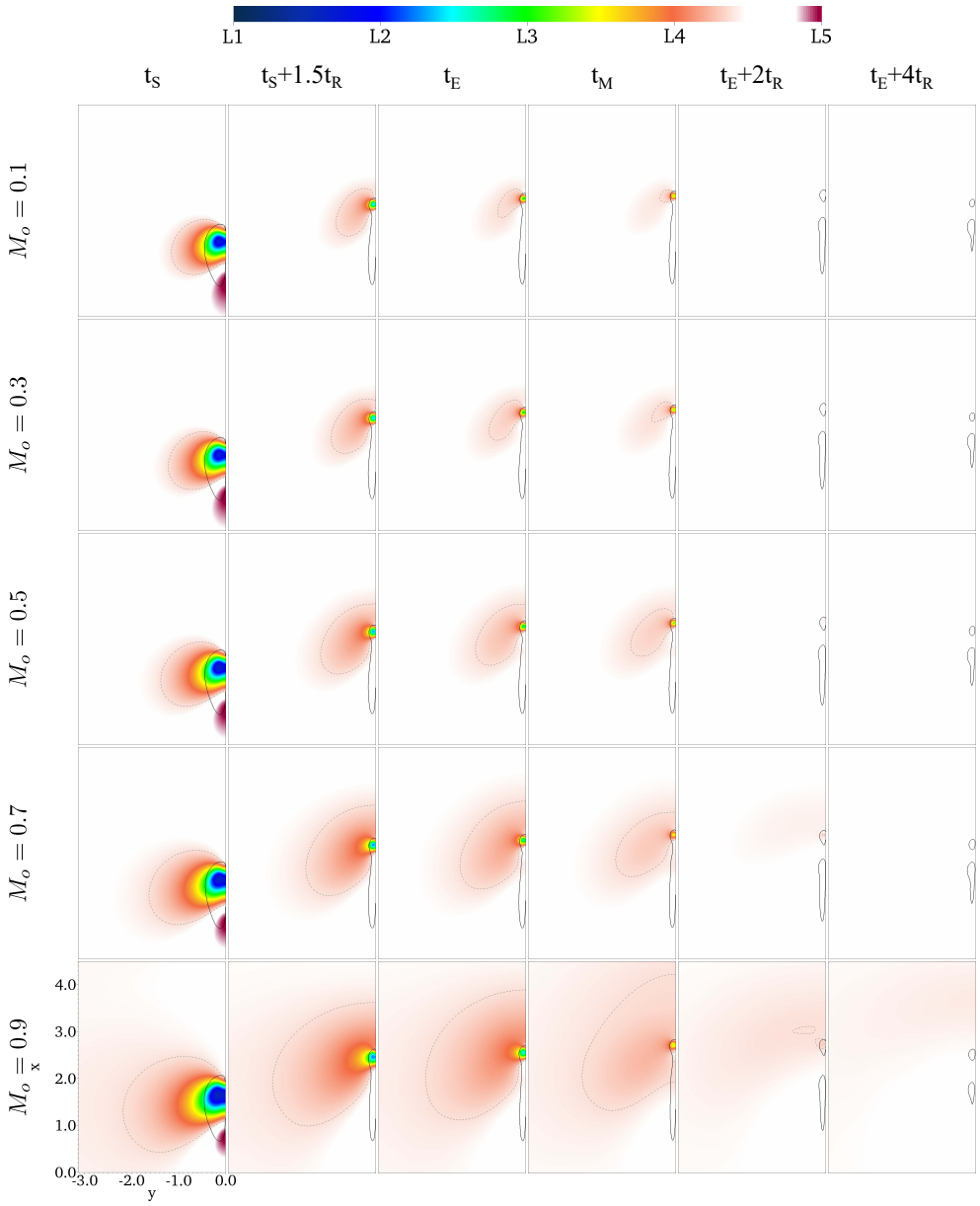

Figure 4.2: Pressure contours on the symmetric plane. The description is the same as in Figure 4.1.

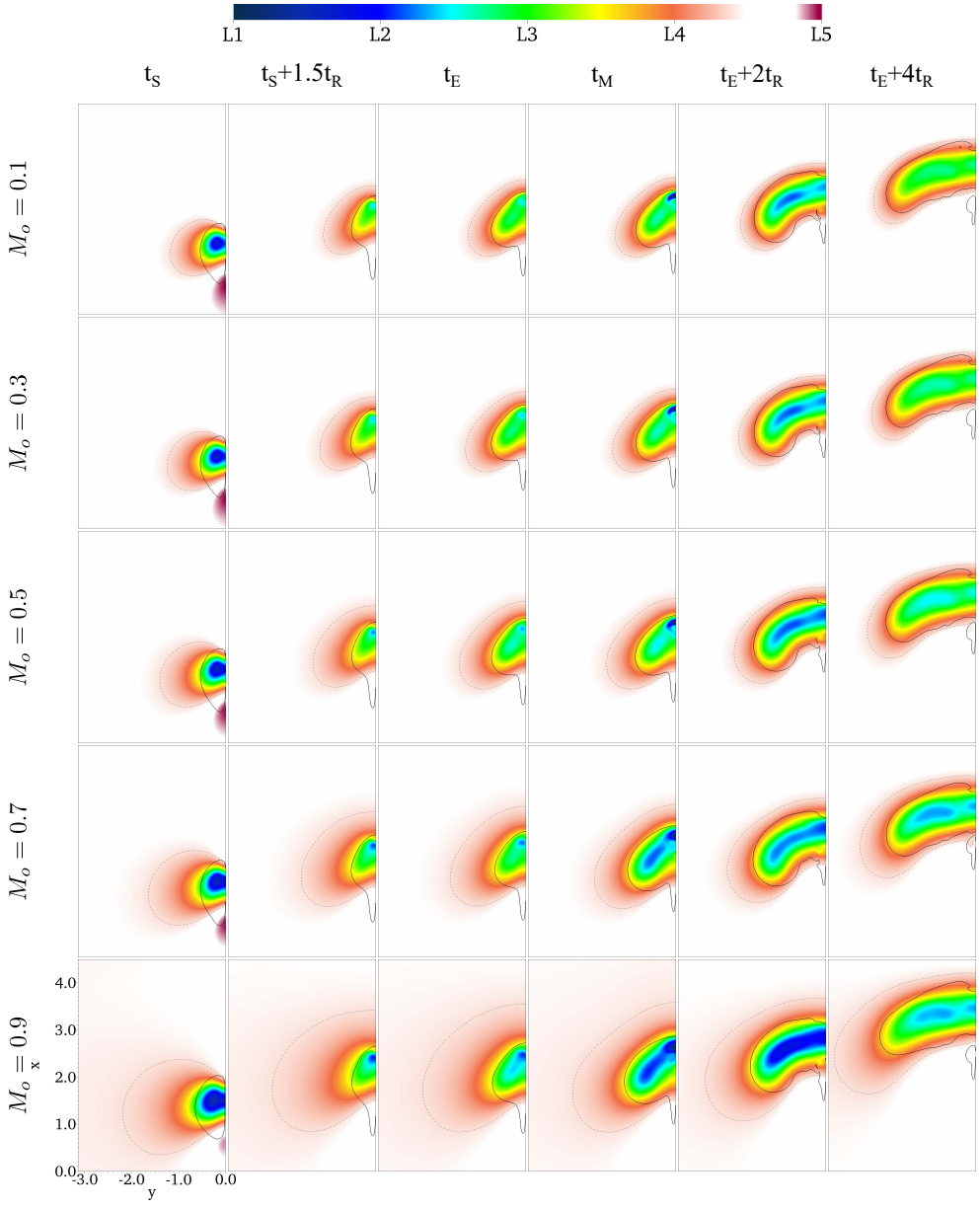

Figure 4.3: Pressure contours on the bridge plane. The description is the same as in Figure 4.1.

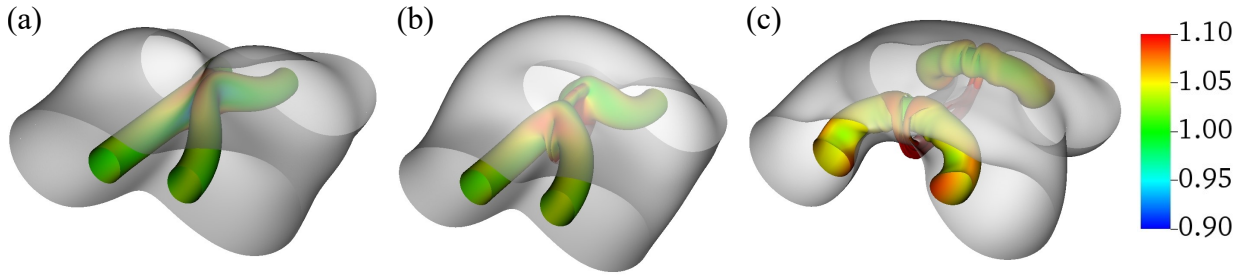

Figure 4.4: Volume-averaged pressure isosurface (gray color) of $M_o = 0.5$ at (a) t_S, (b) t_E, and (c) $t_E + 4t_R$. Color on the enstrophy isosurface (set at 10% of the maximum initial axial vorticity) shows local pressure divided by P_o.

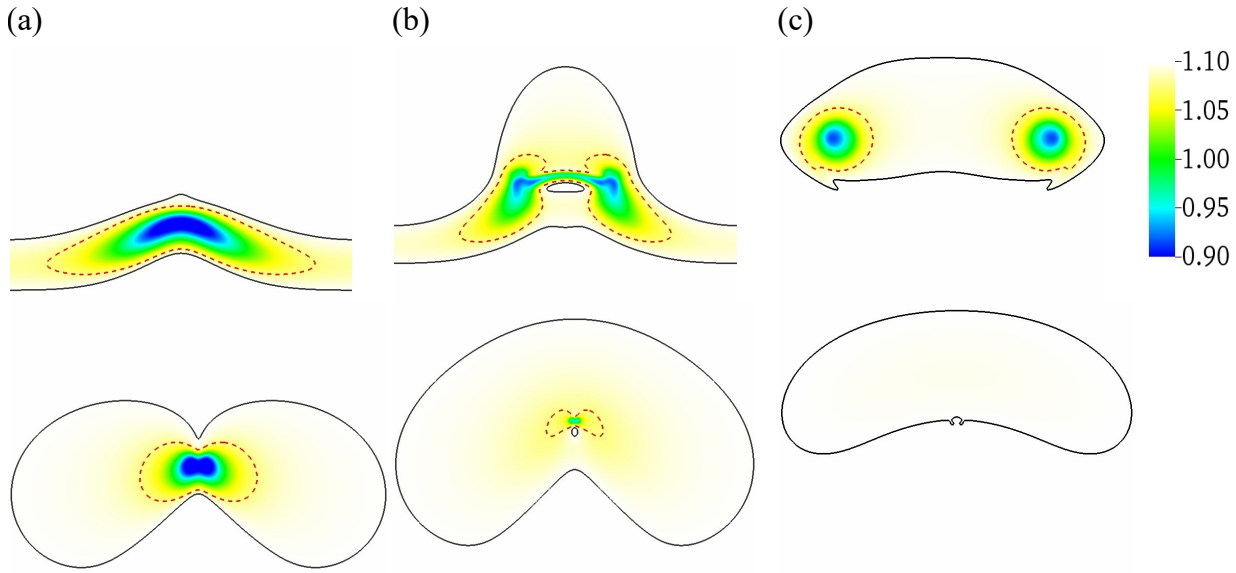

Figure 4.5: Near-field pressure contours of $M_o = 0.5$ on the collision (top row) and symmetric (second row) planes at (a) t_S, (b) t_E, and (c) $t_E + 4t_R$. Red dashed and gray solid lines show contours of pressure (divided by P_o) set at 1.075 and volume-averaged pressure, respectively.

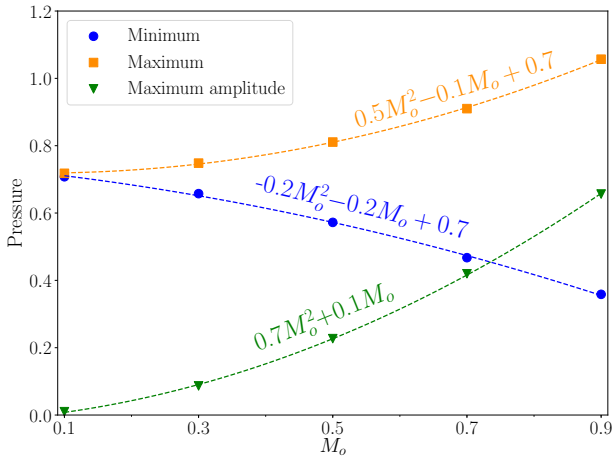

Figure 4.6: Scaling of the overall extrema and maximum amplitude of pressure.

of pressure follow a quadratic behavior with M_o. In other words, not only the low-pressure spatial distribution, but also the pressure amplitude increases with M_o during reconnection. Note that at $M_o = 0.9$ the pressure amplitude is 92% of the reference pressure. We do not expect this scaling to be maintained far into the supersonic regime.

4.2 Far-Field Sound Evolution

Reconnection is a continuous process: anti-parallel vortex lines approach each other by self- and mutual induction, reconnect, and recoil from each other by self-induction. Therefore, characteristic times are defined based on an integral quantity, i.e. circulation. Assuming that reconnection of two anti-parallel vortex lines generates a sound pulse, we do not expect to capture a clear signal in the far-field as reconnection occurs over a finite time and each vortex line reconnects at a slightly different stage during reconnection–some vortex lines are not yet reconnected while others are recoiling from each other. Localized acoustic source terms in the reconnection region could result in intermittent sound radiation [91]. Although some clear instantaneous quadrupole patterns during reconnection of anti-parallel vortex tubes have been found [18], we believe that reconnection of vortex filaments provides a more exact sound pattern and scaling relations. Also, the comparison of the scaling relations of energy exchange in quantum reconnection could be a pivotal foundation in revealing complexities of the impulsive stochasticity and the dissipative feature of turbulent flows [85, 103].

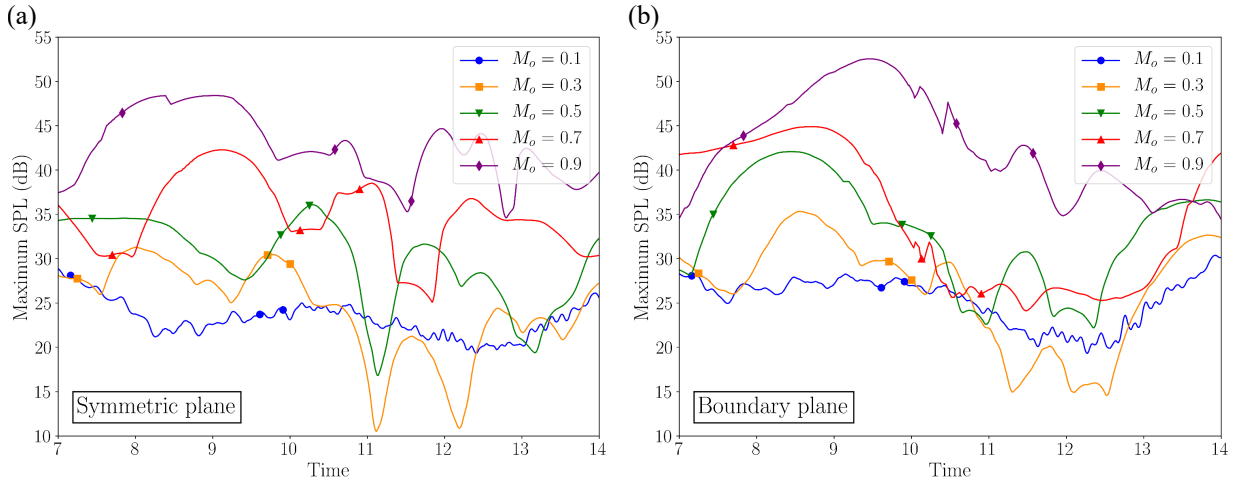

Figure 4.7: Maximum SPL evolution on the (a) symmetric and (b) boundary planes. Markers represent t_S, t_E, and t_M.

Figure 4.7 shows the maximum SPL evolution at different M_o on the symmetric and boundary planes. We assume that the sound source is located at the point with the maximum source term at each time. Then, the corresponding far-field sound is determined by considering a constant speed of sound, c_o; indeed, we offset the time of the far-field sound accordingly. Except for $M_o = 0.1$, a high level of far-field sound is captured during the time interval of $t = [t_S, t_M]$. Note that the maximum sound does not necessarily occur at t_M, implying cancellation of acoustic waves is an important feature. As discussed, the finite time of the viscous reconnection process impedes the emergence of a clear sound pulse; however, the effect of reconnection on far-field sound level, especially at high M_o, can be observed.

Instantaneous sound directivity patterns of $M_o = 0.1, 0.5, 0.9$ at t_S, t_E, and $t_E + 4t_R$ are shown in Figure 4.8. Although the quadrupole pattern is dominant, more complicated directivity patterns also appear during reconnection; see pattern of $M_o = 0.9$ at t_E on the boundary plane in the second row of Figure4.8(b). Patterns of $M_o = 0.1$ are noisy; higher frequency has been also seen in the maximum SPL of $M_o = 0.1$ in Figure 4.7. In [18], the point with the maximum lateral vorticity is considered as the sound source location; therefore, the slight difference between the current results and instantaneous directivity patterns of $M_o = 0.5$ in [18] is acceptable. Increase of SPL by M_o is clear in Figure 4.8.

Figure 4.9 shows the time-averaged (taken over the time interval of $[t_0, t_E+4t_R]$) far-field sound directivity pattern on the symmetric and boundary planes. At low M_o, a quadrupole-

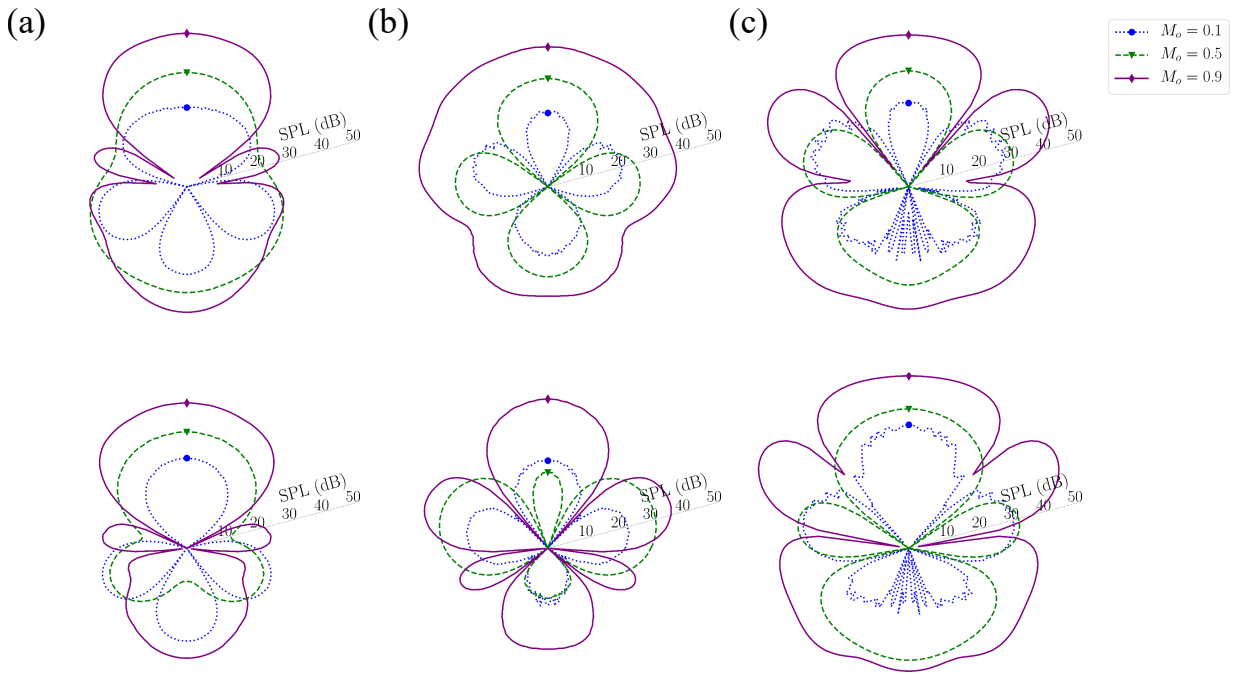

Figure 4.8: Instantaneous sound directivity pattern on the symmetric (top row) and boundary (second row) planes at (a) t_S, (b) t_E, and (c) $t_E + 4t_R$. Markers represent the advection direction.

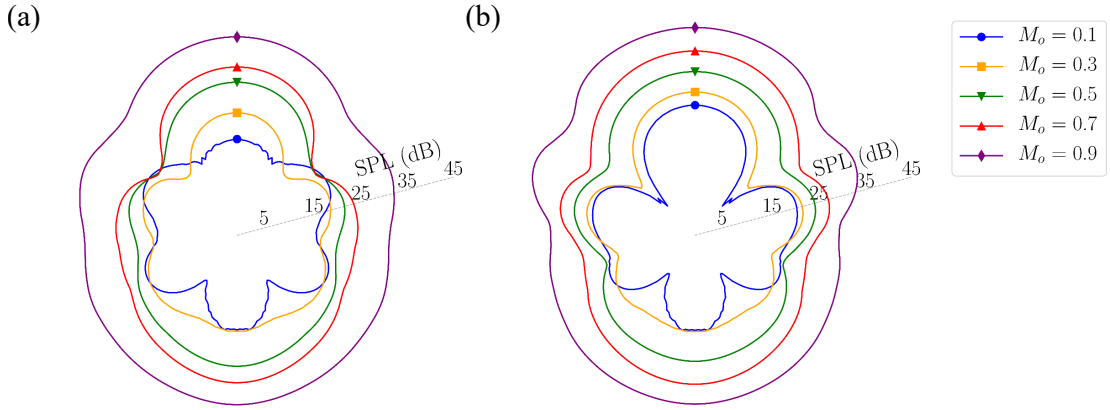

Figure 4.9: Time-averaged far-field sound directivity pattern of the reconnection process on the (a) symmetric and (b) boundary planes. Markers represent the advection direction.

like pattern can be observed. By increase of M_o, not only the sound level intensifies, directivity pattern becomes elongated in the advection direction. Thus, compressibility plays a key role in the sound directivity of the reconnection process.

The scaling of the maximum instantaneous and time-averaged SPL on the symmetric and boundary planes is provided in Figure 4.10. Despite the linear dependence of the maximum time-averaged SPL on M_o, instantaneous SPL follows a quadratic relation, consistent with near-field pressure scaling. There is a small change in the maximum instantaneous SPL for $M_o < 0.3$; see Figure 4.10(a). Note that reconnection at $Re = 1500$ and $M_o = 0.9$ produces up to $52.7dB$ far-field sound, reinforcing the claim that reconnection is one of the vortical interactions producing the most sound.

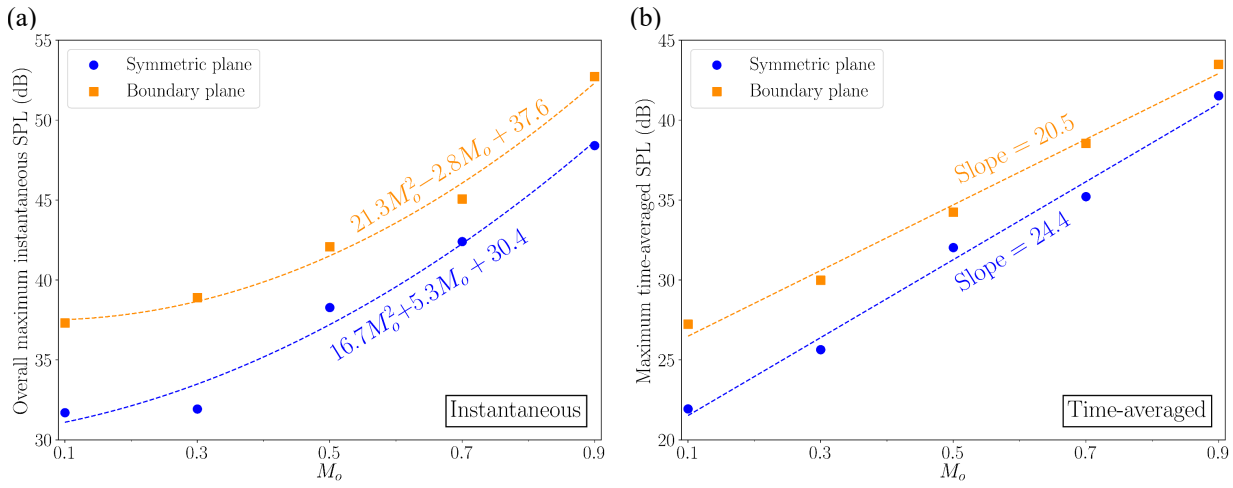

Figure 4.10: Scaling of (a) the overall maximum instantaneous and (b) the maximum time-averaged SPL.

Chapter 5

Summary

5.1 Concluding Remarks

Due to increasingly strict noise regulations, aeroacoustic analysis has become a critical factor in the design of new devices including propulsion, energy, and transportation systems. To control the noise level in these devices, first, dominant noise generation mechanisms should be recognized. It is often acknowledged that coherent vortical structures and their self- and mutual interactions are the main noise sources; however, there is no consensus on the importance of vortex interactions in flow-generated noise. Thus far, dominant acoustic sources, in jet flows, have been attributed to vortex pairing. Meanwhile, it has been claimed that vortex reconnection, which leads to a violent topological change and rapid repulsion of vortex lines, could be considered as a significant contributor to aeroacoustic noise generation [39, 70, 40].

In this thesis, the sound generation mechanism of viscous vortex reconnection via the analysis of the dominant components of Lighthill's source term [66] was studied. The initially subsonic, anti-parallel vortex pair reconnecting at $Re = 1500$ and reference Mach numbers of $M_o = 0.1, 0.3, 0.5, 0.7$, and 0.9 were investigated. Although the time required for the circulation transfer is independent of compressibility, an increase of M_o postpones the onset of reconnection. Compressibility effects are the greatest initially at the entrained jet flow between the approaching vortices preceding reconnection. Soon after the start of reconnection, the regions of high local Mach number migrate towards the bridges. By considering only the time after the start of reconnection, t_S, the overall maximum local Mach number linearly scales as $M_{overall\,max} \approx 1.5 M_o$.

The acoustic source strength is amplified during reconnection and emerges as a jump in the extrema evolution of the source term. Linear scaling of the overall extrema and maximum amplitude of the source term versus M_o manifests the direct effect of compressibility on the source term. To identify the dominant physical mechanisms of sound generation, the source term is decomposed into fourteen physically-meaningful terms and an order-of-magnitude analysis of each is performed. It is shown that dilatation effects and terms containing density gradient can be neglected in the absence of shocklets. Also, at the current Reynolds number, viscous effects do not contribute significantly to the acoustic source term. The Laplacian of the kinetic energy, flexion product, enstrophy, and the deviation from the isentropic condition are found to be the dominant components of the source term. The first three, which are hydrodynamic, scale linearly with M_o; the departure from the isentropic condition follows a quadratic scaling, revealing the importance of the thermodynamic changes during reconnection at high M_o.

The flexion product is a hydrodynamic source term relating the velocity and flexion (curl of vorticity) vectors, and is intensified when these vectors are co-aligned. It is dominant when a twisted vortex tube undergoes a coiling or uncoiling motion. Physically, this arises as the pair of vortical threads are wrapped around the bridges after the end of reconnection, once a rapid strain is applied to the threads by the repulsion of the bridges. This purely hydrodynamic term scales linearly with the reference Mach number of the flow, suggesting an increasing importance of the hydrodynamically-induced noise source as M_o increases.

The spatial distribution of the source term and the vorticity field evolution remain essentially the same during the reconnection at subsonic initial conditions. Exploring the spatial distribution, mutual cancellation of terms A and B becomes apparent (recall that the source terms are defined in equation 2.22) ; unlike term B, term A is negative in vortex cores (due to the enstrophy term) and primarily positive at other regions (due to the flexion product term). Qualitative resemblance between terms A and A+B implies the importance of A over B in vorticity-concentrated regions. Term D (deviation from isentropic conditions) reinforces term A+B; ascendancy of term D2 ($-c_0^2\nabla^2\rho$) over D1 ($\nabla^2 P$) leads to the negative contribution of term D in the vortex cores at the bridges and threads.

At the start of reconnection, the negative source term, due to the enstrophy term, is mainly located at the vortex cores, while the positive part, due to the flexion product, stretches on the collision plane in both axial and advection directions and also bends over the vortices. At later time, due to the deviation from isentropic condition and the enstrophy term at the stretched tail of the well-known head-tail structure appearing as vortex sheets, the negative source term extends on both sides of the collision plane. Once bridge formation is complete, entangled domains of positive and negative source term can

be observed at bridges and threads.

Despite a subsonic reference Mach number of $M_o = 0.9$, reconnection leads to shocklet formation. Density gradient, dilatation, and their interactions are highly sensitive to shocklet formation. Also, due to high velocity variations, contribution of the Laplacian of the kinetic energy becomes important near shocklets. These factors lead to oscillations of the source term prior to the start of reconnection at $M_o = 0.9$. Terms B1, $\rho\nabla^2\left(\frac{|\boldsymbol{v}|^2}{2}\right)$, C1, $\rho\boldsymbol{v}.\boldsymbol{\nabla}(\boldsymbol{\nabla}.\boldsymbol{v})$, and C4, $\boldsymbol{v}.(\boldsymbol{v}.\boldsymbol{\nabla}\boldsymbol{\nabla}\rho)$, are the dominant ones near the shocklets.

Compressibility intensifies the spatial distribution and sharp rise of the near-field low pressure which fade away in time. Also, the overall extrema and the maximum amplitude of pressure are quadratically proportional to M_o. A high level of far-field sound is captured during the circulation transfer. At low M_o, the time-averaged sound directivity takes a quadrupole-like pattern. By increase of M_o, not only the sound level intensifies, but the directivity pattern becomes elongated in the advection direction. Consistent with the near-field pressure, the overall maximum instantaneous SPL follows a quadratic relation with M_o; however, the maximum time-averaged SPL shows a linear behavior. Therefore, reconnection plays a key role in sound generation, especially as compressibility increases.

5.2 Future Work

The physical understanding of the vortex reconnection could reveal many aspects of hidden physics in vortical flows including sound generation mechanism. There are many outstanding subjects on the dynamics of reconnection which have not been studied yet; the most important ones, as the future works of the current thesis, are listed below:

- Effect of Re on sound generation mechanism of reconnection within SPL scaling.
- Reconnection repetition at high Re (see Appendix C) and domain size effect on the generation of small-scale structures. As threads can expand in an extended domain, it is not expected to capture the second reconnection at the same high Re where reconnection repetition takes place in a small domain.
- Effect of Re on the hydrodynamics of reconnection near the sonic threshold and possibility of modification of reconnection process due to shock formation as M_{max} increases by Re; see Figure C.1(f).
- Dominant sound generation mechanism of supersonic reconnection.

- Determination of the exact near-field sound sources through analytical solution of the wave equation for different source terms.
- Role of different vorticity generation mechanisms and possibility of singularity occurrence in compressible reconnection.

These subjects help reveal sound generation mechanisms in vortical flows and understand the physics of compressible turbulent energy cascade.

References

[1] S. Adachi, K. Ishh, and T. Kambe. Vortex sound associated with vortexline reconnection in oblique collision of two vortex rings. *ZAMM-Journal of Applied Mathematics and Mechanics/Zeitschrift für Angewandte Mathematik und Mechanik*, 77(9):716–719, 1997.

[2] Hassan Aref and Ireneusz Zawadzki. Linking of vortex rings. *Nature*, 354(6348):50, 1991.

[3] Wm T Ashurst and DI Meiron. Numerical study of vortex reconnection. *Physical review letters*, 58(16):1632, 1987.

[4] F. Bastin, P. Lafon, and S. Candel. Computation of jet mixing noise due to coherent structures: the plane jet case. *Journal of Fluid Mechanics*, 335:261–304, 1997.

[5] Guillaume Beardsell, Louis Dufresne, and Guy Dumas. Investigation of the viscous reconnection phenomenon of two vortex tubes through spectral simulations. *Physics of Fluids*, 28(9):095103, 2016.

[6] I. Bermejo-Moreno, J. Bodart, J. Larsson, B. M. Barney, J. W. Nichols, and S. Jones. Solving the compressible navier-stokes equations on up to 1.97 million cores and 4.1 trillion grid points. In *SC'13: Proceedings of the International Conference on High Performance Computing, Networking, Storage and Analysis*, pages 1–10. IEEE, 2013.

[7] Gregory P Bewley, Matthew S Paoletti, Katepalli R Sreenivasan, and Daniel P Lathrop. Characterization of reconnecting vortices in superfluid helium. *Proceedings of the National Academy of Sciences*, 105(37):13707–13710, 2008.

[8] Dieter Biskamp. Magnetic reconnection in plasmas. *Astrophysics and Space Science*, 242(1-2):165–207, 1996.

[9] ON Boratav, RB Pelz, and NJ Zabusky. Reconnection in orthogonally interacting vortex tubes: Direct numerical simulations and quantifications. *Physics Fluids*, 4(3):581–605, 1992.

[10] M. Cabana, V. Fortuné, and P. Jordan. Identifying the radiating core of lighthill's source term. *Theoretical and Computational Fluid Dynamics*, 22(2):87–106, 2008.

[11] Patrick Chassaing, RA Antonia, Fabien Anselmet, L Joly, and Sahotra Sarkar. *Variable density fluid turbulence*, volume 69. Springer Science & Business Media, 2002.

[12] Philippe Chatelain, Demosthenes Kivotides, and Anthony Leonard. Reconnection of colliding vortex rings. *Physical review letters*, 90(5):054501, 2003.

[13] F. Coiffet, P. Jordan, J. Delville, Y. Gervais, and F. Ricaud. Coherent structures in subsonic jets: a quasi-irrotational source mechanism? *International Journal of Aeroacoustics*, 5(1):67–89, 2006.

[14] T. Colonius, S. K. Lele, and P. Moin. Sound generation in a mixing layer. *Journal of Fluid Mechanics*, 330:375–409, 1997.

[15] D. G. Crighton. Acoustics as a branch of fluid mechanics. *Journal of Fluid Mechanics*, 106:261–298, 1981.

[16] DG Crighton. The excess noise field of subsonic jets. *Journal of Fluid Mechanics*, 56(4):683–694, 1972.

[17] S. C. Crow. Stability theory for a pair of trailing vortices. *AIAA Journal*, 8(12):2172–2179, 1970.

[18] H. Daryan, F. Hussain, and J.-P. Hickey. Aeroacoustic noise generation due to vortex reconnection. *Physical Review Fluids*, 5(6):062702, 2020.

[19] H. Daryan, F. Hussain, and J.-P. Hickey. Sound generation mechanism of compressible vortex reconnection. *Journal of Fluid Mechanics, submitted*, 2021.

[20] H.M.M. Daryan, F. Hussain, and J.-P. Hickey. Aeroacoustic noise generation in compressible vortex reconnection. In *11th International Symposium on Turbulence and Shear Flow Phenomena, TSFP 2019*, 2019.

[21] J Delfs. Grundlagen der aeroakustik (basics of aeroacoustics). *Technische Universität Braunschweig, Braunschweig*, 2014.

[22] Darshan S Dosanjh and Thomas M Weeks. Interaction of a starting vortex as well as a vortex street with a traveling shock wave. *AIAA journal*, 3(2):216–223, 1965.

[23] F. Ducros, F. Laporte, T. Soulères, V. Guinot, P. Moinat, and B. Caruelle. High-order fluxes for conservative skew-symmetric-like schemes in structured meshes: application to compressible flows. *Journal of Computational Physics*, 161(1):114–139, 2000.

[24] J. D. Eldredge. The dynamics and acoustics of viscous two-dimensional leapfrogging vortices. *Journal of Sound and Vibration*, 301(1-2):74–92, 2007.

[25] Gordon Erlebacher, MY Hussaini, HO Kreiss, and S Sarkar. The analysis and simulation of compressible turbulence. *Theoretical and Computational Fluid Dynamics*, 2(2):73–95, 1990.

[26] T Fohl and JS Turner. Colliding vortex rings. *The Physics of Fluids*, 18(4):433–436, 1975.

[27] Enrico Fonda, David P Meichle, Nicholas T Ouellette, Sahand Hormoz, and Daniel P Lathrop. Direct observation of kelvin waves excited by quantized vortex reconnection. *Proceedings of the National Academy of Sciences*, 111(Supplement 1):4707–4710, 2014.

[28] Stewart Glegg and William Devenport. *Aeroacoustics of low Mach number flows: fundamentals, analysis, and measurement*. Academic Press, 2017.

[29] F. Golanski, V. Fortuné, and E. Lamballais. Noise radiated by a non-isothermal, temporal mixing layer. *Theoretical and Computational Fluid Dynamics*, 19(6):391–416, 2005.

[30] G. Guj, M. Carley, R. Camussi, and A. Ragni. Acoustic identification of coherent structures in a turbulent jet. *Journal of Sound and Vibration*, 259(5):1037–1065, 2003.

[31] C. W. Hamman, J. C. Klewicki, and R. M. Kirby. On the lamb vector divergence in navier–stokes flows. *Journal of Fluid Mechanics*, 610:261–284, 2008.

[32] J.-P. Hickey, F. Hussain, and X. Wu. Compressibility effects on the structural evolution of transitional high-speed planar wakes. *Journal of Fluid Mechanics*, 796:5, 2016.

[33] LN Howard and DL Matthews. On the vortices produced in shock diffraction. *Journal of Applied Physics*, 27(3):223–231, 1956.

[34] AKM Fazle Hussain. Coherent structures and turbulence. *Journal of Fluid Mechanics*, 173:303–356, 1986.

[35] AKM Fazle Hussain and HS Husain. Passive and active control of jet turbulence. In *Turbulence Management and Relaminarisation*, pages 445–457. Springer, 1988.

[36] AKMF Hussain. Coherent structures–reality and myth. *Phys. Fluids*, 26(10):2816–2850, 1983.

[37] AKMF Hussain and MAZ Hasan. Turbulence suppression in free turbulent shear flows under controlled excitation. part 2. jet-noise reduction. *Journal of Fluid Mechanics*, 150:159–168, 1985.

[38] AKMF Hussain and KBMQ Zaman. Vortex pairing in a circular jet under controlled excitation. part 2. coherent structure dynamics. *Journal of Fluid Mechanics*, 101(3):493–544, 1980.

[39] AKMF Hussain and KBMQ Zaman. The preferred mode of the axisymmetric jet. *J. Fluid Mech.*, 110:39–71, 1981.

[40] F. Hussain and K. Duraisamy. Mechanics of viscous vortex reconnection. *Physics of Fluids*, 23(2):021701, 2011.

[41] Fazle Hussain and Hyder S Husain. Elliptic jets. part 1. characteristics of unexcited and excited jets. *Journal of Fluid Mechanics*, 208:257–320, 1989.

[42] Fazle Hussain and Mogens V Melander. Understanding turbulence via vortex dynamics. In *Studies in turbulence*, pages 157–178. Springer, 1992.

[43] Fazle Hussain, Davinder Virk, and Mogens V Melander. New studies in vortex dynamics: Incompressible and compressible vortex reconnection, core dynamics, and coupling between large and small scales. *Sadhana*, 18(3-4):477–529, 1993.

[44] Fazle Hussain and Jie Yao. Evidence of physical turbulence cascade mechanism via reconnection cascade scenario. *Bulletin of the American Physical Society*, 2018.

[45] O Inoue, Y Hattori, and T Sasaki. Sound generation by coaxial collision of two vortex rings. *Journal of Fluid Mechanics*, 424:327–365, 2000.

[46] K. Ishii, S. Adachi, and T. Kambe. Sound generation in oblique collision of two vortex rings. *Journal of the Physical Society of Japan*, 67(7):2306–2314, 1998.

[47] Eric Johnsen, Johan Larsson, Ankit V Bhagatwala, William H Cabot, Parviz Moin, Britton J Olson, Pradeep S Rawat, Santhosh K Shankar, Björn Sjögreen, Helen C Yee, et al. Assessment of high-resolution methods for numerical simulations of compressible turbulence with shock waves. *Journal of Computational Physics*, 229(4):1213–1237, 2010.

[48] T Kambe and T Minota. Acoustic wave radiated by head-on collision of two vortex rings. *Proc. R. Soc. Lond. A*, 386(1791):277–308, 1983.

[49] T. Kambe, T. Minota, and M. Takaoka. Oblique collision of two vortex rings and its acoustic emission. *Physical Review E*, 48(3):1866, 1993.

[50] R. Kerr, D. Virk, and F. Hussain. Effects of incompressible and compressible vortex reconnection. *Topological Fluid Mechanics*, pages 500–514, 1989.

[51] Robert M Kerr. Swirling, turbulent vortex rings formed from a chain reaction of reconnection events. *Physics of Fluids*, 25(6):065101, 2013.

[52] Robert M Kerr and Fazle Hussain. Simulation of vortex reconnection. *Physica D: Nonlinear Phenomena*, 37(1-3):474–484, 1989.

[53] V. Kibens. Discrete noise spectrum generated by acoustically excited jet. *AIAA Journal*, 18(4):434–441, 1980.

[54] S. Kida and M. Takaoka. Bridging in vortex reconnection. *Physics of Fluids*, 30(10):2911–2914, 1987.

[55] S. Kida and M. Takaoka. Vortex reconnection. *Annual Review of Fluid Mechanics*, 26(1):169–177, 1994.

[56] S. Kida, M. Takaoka, and F. Hussain. Collision of two vortex rings. *Journal of Fluid Mechanics*, 230:583–646, 1991.

[57] S Kida, M Takaoka, and Fazle Hussain. Reconnection of two vortex rings. *Physics of Fluids A: Fluid Dynamics*, 1(4):630–632, 1989.

[58] Dustin Kleckner and William TM Irvine. Creation and dynamics of knotted vortices. *Nature physics*, 9(4):253, 2013.

[59] Dustin Kleckner, Louis H Kauffman, and William TM Irvine. How superfluid vortex knots untie. *Nature Physics*, 12(7):650, 2016.

[60] Pijush K. Kundu, Ira M Cohen, and David R Dowling. *Fluid mechanics*. Waltham, MA Academic Press, 6th edition, 2016.

[61] Christian E Laing, Renzo L Ricca, and L Sumners De Witt. Conservation of writhe helicity under anti-parallel reconnection. *Scientific reports*, 5:9224, 2015.

[62] J Larsson, SK Lele, and P Moin. Effect of numerical dissipation on the predicted spectra for compressible turbulence. *Annual Research Briefs*, pages 47–57, 2007.

[63] J. Laufer and T.-C. Yen. Noise generation by a low-mach-number jet. *Journal of Fluid Mechanics*, 134:1–31, 1983.

[64] M Leadbeater, T Winiecki, DC Samuels, CF Barenghi, and CS Adams. Sound emission due to superfluid vortex reconnections. *Physical Review Letters*, 86(8):1410, 2001.

[65] CB Lee and S Fu. On the formation of the chain of ring-like vortices in a transitional boundary layer. *Experiments in fluids*, 30(3):354–357, 2001.

[66] M. J. Lighthill. On sound generated aerodynamically i. general theory. *Proceedings of the Royal Society of London. Series A. Mathematical and Physical Sciences*, 211(1107):564–587, 1952.

[67] M. Mancinelli, T. Pagliaroli, A. Di Marco, R. Camussi, and T. Castelain. Wavelet decomposition of hydrodynamic and acoustic pressures in the near field of the jet. *Journal of Fluid Mechanics*, 813:716–749, 2017.

[68] M. J. Mandella. *Experimental and analytical studies of compressible vortices*. PhD thesis, Stanford Univ., CA., December 1987.

[69] Philip McGavin and David I Pontin. Vortex line topology during vortex tube reconnection. *Physical Review Fluids*, 3(5):054701, 2018.

[70] Mogens V Melander and Fazle Hussain. Cut-and-connect of two antiparallel vortex tubes. *in Studying Turbulence Using Numerical Simulation Databases, Proceedings of the 1988 Summer Program (Stanford University, Stanford, CA, 1988), pp. 257–286*, 1988.

[71] Mogens V Melander and Fazle Hussain. Core dynamics on a vortex column. *Fluid dynamics research*, 13(1):1, 1994.

[72] MV Melander and Fazle Hussain. Cross-linking of two antiparallel vortex tubes. *Physics of Fluids A: Fluid Dynamics*, 1(4):633–636, 1989.

[73] Melander Mogens V and Zabusky Norman J. Interaction and "apparent" reconnection of 3d vortex tubes via direct numerical simulations. *Fluid Dynamics Research*, 3(1-4):247–250, 1988.

[74] W Möhring. On vortex sound at low mach number. *J. Fluid Mech.*, 85(4):685–691, 1978.

[75] Marc Montagnac. Variable normalization (nondimensionalization and scaling) for navier-stokes equations: a practical guide. *Centre Européen de Recherche et de Formation Avancée en Calcul Scientifique, Tech. Rep. TRF-CFD-13-77*, 2013.

[76] Joseph Mouallem, Joshua Wawryk, Hamid Daryan, Zhao Pan, and Jean-Pierre Hickey. Targeted particle delivery via vortex ring reconnection. *arXiv preprint arXiv:2012.00721*, 2020.

[77] Yoshitaka Nakashima. Sound generation by head-on and oblique collisions of two vortex rings. *Physics of Fluids*, 20(5):056102, 2008.

[78] Yuko Oshima and Saburo Asaka. Interaction of two vortex rings along parallel axes in air. *Journal of the Physical Society of Japan*, 42(2):708–713, 1977.

[79] Yuko Oshima and Naoki Izutsu. Cross-linking of two vortex rings. *The Physics of fluids*, 31(9):2401–2403, 1988.

[80] C Pantano and S Sarkar. A study of compressibility effects in the high-speed turbulent shear layer using direct simulation. *Journal of Fluid Mechanics*, 451:329, 2002.

[81] P. Paredes, J. W. Nichols, K. Duraisamy, and F. Hussain. Aeroacoustics of viscous vortex reconnection. In *Bulletin of the American Physical Society DFD*, volume 64, pages D21–009, 2011.

[82] N. Peng and Y. Yang. Effects of the mach number on the evolution of vortex-surface fields in compressible taylor-green flows. *Physical Review Fluids*, 3(1):013401, 2018.

[83] A. Powell. Theory of vortex sound. *Journal Acoustic Society of America*, 36(1):177–195, 1964.

[84] Eric Priest and Terry Forbes. Magnetic reconnection. *Magnetic Reconnection, by Eric Priest, Terry Forbes, Cambridge, UK: Cambridge University Press, 2007*, 2007.

[85] D. Proment and G. Krstulovic. Matching theory to characterize sound emission during vortex reconnection in quantum fluids. *Physical Review Fluids*, 5:104701, Oct 2020.

[86] Alain Pumir and Robert M Kerr. Numerical simulation of interacting vortex tubes. *Physical review letters*, 58(16):1636, 1987.

[87] Alain Pumir and Eric D Siggia. Vortex dynamics and the existence of solutions to the navier–stokes equations. *The Physics of fluids*, 30(6):1606–1626, 1987.

[88] PG Saffman. A model of vortex reconnection. *Journal of Fluid Mechanics*, 212:395–402, 1990.

[89] Paul Russell Schatzle. *An experimental study of fusion of vortex rings*. PhD thesis, California Institute of Technology, 1987.

[90] Martin W Scheeler, Dustin Kleckner, Davide Proment, Gordon L Kindlmann, and William TM Irvine. Helicity conservation by flow across scales in reconnecting vortex links and knots. *Proceedings of the National Academy of Sciences*, 111(43):15350–15355, 2014.

[91] T. E. Scheidegger. *On compressibility effects in two-and three-dimensional flows: Vortex dipoles and reconnection.* PhD thesis, Rutgres University, New Brunswick, NJ, 1998.

[92] RS Scorer and LJ Davenport. Contrails and aircraft downwash. *Journal of Fluid Mechanics*, 43(3):451–464, 1970.

[93] R. K. Shah. A Correlation for Laminar Hydrodynamic Entry Length Solutions for Circular and Noncircular Ducts. *J Fluids Eng.*, 100(2):177–179, 06 1978.

[94] Karim Shariff and Anthony Leonard. Vortex rings. *Annual Review of Fluid Mechanics*, 24(1):235–279, 1992.

[95] MJ Shelley, DI Meiron, and SA Orszag. Dynamical aspects of vortex reconnection of perturbed anti-parallel vortex tubes. *Journal of Fluid Mechanics*, 246:613–652, 1993.

[96] B. K. Shivamoggi. Vortex stretching and reconnection in a compressible fluid. *The European Physical Journal B-Condensed Matter and Complex Systems*, 49(4):483, 2006.

[97] Bhimsen K Shivamoggi. Vortex reconnection in a compressible fluid. *Physica Scripta*, 53(6):703, 1996.

[98] E.D. Siggia. Collapse and amplification of a vortex filament. *Physics of Fluids*, 28(3):794–805, 1985.

[99] JBj Taylor. Relaxation and magnetic reconnection in plasmas. *Reviews of Modern Physics*, 58(3):741, 1986.

[100] P.A. Thompson. *Compressible-fluid Dynamics*. Advanced engineering series. McGraw-Hill, 1971.

[101] Wim M van Rees. Vortex bursting. *Physical Review Fluids*, 5(11):110504, 2020.

[102] Wim M van Rees, Fazle Hussain, and Petros Koumoutsakos. Vortex tube reconnection at re= 104. *Physics of fluids*, 24(7):075105, 2012.

[103] A. Villois, D. Proment, and G. Krstulovic. Irreversible dynamics of vortex reconnections in quantum fluids. *Physical Review Letters*, 125:164501, Oct 2020.

[104] Daniele Violato and Fulvio Scarano. Three-dimensional evolution of flow structures in transitional circular and chevron jets. *Phys. Fluids*, 23(12):124104, 2011.

[105] Daniele Violato and Fulvio Scarano. Three-dimensional vortex analysis and aeroacoustic source characterization of jet core breakdown. *Phys. fluids*, 25(1):015112, 2013.

[106] D. Virk, F. Hussain, and R.M. Kerr. Compressible vortex reconnection. *Journal of Fluid Mechanics*, 304:47–86, 1995.

[107] D Virk and Fazle Hussain. Influence of initial conditions on compressible vorticity dynamics. *Theoretical and Computational Fluid Dynamics*, 5(6):309–334, 1993.

[108] J. E. Ffowcs Williams and A. J. Kempton. The noise from the large-scale structure of a jet. *Journal of Fluid Mechanics*, 84(4):673–694, 1978.

[109] Jie-Zhi Wu, Hui-Yang Ma, and M-D Zhou. *Vorticity and vortex dynamics*. Springer Science & Business Media, 2007.

[110] J. Yao and F. Hussain. A physical model of turbulence cascade via vortex reconnection sequence and avalanche. *Journal of Fluid Mechanics*, 883, 2020.

[111] NJ Zabusky and MV Melander. Three-dimensional vortex tube reconnection: morphology for orthogonally-offset tubes. *Physica D: Nonlinear Phenomena*, 37(1-3):555–562, 1989.

[112] Norman J Zabusky, ON Boratav, RB Pelz, M Gao, Deborah Silver, and SP Cooper. Emergence of coherent patterns of vortex stretching during reconnection: A scattering paradigm. *Physical Review Letters*, 67(18):2469, 1991.

[113] K. B. M. Q. Zaman and A. K. M. F. Hussain. Turbulence suppression in free shear flows by controlled excitation. *Journal of Fluid Mechanics*, 103:133–159, 1981.

[114] KBMQ Zaman. Far-field noise of a subsonic jet under controlled excitation. *Journal of Fluid Mechanics*, 152:83–111, 1985.

[115] GP Zank and WH Matthaeus. The equations of nearly incompressible fluids. i. hydrodynamics, turbulence, and waves. *Physics of Fluids A: Fluid Dynamics*, 3(1):69–82, 1991.

APPENDICES

Appendix A

Expanded Mathematical Relations

In this section, relations containing $\boldsymbol{\xi}$, which were mentioned in Chapter 2 and are expected to be important in hypersonic reconnection, are expanded:

$$\boldsymbol{\nabla}.\boldsymbol{\xi} = \boldsymbol{\nabla}.(2\boldsymbol{S} \odot \boldsymbol{\nabla}\mu) - \frac{2}{3}(\boldsymbol{\nabla}.\boldsymbol{v})\nabla^2\mu - \frac{2}{3}\boldsymbol{\nabla}(\boldsymbol{\nabla}.\boldsymbol{v}).\boldsymbol{\nabla}\mu \tag{A.1}$$

$$\begin{aligned}\boldsymbol{\nabla}\times(\frac{1}{\rho}\boldsymbol{\xi}) =& \frac{1}{\rho}\,\boldsymbol{\nabla}\times\,(2\boldsymbol{S} \odot \boldsymbol{\nabla}\mu) + \frac{1}{\rho^2}(2\boldsymbol{S} \odot \boldsymbol{\nabla}\mu) \times\boldsymbol{\nabla}\,\rho \\ &+\frac{2}{3}\frac{1}{\rho}\boldsymbol{\nabla}\mu \times\boldsymbol{\nabla}\,(\boldsymbol{\nabla}.\boldsymbol{v}) + \frac{2}{3}\frac{(\boldsymbol{\nabla}.\boldsymbol{v})}{\rho^2}\boldsymbol{\nabla}\rho \times\boldsymbol{\nabla}\,\mu\end{aligned} \tag{A.2}$$

$$\oint_C \frac{1}{\rho}\boldsymbol{\xi}.\boldsymbol{ds} = \oint_C \frac{1}{\rho}(2\boldsymbol{S} \odot \boldsymbol{\nabla}\mu).\boldsymbol{ds} - \oint_C \frac{2}{3}\frac{(\boldsymbol{\nabla}.\boldsymbol{v})}{\rho}\boldsymbol{\nabla}\mu.\boldsymbol{ds} \tag{A.3}$$

Appendix B

Contours and Isosurfaces

In this section additional useful contours and isosurfaces of the source term and other interesting variables are presented.

Figures B.1 and B.2 respectively show the evolution of isosurface of the flexion product, $\rho \boldsymbol{v}.(\boldsymbol{\nabla} \times \boldsymbol{\omega})$, and the helicity density, $h = \boldsymbol{v}.\boldsymbol{\omega}$, at $M_o = 0.5$. Dominance of the positive flexion product isosurface is obvious in Figure B.1. Also, as seen in Figure B.2, helicity density field at the current moderate Re is anti-symmetric in the both axial and lateral directions.

Figures B.3 and B.4 show the source term contour evolution for different M_o on the symmetric and bridge planes, respectively. Current figures endorse the discussion of Section 3.4 that the spatial distribution of the source term and the vorticity field evolution remain essentially the same during the reconnection with subsonic initial conditions; however, same as Figure 3.12, an intensification of the localized source term at higher M_o is clear. Note that due to the moderate Re of the cases and symmetric spatial evolution of the source term, only half of the characteristic planes are presented.

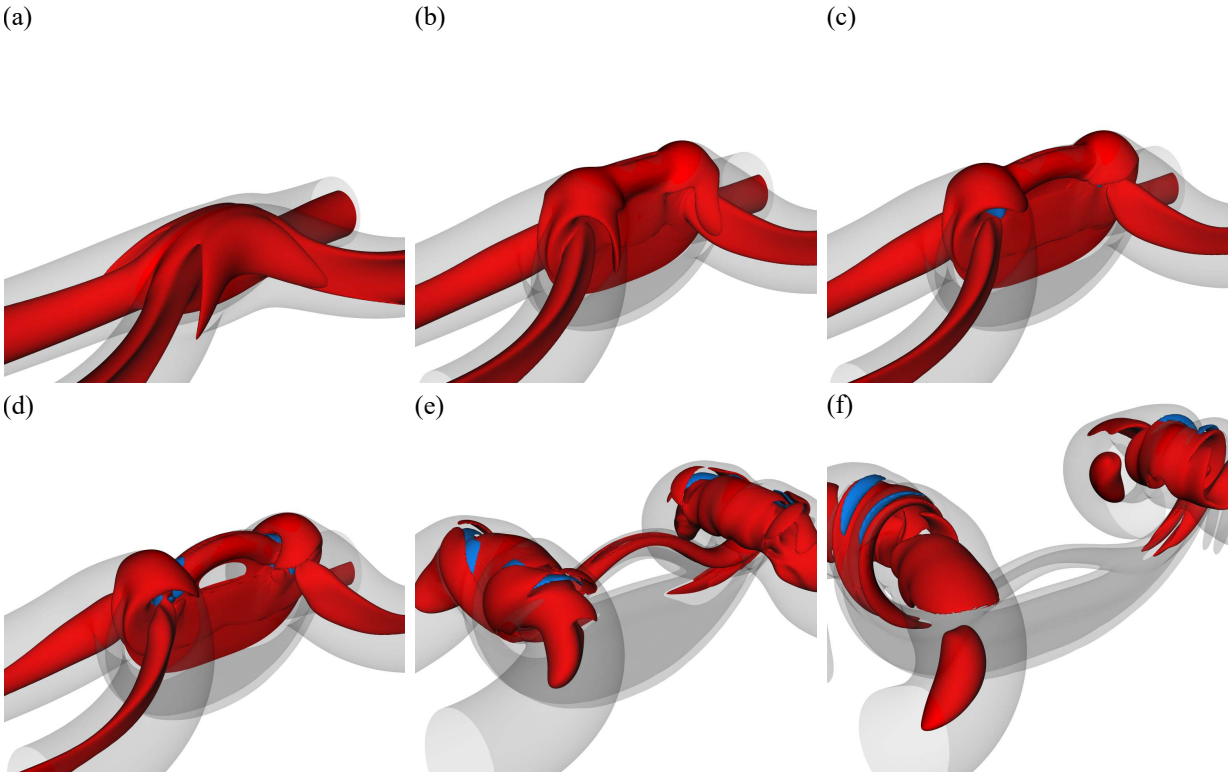

Figure B.1: Flexion product isosurface of $M_o = 0.5$ at (a) t_S, (b) $t_S + 1.5t_R$, (c) t_E, (d) t_M, (e) $t_E + 2t_R$, and (f) $t_E + 4t_R$. Blue and red isosurface levels equal the negative and positive 1% of the overall maximum absolute value of the flexion product. Gray transparent color shows the enstrophy isosurface set at 2% of the overall maximum enstrophy.

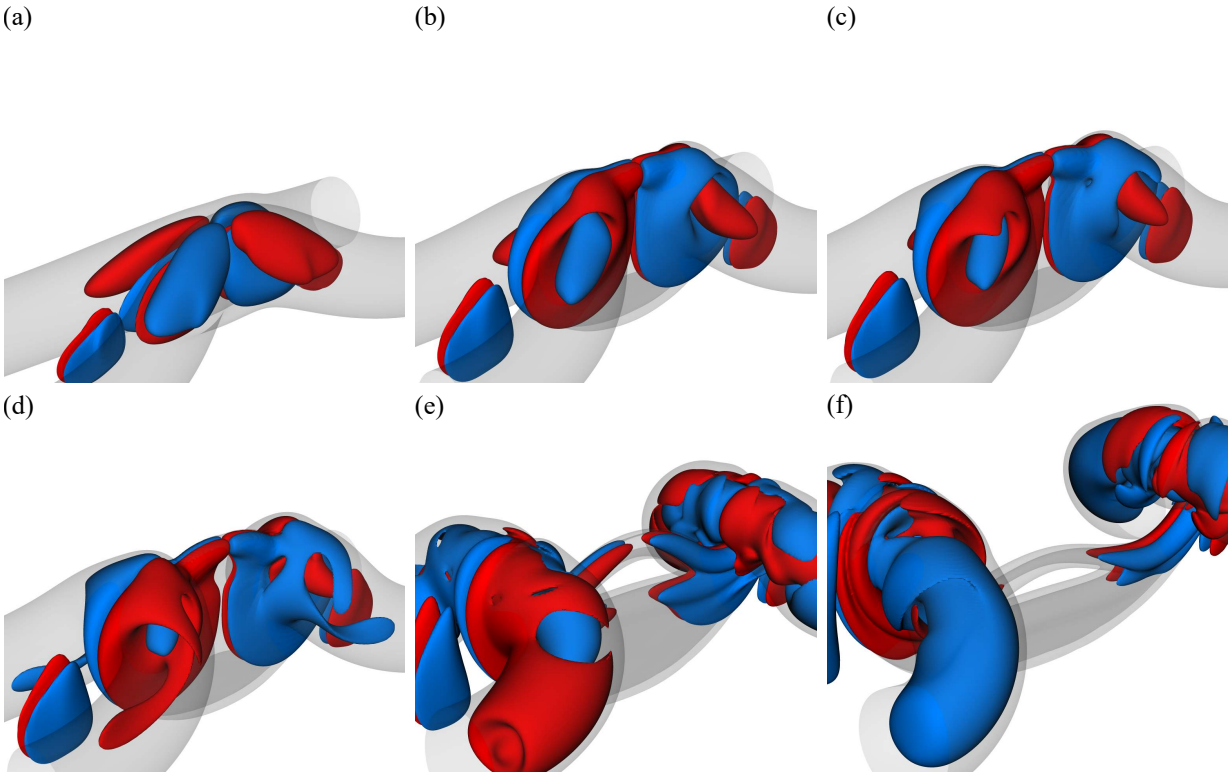

Figure B.2: Helicity isosurface of $M_o = 0.5$ at (a) t_S, (b) $t_S + 1.5t_R$, (c) t_E, (d) t_M, (e) $t_E + 2t_R$, and (f) $t_E + 4t_R$. Blue and red isosurface levels equal the negative and positive 1% of the overall maximum absolute value of the helicity. Gray transparent color shows the enstrophy isosurface set at 2% of the overall maximum enstrophy.

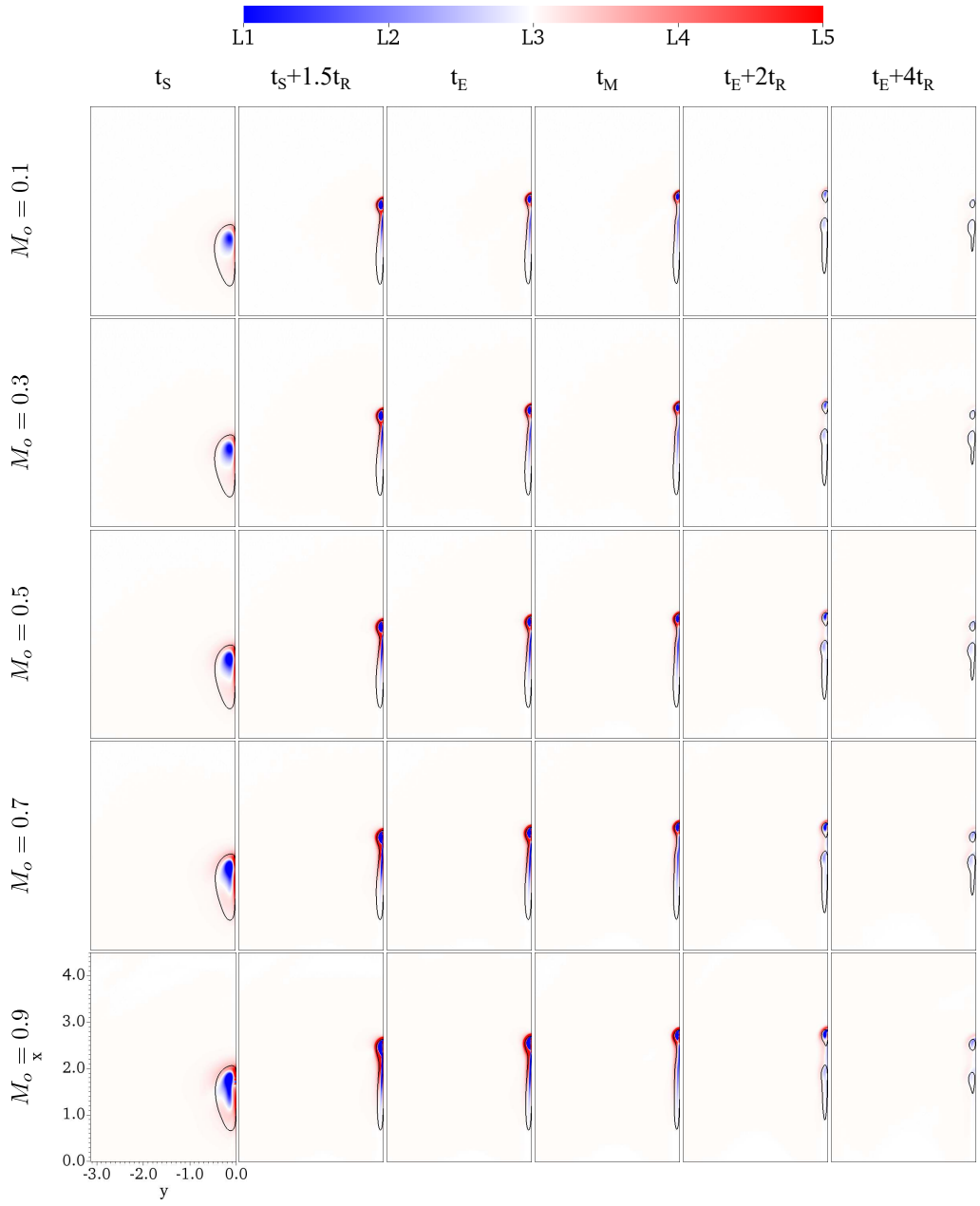

Figure B.3: Source term contour on the symmetric plane. The legend is the same as in Figure 3.12.

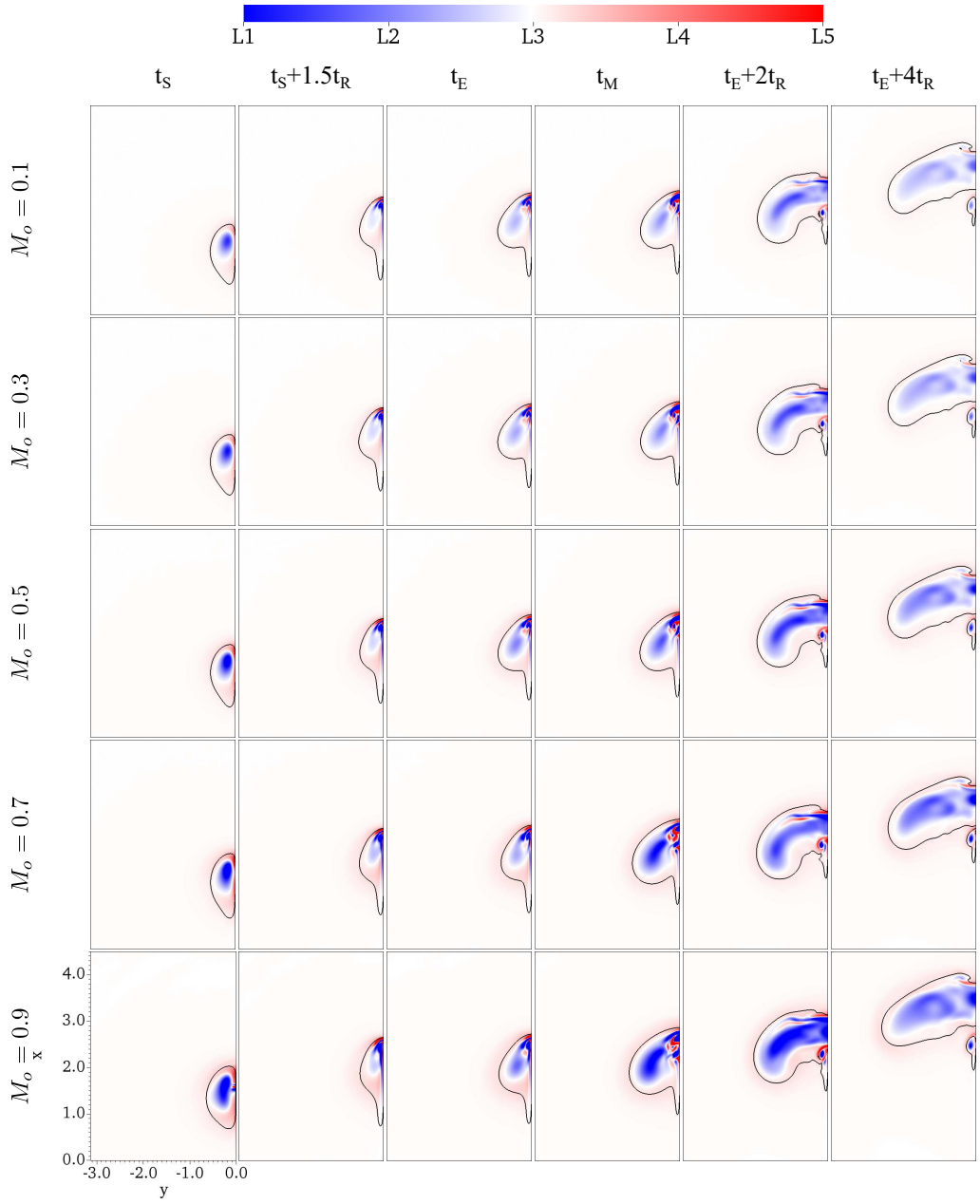

Figure B.4: Source term contour on the bridge plane. The legend is the same as in Figure 3.12.

Appendix C

Reconnection Repetition

Further to the significance in sound generation, vortex reconnection could be deterministic in revealing a physical mechanism of turbulence cascade. In this section, reconnection at high Re and occurrence of the second reconnection between the small-scale structures are briefly investigated. The problem setup is the same as Section 2.2.3; however, a smaller $2\pi^3$ domain with a uniform grid has been used. Also, to be consistent to the previous studies, the simulation time is divided by 2π. Note that to get a different Re, the initial circulation remains constant and the kinematic viscosity is modified; refer to Section 2.2.3 for more explanation.

In the current section, the reference Mach number is constant, $M_o = 0.5$. Simulations are conducted for $Re = 1500, 3000, 6000, 12000$ on four grids, 384^3, 512^3, 640^3, and 1024^3, respectively. Table C.1 shows t_S, t_E, and t_R of these cases. By increasing Re at a constant M_o the start of the reconnection postpones; however, once reconnection begins, circulation transfer takes place more intensely in a way that t_R decreases–note that the post-processing time step for the current results is limited to $dt_p = 0.016$ and it is expected that by using a smaller dt_p the difference between t_R of $Re = 6000$ and $Re = 12000$ becomes clear. The same influence of the Re has been observed on the incompressible reconnection [40]. t_E generally decreases as Re increases; however, due to the generation of small-scale hairpin-like structures which cut the symmetric plane, t_E of $Re = 12000$ does not necessarily follow this general trend.

Circulation evolution for different Re is depicted in Figure C.1(a) which clearly demonstrates three characteristic stages of the reconnection, namely inviscid induction (see the initial almost constant circulation on the symmetric plane), bridging (note the intense decrease in the value of circulation), and threading (period after bridging determined by a

Re	t_S	t_E	t_R
1500	1.321	1.974	0.350
3000	1.369	1.926	0.239
6000	1.401	1.814	0.207
12000	1.432	1.846	0.207

Table C.1: Characteristic times for different Re at $M_o = 0.5$.

moderate inflection). Consistent with the data of Table C.1, the bridging stage is sharper at higher Re. Another interesting point is the negative circulation at the threading stage. Such trend has not been seen in the incompressible regime [40]. It is estimated that such behavior is associated to the extra mechanisms of vorticity generation in the compressible regime which may produce vorticity in the opposite direction. Note that threads keep the same sense of the vorticity direction after reconnection and cannot have contribution to this negative circulation.

Circulation change rate for different Re is plotted in Figure C.1(b). Higher Re leads to a higher $|d\Gamma_z/dt|$ which confirms the intense circulation transfer. The same behavior is captured for the maximum axial and lateral vorticity on the symmetric and collision planes, respectively; see Figures C.1(c) and (d). It can be seen that higher Re brings forward the maximum value of the vorticity on both planes.

In the current study, vortex separation before reconnection is defined as the distance between the point with the maximum axial vorticity on the symmetric plane from the collision plane. After reconnection, vortex separation is defined as the distance between the point with the maximum lateral vorticity on the collision plane from the symmetric plane. Because of the irregular vorticity distribution, Hussain and Melander [40] used vorticity centroid (centroid of the points where vorticity is more than 75% of the maximum vorticity) to define the vortex separation. Figure C.1(e) demonstrates the vortex separation for different Re and has an almost similar evolution as the incompressible regime [40]; therefore, after scaling analysis, virtually similar conclusion is expected for the compressible regime. Scaling analysis of Hussain and Melander [40] for the incompressible regime revealed that the repulsion of the bridges takes less time than the collision of the initial vortex tubes; also, they showed that the repulsion of the bridges is independent of the initial conditions and is dominated by the local curvature and self-induction.

Figure C.1(f) shows that Re has a direct effect on the evolution of M_{max}; Higher Re leads to higher M_{max}. Such behavior could be justified by the higher velocity between the dipole at higher Re. Note that if Re is increased enough, M_{max} may pass the sonic threshold

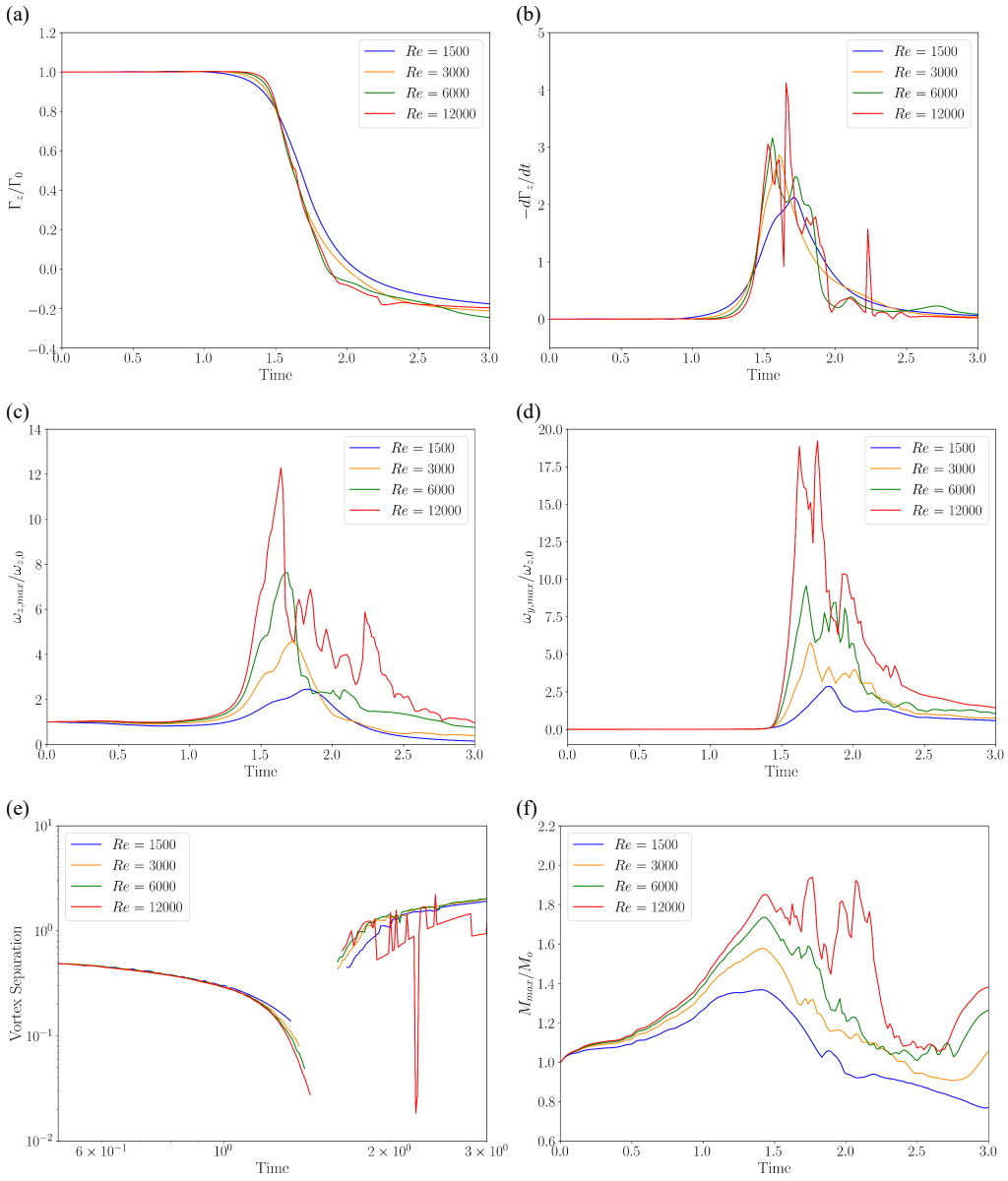

Figure C.1: Effect of Re on the time evolution of the (a) circulation, (b) circulation change rate, (c) maximum axial vorticity on the symmetric plane, (d) maximum lateral vorticity on the collision plane, (e) vortex separation, and (f) M_{max}. The reference Mach number is constant, $M_o = 0.5$.

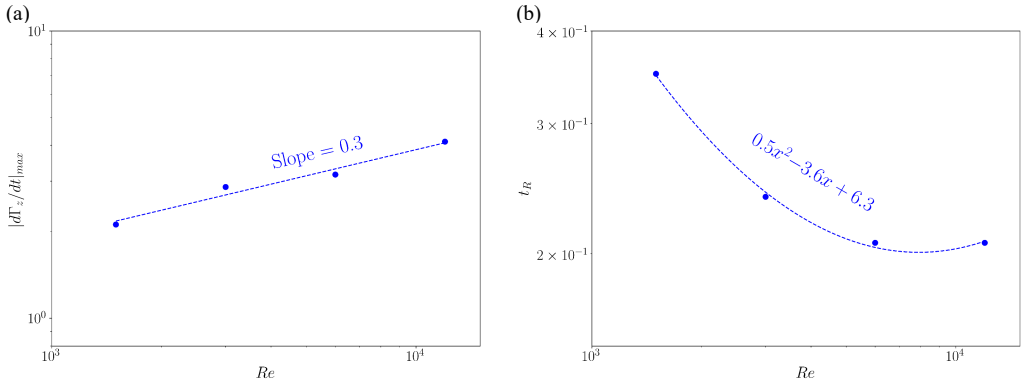

Figure C.2: Scaling of the (a) maximum circulation change rate and (b) t_R (curved line equation is depicted based on x). The reference Mach number is constant, $M_o = 0.5$.

even for $M_o = 0.5$ and can cause shocklet formation. Recall that strong shocks can modify the reconnection process and trigger early circulation transfer. High-Re reconnection near the sonic threshold has not been studied yet.

Figure C.2(a) shows the scaling of the maximum circulation change rate. It is found that the maximum circulation change rate is logarithmically scaled as $|d\Gamma_z/dt|_{max} \approx Re^{0.302}$. For the incompressible regime where a different range of Re ($Re = 250$ to 9000) has been simulated, it was showed that $|d\Gamma_z/dt|_{max} \approx Re^1$ [40].

Considering current cases of the compressible reconnection, reconnection time is scaled as $log(t_R) \approx 0.5(log(Re))^2 - 3.6log(Re) + 6.3$; see Figure C.2(b). In the incompressible regime, for $Re = 250$ to 9000, it was found that $t_R \approx Re^{-0.75}$ [40].

Thus far, because of the instability of the small-scale structures and generation of several dipoles, the second reconnection of small-scale structures has not been captured even at $Re = 10000$ [102, 5]. By imposing symmetric boundary conditions and solving a quarter of the domain, Yao and Hussain [110] captured the second and third reconnections. In the current study, by using the physical periodic boundary conditions and continuing the simulation after the first reconnection, the second reconnection takes place for $Re = 12000$, which is the highest studied Re for this type of the boundary conditions. Note that at $Re = 12000$ the flow evolution is not symmetric anymore. The source of these asymmetries in numerical simulations is considered to be the Kelvin-Helmholtz instability which is triggered by numerical round-off error; compare enstrophy contour evolution on the symmetric plane for $Re = 1500$ and $Re = 12000$ provided in Figure C.3. As seen in C.1(b), during reconnection, there is a sudden change in the circulation change rate for all cases. For $Re = 12000$, there is a second spike at $t_E + 1.86t_R = 2.23$ which

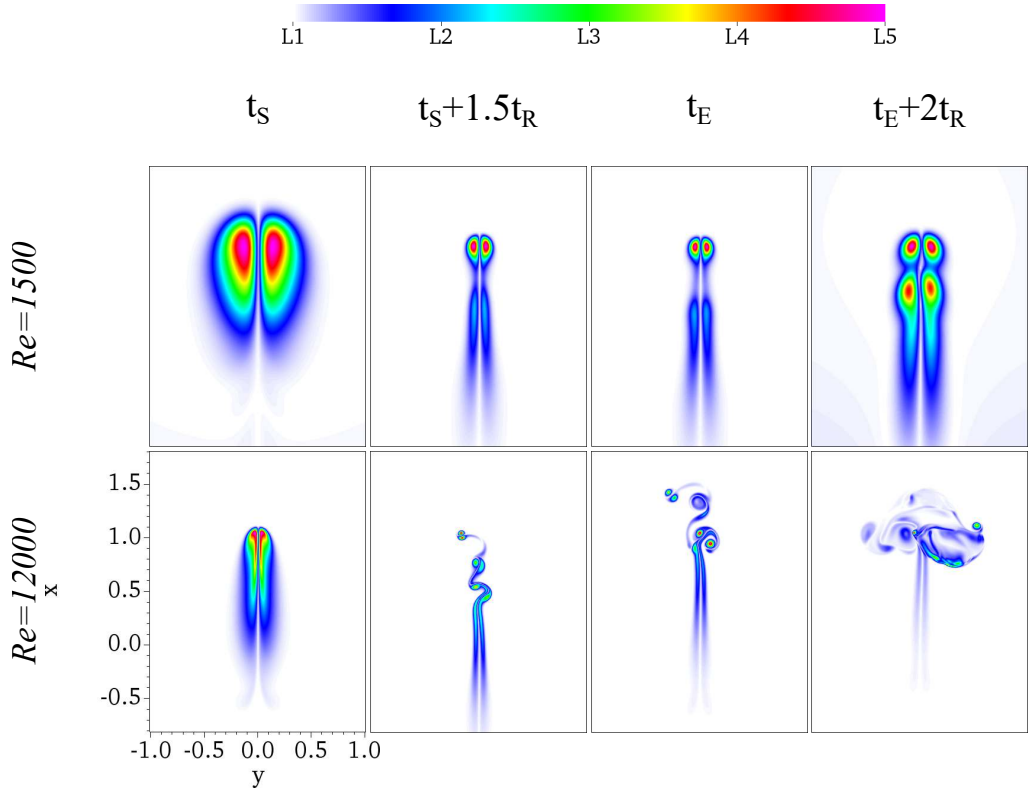

Figure C.3: Enstrophy contour evolution on the symmetric plane. Limits of the global linear legend equal zero and the maximum enstrophy.

implies the second reconnection of small-scale structures–also note the sudden decrease in the vortex separation at the same time in Figure C.1(e). To visualize the reconnected small-scale structures, the simulation is continued for a longer time. Figure C.4 shows the enstrophy isosurface for $Re = 12000$ at $t_E + 6.46t_R = 3.18$. Separations of small ring-like structures near the threads are obvious. Note the appearance of multiple dipoles and hairpin-like looping structures around the threads. This phenomenon, which proves the role of the reconnection in fine-scale mixing [40], also reasserts the physical model of turbulence cascade through vortex reconnection scenario [110].

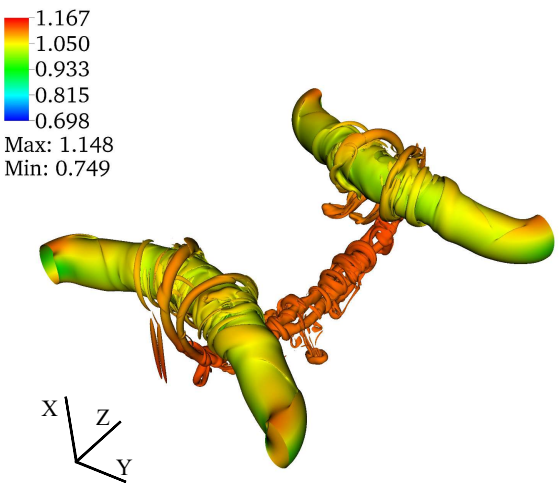

Figure C.4: Enstrophy isosurface at 15% of the maximum initial axial vorticity for $Re = 12000$ at $t_E + 6.46t_R = 3.18$. The color represents divided pressure, P/P_p.